

Accurate distances to Galactic globular clusters through a combination of *Gaia* EDR3, *HST* and literature data

H. Baumgardt^{1*}, E. Vasiliev^{2,3}

¹ *School of Mathematics and Physics, The University of Queensland, St. Lucia, QLD 4072, Australia*

² *Institute of Astronomy, University of Cambridge, Madingley Road, Cambridge CB3 0HA, UK*

³ *Lebedev Physical Institute, Leninsky prospekt 53, 119991 Moscow, Russia*

Accepted 2021 xx xx. Received 2021 xx xx; in original form 2021 xx xx

ABSTRACT

We have derived accurate distances to Galactic globular clusters by combining data from the *Gaia* Early Data Release 3 (EDR3) with distances based on Hubble Space telescope (*HST*) data and literature based distances. We determine distances either directly from the *Gaia* EDR3 parallaxes, or kinematically by combining line-of-sight velocity dispersion profiles with *Gaia* EDR3 and *HST* based proper motion velocity dispersion profiles. We furthermore calculate cluster distances from fitting nearby subdwarfs, whose absolute luminosities we determine from their *Gaia* EDR3 parallaxes, to globular cluster main-sequences. We finally use *HST* based stellar number counts to determine distances. We find good agreement in the average distances derived from the different methods down to a level of about 2%. Combining all available data, we are able to derive distances to 162 Galactic globular clusters, with the distances to about 20 nearby globular clusters determined with an accuracy of 1% or better. We finally discuss the implications of our distances for the value of the local Hubble constant.

Key words: globular clusters: general – stars: distances

1 INTRODUCTION

Galactic globular clusters constitute an important rung on the extragalactic distance ladder. They are nearby enough to be resolved into individual stars, making them ideal objects to calibrate the brightnesses of physically interesting stars like RR Lyrae or Type II Cepheids. In addition they are also massive enough to contain statistically significant samples of these stars. Hence globular clusters are useful to determine the slopes and zero-points of RR Lyrae period-luminosity (P/L) relations (e.g. Bono, Caputo & Di Criscienzo 2007; Dambis et al. 2014) as well as a possible metallicity dependence of the zero points (e.g. Sollima, Cacciari & Valentini 2006). Globular clusters can also be used as calibrators for other distance methods, like the tip of the red giant branch distance method (TRGB), which allows to determine distances to external galaxies without having to rely on P/L relations of variable stars (e.g. Cerny et al. 2020; Freedman et al. 2020; Soltis, Casertano & Riess 2021).

Distances to globular clusters are determined either through fits of their color-magnitude diagrams (CMDs) with theoretical isochrones (e.g. Ferraro et al. 1999; Dotter et al. 2010; Gontcharov, Mosenkov & Khovritchev 2019; Valcin

et al. 2020), or by using variable stars that follow known relations between their periods and absolute luminosities like RR Lyrae stars (e.g. Bono, Caputo & Di Criscienzo 2007; Hernitschek et al. 2019), Type II Cepheids (Matsunaga et al. 2006) or Mira type variables (Feast, Whitelock & Menzies 2002). In order to avoid circularity, the absolute luminosities of these stars need to be determined independently from globular cluster distances by using for example theoretical models (e.g. Catelan, Pritzl & Smith 2004) or *Hipparcos* or *Gaia* parallaxes (Fernley et al. 1998; Neeley et al. 2019; Ripepi et al. 2019). Accurate distances have also been obtained for globular clusters by using eclipsing binaries (Kaluzny et al. 2007; Thompson et al. 2020), however the faintness and scarcity of suitable binaries means that observations have so far been limited to a few globular clusters. Finally it is possible to determine distances by comparing the magnitudes of main-sequence stars with stars of similar metallicity in the solar neighborhood, the so-called subdwarf method (e.g. Reid & Gizis 1998; Cohen & Sarajedini 2012) or kinematically by comparing line-of-sight and proper motion velocity dispersion profiles in globular clusters (e.g. McNamara, Harrison & Baumgardt 2004; van de Ven et al. 2006; Watkins et al. 2015b). The latter method has the advantage that the derived distance is not influenced by the reddening of the cluster.

* E-mail: h.baumgardt@uq.edu.au

Typical uncertainties in the zero points of the P/L relations of RR Lyrae stars are thought to be of order 0.05 mag (Bhardwaj 2020) and other methods like CMD fitting have similar uncertainties. In addition, the reddening of many clusters presents an additional challenge for the determination of accurate distances since it can be variable even across small, arcminute size fields (Bonatto, Campos & Kepler 2013; Palla et al. 2019). Furthermore there is evidence for non-standard reddening laws in the directions of several globular clusters like for example M4 (Dixon & Longmore 1993; Hendricks et al. 2012).

It is therefore important to use independent methods to verify the distances to globular clusters, especially methods which are not affected by the reddening of stars. In this paper we use data from the *Gaia* EDR3 catalogue (Gaia Collaboration et al. 2016, 2020) to determine distances to Galactic globular clusters. In addition to using the *Gaia* EDR3 parallaxes directly, we also determine moving group distances and kinematic distances derived by comparing proper motion velocity dispersion profiles with line-of-sight velocity dispersion ones. We finally use the *Gaia* EDR3 parallaxes of nearby subdwarfs as well as Hubble Space Telescope (HST) star counts together with kinematic information to determine distances.

Our paper is organised as follows: In sec. 2 we present our derivation of cluster distances using the methods mentioned above. In sec. 3 we describe our survey of literature distances. We compare the distances that we derive from the different methods and derive the average distance to each globular cluster in sec. 4. We finally draw our conclusions in sec. 5.

2 ANALYSIS

2.1 Cluster sample and selection of member stars

We take our target list of globular clusters from Baumgardt et al. (2019b). To this sample we add six additional Milky Way globular clusters that have been found in recent years: VVV-CL001 (Minniti et al. 2011; Fernández-Trincado et al. 2021), BH 140 and FSR 1758 (Cantat-Gaudin et al. 2018), Sagittarius II (Laevens et al. 2015; Mutlu-Pakdil et al. 2018), RLGC 1 and RLGC 2 (Ryu & Lee 2018), and Laevens 3 (Longeard et al. 2019). The status of Sagittarius II is still debated, while Mutlu-Pakdil et al. (2018) argue for it to be a star cluster based on its location in a size vs. luminosity plane, Longeard et al. (2020) argue, based on a small spread in [Fe/H] that they find among the cluster stars, for it to be a dwarf galaxy. We tentatively include the object in our list of clusters. The other systems are most likely globular clusters based on their color-magnitude diagrams, kinematics and location in the Milky Way. Together with the 158 GCs studied in Baumgardt et al. (2019b), we therefore have a sample of 162 globular clusters.

2.2 Cluster parallax distances

Determining distances to globular clusters via the parallaxes of individual stars has the advantage that the distances are determined directly, without having to rely on another distance method as an intermediate step in the distance ladder.

In addition, parallaxes are not influenced by the reddening of the clusters. In this paper, we take the cluster parallaxes from Vasiliev & Baumgardt (2021) (hereafter VB21). VB21 determined mean parallaxes for 170 globular and outer halo star clusters by averaging the cluster parallaxes of individual member stars from the *Gaia* EDR3 catalogue. Cluster members were selected based on the *Gaia* EDR3 proper motions and parallaxes. VB21 also applied multi-gaussian mixture modeling to classify stars into cluster members and background stars and determined the mean cluster parameters and their errors over multiple realizations of statistically created member catalogues. In order to account for possible magnitude, color and position dependent biases in the *Gaia* catalogue, VB21 applied the parallax corrections of Lindegren et al. (2020) to the individual stellar parallaxes. However when testing the derived cluster parallaxes against the literature distances that we derive further below, VB21 found that even after applying the Lindegren et al. corrections, there is still a mean offset in the *Gaia* parallaxes. In particular, they found that the parallax corrections suggested by Lindegren et al. (2020) might have been over-correcting the *Gaia* EDR3 parallaxes by $\Delta\varpi \sim 0.007$ mas. VB21 also found evidence for spatially correlated small scale systematic errors of order $\epsilon_\varpi \sim 0.01$ mas. We therefore subtract $\Delta\varpi = 0.007$ mas from the derived mean parallaxes to correct for the parallax bias. The small-scale correlated errors were already taken into account by the parallax averaging procedure of VB21. We list the median distances $D = 1/\varpi$ for clusters with $\varpi/\sigma_\varpi > 10$ in Table 2 to allow a comparison of the *Gaia* EDR3 parallax distances with the other distances that we derive. When calculating mean cluster distances we use the data for all clusters and the parallax values directly as will be described further below.

2.3 Kinematic distances

For clusters with accurately measured line-of-sight and proper motion velocity dispersion profiles one can determine cluster distances kinematically by varying the cluster distance until the velocity dispersions are the same or a best match to a theoretical model of the cluster is achieved (e.g. Hénault-Brunet et al. 2019). The advantage of such kinematic distances is that, like parallaxes, the kinematic distance method is a direct method which does not rely on other, more nearby methods in the distance ladder. Similar to parallax distances, kinematic distances are also not affected by cluster reddening, allowing in principle to derive accurate distances for highly reddened clusters. In order to calculate kinematic distances, one either needs to know the anisotropy profile of the internal velocity dispersion of a cluster, or assume that the cluster is isotropic. The latter is most often assumed since observed velocity dispersion profiles usually show that globular clusters are isotropic, at least in their inner parts (van Leeuwen et al. 2000; Watkins et al. 2015a; Raso et al. 2020; Cohen et al. 2021), N -body simulations of star clusters also show that most globular clusters should have isotropic velocity dispersion profiles (Baumgardt & Makino 2003; Lützgendorf et al. 2011; Tiongco, Vesperini & Varri 2016).

We take the line-of-sight velocity dispersion profiles for the kinematic distance fitting from Baumgardt & Hilker (2018), Baumgardt et al. (2019a) and Baumgardt et al.

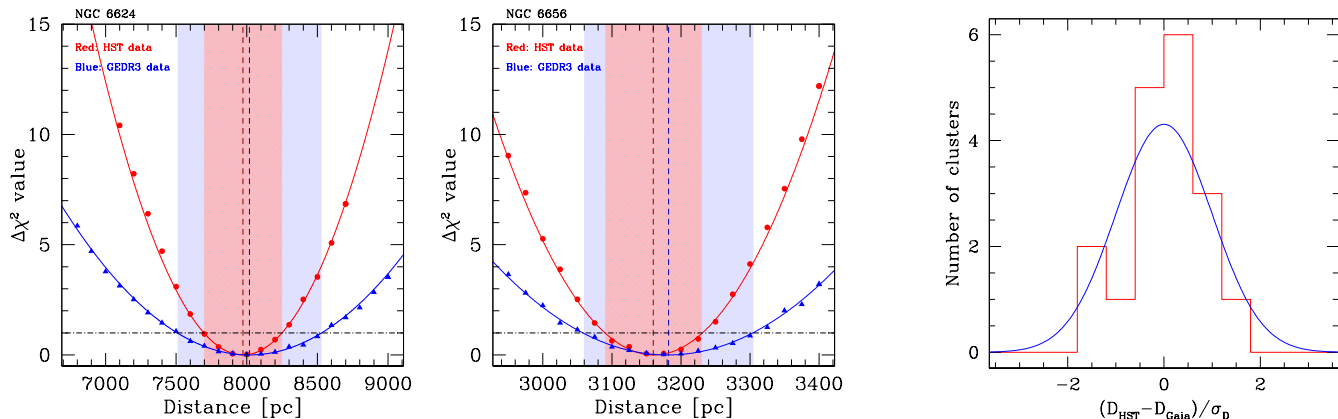


Figure 1. Illustration of the kinematic distance determination for the globular clusters NGC 6624 (left panel) and NGC 6656 (middle panel). Shown are the χ^2 values from the fit of our N -body models to the velocity dispersion profiles as a function of distance for the *HST* proper motions (red circles) and *Gaia* EDR3 proper motions (blue triangles). Solid lines show a quadratic fit to the χ^2 values of each data set and the dashed lines and shaded areas mark the best-fitting distances and their 1σ error. The literature distances are $D = 8020$ pc (NGC 6624) and $D = 3330$ pc (NGC 6656) and are in agreement with the kinematic ones. The right panel compares the error-weighted distance differences from *Gaia* and *HST* data for clusters which have proper motion velocity dispersion profiles from both satellites. The resulting distribution is compatible with a normal distribution (shown by a blue solid line).

(2019b). Baumgardt & Hilker (2018) calculated line-of-sight velocity dispersion profiles by combining literature velocities with line-of-sight velocities derived from archival spectra from the ESO and Keck data archives. Baumgardt et al. (2019a) and Baumgardt et al. (2019b) added line-of-sight velocities from *Gaia* DR2 and the Anglo-Australian Observatory (AAO) data archive to these profiles. In addition we use the line-of-sight velocity dispersion profiles published by Kamann et al. (2018) based on MUSE data. We take the proper motion dispersion profiles either from VB21 based on *Gaia* EDR3 data, or from published profiles based on multi-epoch *HST* measurements. Table 1 lists the *HST* proper motion velocity dispersion profiles that we use in this paper together with the distances that we derive from these profiles. Unfortunately we could not use the recently published proper motion dispersion profiles for nine inner Milky Way globular clusters by Cohen et al. (2021) since no accurate line-of-sight velocity dispersion profiles are available for these clusters.

We determine a kinematic distance independently for each proper motion velocity dispersion profile that we have from either *Gaia* EDR3 or *HST* data. The best-fitting distance is determined by fitting each cluster with the grid of N -body models calculated by Baumgardt (2017) and Baumgardt & Hilker (2018). Their grid contains several thousand N -body models of star clusters, varying the size, initial density profile, metallicity and stellar mass function of each cluster. We interpolate within this grid and determine for each cluster the N -body model that simultaneously provides the best fit to the internal mass function, velocity dispersion and surface density profile. More details about the N -body models can be found in Baumgardt (2017) and Baumgardt & Hilker (2018) and we refer the reader to these papers for a full description of the fitting procedure.

We restrict the radial extent of the line-of-sight velocity dispersion profiles to the same range for which we have proper motion dispersions in order to avoid a possible bias due to the N -body models not providing a match to the

Table 1. Kinematic distances based on *HST* proper motion velocity dispersion profiles. The second last panel gives the kinematic distance derived by the authors of the original *HST* data set, the last column gives our distances for the same data set.

Cluster	HST Data set	Lit. Dist. [kpc]	Our Dist. [kpc]
NGC 104	Watkins et al. (2015a)	4.45 ± 0.50	4.545 ± 0.047
	Heyl et al. (2017)	4.29 ± 0.47	4.347 ± 0.236
NGC 288	Watkins et al. (2015a)	9.98 ± 0.37	9.098 ± 0.291
NGC 362	Watkins et al. (2015a)	9.37 ± 0.18	9.202 ± 0.280
NGC 1261	Raso et al. (2020)	—	16.775 ± 0.824
NGC 1851	Watkins et al. (2015a)	11.41 ± 0.20	11.440 ± 0.254
NGC 2808	Watkins et al. (2015a)	10.18 ± 0.12	9.837 ± 0.122
NGC 5139	Watkins et al. (2015a)	5.22 ± 0.05	5.264 ± 0.082
NGC 5904	Watkins et al. (2015a)	8.77 ± 0.15	7.456 ± 0.146
NGC 6266	Watkins et al. (2015a)	5.67 ± 0.07	6.354 ± 0.128
	McNamara et al. (2012)	—	6.945 ± 0.264
NGC 6341	Watkins et al. (2015a)	8.43 ± 0.34	8.231 ± 0.347
NGC 6352	Libralato et al. (2019)	—	6.260 ± 0.762
NGC 6362	Watkins et al. (2015a)	7.34 ± 0.24	7.720 ± 0.315
NGC 6388	Watkins et al. (2015a)	10.44 ± 0.12	10.894 ± 0.137
NGC 6397	Watkins et al. (2015a)	2.54 ± 0.05	2.332 ± 0.057
	Heyl et al. (2012)	2.20 ± 0.60	2.416 ± 0.062
NGC 6441	Watkins et al. (2015a)	11.77 ± 0.20	12.059 ± 0.172
	Häberle et al. (2021)	12.74 ± 0.16	12.364 ± 0.226
NGC 6624	Watkins et al. (2015a)	6.69 ± 0.36	7.972 ± 0.277
NGC 6656	Watkins et al. (2015a)	3.18 ± 0.07	3.161 ± 0.070
NGC 6681	Watkins et al. (2015a)	9.33 ± 0.14	9.260 ± 0.165
NGC 6715	Watkins et al. (2015a)	23.79 ± 0.33	25.019 ± 0.646
NGC 6752	Watkins et al. (2015a)	4.28 ± 0.03	4.005 ± 0.130
NGC 7078	Watkins et al. (2015a)	10.23 ± 0.13	10.375 ± 0.237

full profile. In the N -body models we measure the line-of-sight velocity dispersion profile for stars brighter than the main-sequence turnoff. The magnitude limit for the proper motion velocity dispersion profiles was varied for each data set independently so we match the magnitude limit of the

observed data. Hence, except for the nearest clusters like NGC 6121, we chose a magnitude limit equal to the main-sequence turnoff for fits to the *Gaia* EDR3 proper motions, while we choose deeper limits for the *HST* data. The left and middle panels of Fig. 1 show the resulting fits to two clusters that have both *Gaia* and *HST* data and Table 1 gives the derived distances from the *HST* data together with the kinematic distances derived by the authors of the original papers. There is usually good agreement between the distances derived by us and the original kinematic distances. The only exceptions are NGC 5904 and NGC 6266. At least for NGC 5904, one the reason for different distances could be the lack of a radial overlap between the line-of-sight and proper motion velocity dispersion profiles used by Watkins et al. (2015a), which makes the derived distance strongly dependent on the dynamical model used for the cluster.

We give the full set of distances including the *Gaia* ED3 kinematic distances in the Appendix. The right panel of Fig. 1 shows the error weighted distribution of differences in the kinematic distances for the *Gaia* EDR3 and *HST* data. It can be seen that they roughly follow a normal distribution, indicating good agreement between the *HST* and *Gaia* distances.

2.4 Subdwarf distances

The main idea of our subdwarf distances is to make use of the excellent accuracy of *Gaia* EDR3 parallaxes for nearby stars. As discussed in sec. 2.2, *Gaia* EDR3 parallaxes have small-scale, systematic uncertainties of ~ 0.01 mas that can't be removed through calibration of the parallaxes against objects with known parallaxes. This means that even the distances to the nearest globular clusters cannot be determined directly with an accuracy better than a few percent. The accuracy of parallax distances also quickly deteriorates with increasing distance and drops below the accuracy of CMD fitting distances beyond distances of about 5 kpc. In contrast, the distance to a nearby star at $d = 100$ pc has a relative uncertainty of only 0.1% using *Gaia* EDR3 parallaxes.

Our basic approach for deriving subdwarf distances is the same as the one used by Cohen & Sarajedini (2012), except that we replace the Hipparcos parallaxes by *Gaia* EDR3 ones. We start using the compilation of precise Johnson-Cousins UBVRI photometry of nearby subdwarfs by Casagrande et al. (2010) and identify the counter-parts of these stars in the *Gaia* EDR3 catalogue. We then apply the Lindegren et al. (2020) parallax corrections to the stars as well as the additional shift of $\Delta\varpi = 0.007$ mas found by VB21. Using only stars which have published *V* and *I* band photometry by Casagrande et al. (2010), a reddening $E(B - V) < 0.02$ and *Gaia* EDR3 parallaxes with a relative precision $\varpi/\epsilon_\varpi > 20$ leaves us with a sample of 206 stars. Despite our more stringent limit on the parallax accuracy, our sample is almost a factor 10 larger than the one used by Cohen & Sarajedini (2012). Thanks to the superior accuracy of the *Gaia* EDR3 parallaxes, our sample also contains about 20 stars with metallicities $[\text{Fe}/\text{H}] < -2.0$, while no accurate Hipparcos parallaxes were available for any of these stars. We finally use the SIMBAD astronomical data base to exclude known binaries from this sample, leaving us with a sample of 185 stars.

Our source for the globular cluster photometry is the compilation of *HST* photometry published by Sarajedini et al. (2007) based on observations made with the Advanced Camera for Surveys (ACS) onboard *HST*. Their survey contains deep photometry in the ACS/WFC F606W and F814W bands for 67 globular clusters. In addition to the photometry for 67 globular clusters from Sarajedini et al. (2007), we also use the ACS/WFC photometry published by Dotter, Sarajedini & Anderson (2011) for 6 globular clusters as well as the photometry for NGC 6528 from Lagioia et al. (2014) that was kindly provided to us by the authors. We finally use the photometry from Baumgardt et al. (2019b) for an additional 6 globular clusters (NGC 6325, NGC 6342, NGC 6355, NGC 6380, NGC 6401 and NGC 6558). We skipped Pal 2 due to significant differential reddening and E 3 since the cluster has such a low mass that the location of its main sequence cannot be accurately determined. This leaves us with a sample of 79 globular clusters with accurate, deep ACS/WFC photometry in the F606W and F814W bands.

We dereddened the photometry of each globular cluster using the reddening values given by Dotter et al. (2010) together with the extinction coefficients from Sirianni et al. (2005). We then transformed the subdwarf photometry, from the Johnson-Cousins UBVRI system to the ACS/WFC filter system using eqn. 12 of Sirianni et al. (2005) together with the transformation coefficients given in Table 18 of their paper. We then fitted PARSEC isochrones (Bressan et al. 2012) to the color-magnitude diagram of each cluster, and used the isochrone to select the cluster members. We then calculated the average color of the cluster stars as a function of magnitude and define a main-sequence ridge line by cubic spline interpolation between the data points.

In order to compare the subdwarf photometry with the globular cluster photometry and derive the cluster distances, we select for each globular cluster all subdwarfs with metallicities $|[\text{Fe}/\text{H}]_{SD} - [\text{Fe}/\text{H}]_{GC}| < 0.2$. We took the metallicities of the subdwarfs from Casagrande et al. (2010) and the metallicities of the globular clusters from Carretta et al. (2009). In order to correct the colors of the subdwarfs to the color they would have at the metallicity of the globular cluster, we created a set of PARSEC isochrones equally spaced in metallicity by $\Delta[\text{Fe}/\text{H}] = 0.5$ and calculate the colors of zero-age main sequence stars as a function of their absolute *V*-band luminosity. We then use this grid of isochrones and the absolute magnitudes of the subdwarfs which we calculate using their *Gaia* EDR3 parallaxes to correct the subdwarf colors for the difference in metallicity. Due to the proximity of the subdwarf metallicities to the metallicity of the clusters, the resulting shifts are always below 0.02 mag.

After transforming the subdwarf photometry to the ACS/WFC system and correcting the subdwarf metallicities, we fitted the cluster main sequences in a $(F814W_0 \text{ vs. } (F606W - F814W)_0)$ CMD with the subdwarfs. To this end, we vary the assumed cluster distance modulus until the error-weighted difference between the subdwarfs and the previously determined main-sequence ridgeline are minimal. Due to the steepness of the cluster ridgelines and the accurate *Gaia* parallax distances, this essentially results in minimizing the error weighted color differences between the subdwarfs and the main sequence ridge lines. We exclude subdwarfs with $M_{814} < 4$ from the fits since these could already

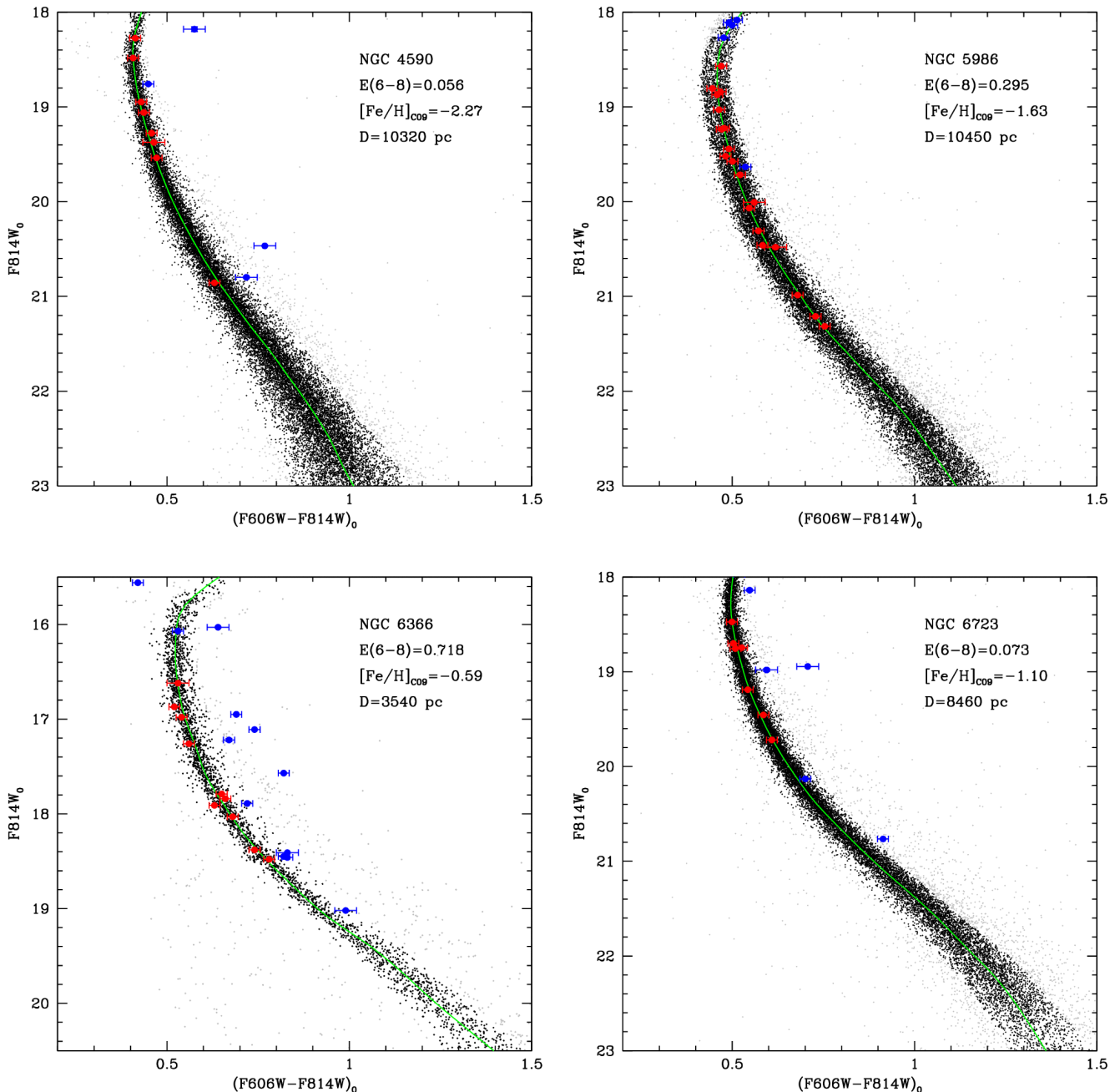


Figure 2. Illustration of the subdwarf distance determination for four globular clusters with a range of metallicity and reddening values. Grey points mark stars considered to be background stars, black points are cluster members. The green line shows our fitted ridge line for each cluster. Subdwarfs used in the distance fitting are shown by red circles, subdwarfs not used are shown by blue circles. Photometric error bars are also shown. Note that the error in absolute magnitude due to the *Gaia* EDR3 parallax error is shown but usually too small to be seen.

have evolved away from the main sequence. We also exclude subdwarfs with discrepant photometry since these could be undetected binaries. Fig. 2 shows examples of our subdwarf fits for four globular clusters. The clusters shown are the same as the ones depicted in Fig. 2 of Cohen & Sarajedini (2012). We will derive an error bar for the subdwarf distance moduli in sec. 3 when we compare the subdwarf distance moduli against literature data.

2.5 Star count distances

For a given velocity dispersion profile, the derived mass of a cluster increases (decreases) with increasing (decreasing) cluster distance. If the velocity dispersion profile is based entirely on line-of-sight velocities, the total cluster mass changes linearly with distance, while for a cluster with a velocity dispersion profile based only on proper motions, the mass changes with the distance to the third power. For a cluster with measured line-of-sight and proper motion ve-

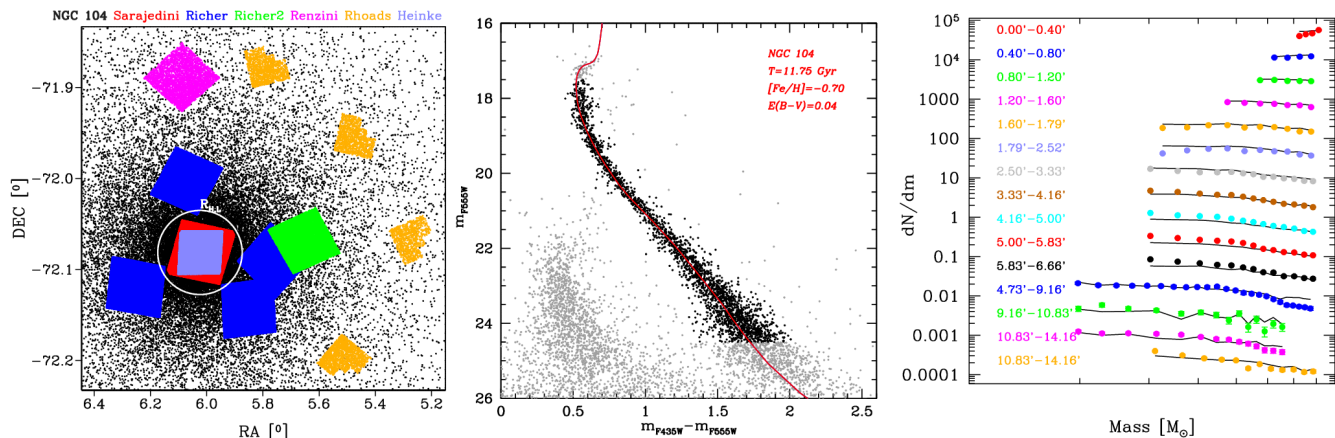


Figure 3. Illustration of the fit of our N -body models to the globular cluster NGC 104. The left panel shows all fields in NGC 104 with available *HST* photometry. The different fields are labeled by the name of the Principal Investigator of the *HST* observations and the white circle marks the observed half-light radius of NGC 104. The middle panel shows the fit of a PARSEC isochrone (shown in red) to the combined photometry of the four *HST*/WFPC2 fields of Rhoads (*HST* Proposal ID: 9634) from the left panel. The parameters of the isochrone are given in the figure. Grey circles mark all stars in the field and black stars are the stars used for the determination of the stellar mass function of NGC 104. The group of stars visible in the lower left part of the middle panel is the SMC. The right panel compares the derived mass functions as a function of radius against the mass function of the best-fitting N -body model (shown by solid lines). There is a clear change in the derived mass function slope from increasing towards higher masses in the centre to increasing towards lower masses in the outermost parts, indicating that NGC 104 is mass segregated. This trend is reproduced by the best-fitting N -body model.

locities, the scaling will be in between these limits. Since the predicted number of main-sequence stars changes linearly with the cluster mass (for a given mass function), one can use the observed number of cluster stars in a given magnitude interval and a given field, together with the measured cluster kinematics and a theoretical model for the cluster, to determine the cluster distance.

We use as source for the globular cluster photometry the compilation of ACS/WFC F606W/F814W photometry published by Sarajedini et al. (2007) as well the *HST* photometry that was derived in Baumgardt et al. (2019b), Baumgardt, Sollima & Hilker (2020) and Ebrahimi et al. (2020). We also use the photometry published by Kerber et al. (2018) for NGC 6626 as input photometry. We exclude NGC 5139 from this list due to the significant metallicity spread among the cluster stars. For each *HST* observation, we again fit PARSEC isochrones (Bressan et al. 2012) to the cluster color-magnitude diagrams. To create the isochrones, we use the cluster ages derived by VandenBerg et al. (2013), or, for clusters not studied by them, from available literature sources, and take the cluster metallicities and reddenings from Harris (1996). From the isochrones we then derive individual stellar masses for the main-sequence stars in the clusters. We fit the N -body models of Baumgardt (2017) and Baumgardt & Hilker (2018) to the observed surface density, velocity dispersion profiles and the observed mass function of main sequence stars in the *HST* fields and determine the best-fitting N -body model from the fit. For each *HST* observation, we fit a power-law mass function $N(m) \sim m^\alpha$ to the observed stellar mass distribution as well as the masses of stars in the N -body models in the same field. We use the mass function slopes α as fit parameters but not the absolute number of stars. Fig. 3 shows as an example the distribution of *HST* fields with measured photometry (left panel), the derived color-magnitude diagram (middle panel), and the

measured stellar mass functions at different distances from the centre (right panel) for the globular cluster NGC 104.

Varying the cluster distance, we then determine the distance that gives the best match between the number of main-sequence stars in the best-fitting N -body model and the observed number of main sequence stars in the different *HST* fields. We restrict ourselves to well observed clusters in which the errors of the total mass (based on the cluster kinematics) are less than 5%.

Fig. 4 depicts the ratio between the best-fitting cluster distances based on the star count method against the mean cluster distances that we derive from the other methods. We split the cluster sample into two groups, clusters with 10 or more distance determinations from the other methods and clusters with less than 10 measurements. We expect that the distances of clusters in the first group are well determined so that any deviation is mainly due to errors in the star count distances. It can be seen that the average distance ratio is well below unity. The reason is probably that the N -body models that we use to fit the clusters do not contain primordial binaries. Since the average mass of binaries is larger than that of single stars, real globular clusters contain fewer stellar systems than models with only single stars for the same total mass, leading to an underprediction of the cluster distances with our method. The size of this underprediction is also in rough agreement with the observed binary fractions, which are around 10% (Sollima et al. 2007; Milone et al. 2012; Giesers et al. 2019). Fig. 4 also indicates that the star count distances contain additional errors that are not accounted for by the uncertainties in the cluster kinematics, since even when applying a constant shift, the deviations between the star count distances and the mean distances of the other methods are larger than what can be accounted for by the errors in either method. These additional errors could arise due to for example mismatches between the cho-

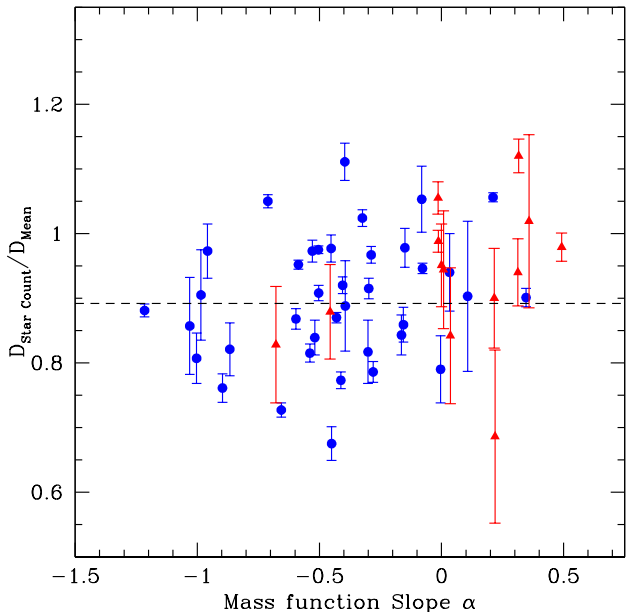


Figure 4. Ratio of the best-fitting distance based on star counts to the average distance from the other methods as a function of the global mass function slope α of the clusters. The cluster sample is split into clusters with 10 or more distance measurements (blue circles) and those with less than 10 individual measurements (red triangles). The dashed line shows the average $D_{StarCount}/D_{Mean}$ ratio for the former group which has more secure distance determinations. It can be seen that the average ratio is well below unity.

sen mass functions of the N -body models and those of the real clusters or errors in the conversion from luminosity to mass from the isochrones. We will fit for an additional shift in the star count distances as well as additional errors in sec. 4 when we compare all distances.

2.6 Moving group distances

Stars in star clusters move on very similar trajectories through the Milky Way since the internal motion of stars in the cluster is usually two orders of magnitudes smaller than the velocity with which the cluster moves around the Galactic centre. As the distance and viewing angle to the stars changes along the orbit, the proper motion and line-of-sight velocity of the stars will change as well and one can use this variation to measure the distance to the cluster. This is the so-called moving group or convergent point method (Brown 1950; de Bruijne 1999). To first order, the change in proper motion μ due to these perspective effects can be approximated by

$$\mu = -\frac{v_{Los}\alpha}{DA} \text{ mas yr}^{-1} \quad (1)$$

where v_{Los} is the line-of-sight velocity of the cluster in km/sec, α the distance from the cluster centre in the direction of motion in radians, D the distance of the cluster from the Sun in kpc, and $A = 4.74$ (Brown 1950; van de Ven et al. 2006). Using the above equation, VB21 determined moving group distances to about 40 globular clusters based on *Gaia* EDR3 proper motions and the average line-of-sight velocities of the clusters from Baumgardt & Hilker

(2018). Here we use the two most precisely determined distances $D = 4.62 \pm 0.28$ kpc (NGC 3201) and $D = 5.34 \pm 0.55$ kpc (NGC 5139). For all other clusters the derived distances have too large error bars to be useful.

3 LITERATURE SURVEY OF GLOBULAR CLUSTER DISTANCES

In addition to our own distance determinations, we also performed a literature search of globular cluster distances. Limiting our search to the last 20 to 25 years, we were able to find about 1300 distance determinations in total, with each globular cluster having between 1 to 35 individual measurements. Whenever a paper gave multiple measurements for the same cluster, we averaged these and took the scatter between the individual values as an indication of the uncertainty. When we had multiple distance determinations from the same research group which were based on the same method and similar input data, we included only the newest value since we expect the different distances to not be independent from each other and the newest measurement to be the most accurate one. When a paper gave both a distance and a distance modulus to a cluster, we used the distance modulus since we expect the errors to be Gaussian only in distance modulus. The resulting list of distance moduli and distances can be found in the Appendix.

In order to calculate a mean distance modulus for each cluster, we de-reddened distance moduli using the reddening values given in the papers, or, if no value was available, given in the 2010 edition of Harris (1996). We also transformed linear distances into distance moduli for those papers which did not give distance moduli. For distance moduli without an error bar, we assumed an error equal to the mean error of the other distance determinations for the same cluster, with a minimum of 0.10 mag. A comparison of distance moduli for a few well observed clusters shows that even in clusters with low reddening, individual distance moduli show a scatter of around 0.07 to 0.10 mag around the mean. This scatter is independent of the chosen method, with only eclipsing binary and RR Lyrae distances based on infrared P/L relations showing smaller scatter. We therefore set the minimum error of any measurement except for EB or infrared RR Lyrae distances, for which we use the quoted errors, to 0.07 mag. We neglected distances that deviate strongly from the other measurements. In total we had to exclude about 25 measurements out of the 1300 measurements we found this way. Most of the excluded measurements were for highly reddened clusters with $E(B - V) > 1.0$ where the individual measurements also often show a larger scatter. This scatter probably reflects an uncertainty in the exact amount of reddening and the proper selection of cluster and background stars.

We also found that the subdwarf distance moduli of Cohen & Sarajedini (2012) were systematically smaller than the other literature values for low-metallicity clusters with $[Fe/H] < -1.2$. The average difference increased with decreasing metallicity and reached about 0.30 mag for the lowest-metallicity clusters. In order to correct this bias, we fitted a linear relation between the difference in distance modulus and metallicity to the data and shifted the Cohen & Sarajedini (2012) distance moduli upwards to bring them

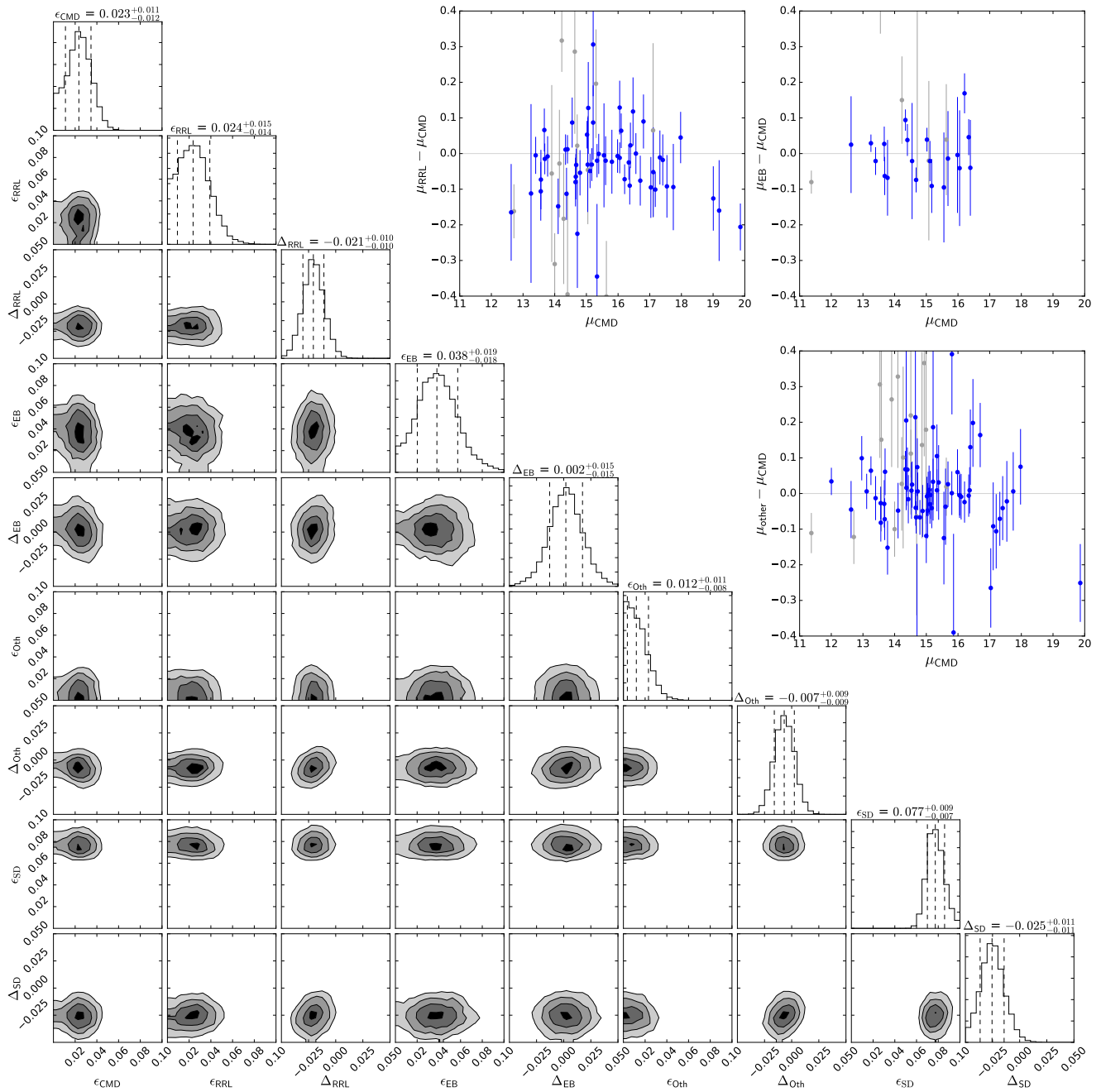


Figure 5. Comparison of the distance moduli derived from isochrone fitting of CMDs (CMD), optical RR Lyrae P/L relations (RRL), eclipsing binaries and infrared RR Lyrae P/L relations (EB), and a combination of all other literature methods (OTH) and our subdwarf distance moduli (SD). For each of the methods shown we use Monte Carlo Markov chain (MCMC) sampling to determine a maximum likelihood solution, solving for a constant shift Δ in distance modulus of each method against the CMD isochrone fitting distances as well as additional systematic errors ϵ of each method. The RR Lyrae distance moduli are on average about $\Delta_{RRL} = 0.021$ mag smaller than the CMD fitting and our subdwarf distance moduli are smaller by about 0.025 mag. The MCMC sampling also indicates additional errors of order 0.02 mag for the CMD and RR Lyrae distance moduli and 0.04 mag for the eclipsing binary ones. It finally finds an error of 0.08 mag for our subdwarf distance moduli. The insets compare the distance moduli for individual clusters. Clusters with $E(B - V) < 0.40$ that are used for the comparison are shown in blue, clusters with $E(B - V) > 0.40$ are shown in grey.

into agreement with the other literature data. We finally shifted the distances that Recio-Blanco et al. (2005) derived from CMD fitting down by 0.10 mag since we found a systematic bias of this size when comparing their distances with other literature distances.

In order to assess the accuracy of the derived distances and the reliability of the quoted errors, we compare in Fig. 5 the mean distance moduli calculated from various methods (isochrone fitting of CMDs, visible light RR Lyrae P/L relations, eclipsing binaries and infrared RR Lyrae P/L relations

and a combination of all other literature methods) plus the distance moduli we derived from subdwarfs with each other. For each cluster we take a weighted average of all individual measurements of a given type. We split the RR Lyrae distances into distances derived from visible or infrared P/L relations, since infrared P/L relations are usually thought to be more accurate (e.g. Bono et al. 2016). We also group the infrared P/L distances together with the EB distances to have a larger sample of clusters with very accurate distances. For each cluster we calculate average distance moduli for each method separately and then use Monte Carlo Markov chain (MCMC) sampling and maximum likelihood optimisation to determine possible shifts Δ between the CMD distance moduli and the other distance moduli, as well as additional systematic errors ϵ that could still be present in the data. We use only clusters with $E(B - V) < 0.4$ mag for the comparison since more strongly reddened clusters show larger deviations between the individual measurements, and would therefore require a separate treatment. We compare all distance moduli against the CMD fitting ones since these are available for the largest number of clusters.

It can be seen that the RR Lyrae distance moduli are smaller by $\Delta_{RRL} = -0.021$ mag compared to the CMD fitting ones, which is significant at the 2σ level. Our subdwarf distance moduli are also smaller, while the other methods show no statistically significant offset to the CMD distances. Since, without independent information, it is not possible to determine which of these distance scales is closer to the true distances, we do not apply shifts to any individual method and perform a straight averaging of the individual measurements instead. Our MCMC sampling also finds evidence for additional systematic errors of $\epsilon \approx 0.023$ in the CMD fitting and RR Lyrae distance moduli and additional systematic errors of $\epsilon_{EB} \approx 0.038$ mag in the eclipsing binary/IR RR Lyrae distance moduli. The MCMC sampling finally shows that our subdwarf distance moduli have errors of about $\epsilon_{SD} = 0.077$ mag, which we use when calculating the mean distance moduli.

Adding the above systematic errors in quadrature to the individual errors for the CMD, RR Lyrae and eclipsing binary distances, we then calculate a mean literature distance modulus and its formal error for each cluster from the mean distance moduli of each individual method. We also calculated a reduced χ_r^2 value of all distance determinations according to

$$\chi_r^2 = \frac{1}{N-1} \sum_i (\langle \mu_{Lit} \rangle - \mu_i)^2 / \sigma_i^2 \quad (2)$$

where $\langle \mu_{Lit} \rangle$ and μ_i are the average distance modulus and the individual distance moduli respectively and σ_i is the error of the individual measurements. For clusters with $\chi_r^2 > 1$, i.e. a larger than expected scatter of the individual measurements, we increase the final distance error by the square root of χ_r^2 . Table 2 gives the average distance and its 1σ upper and lower error that we obtain after averaging the literature distances for each cluster in this way. For easier comparison with the other methods, we give the literature data in linear distances, however when calculating a final value for the distance we use the distance modulus as explained below. Plots depicting the individual measurements for each cluster can be found in the Appendix.

4 RESULTS

4.1 Calculation of final distances

Fig. 6 compares the distances that we derive from the *Gaia* EDR3 data (separated into parallax and kinematic distances), the *HST* kinematic distances and the star count distances with the mean literature distances determined in the previous section. We again use MCMC sampling and determine offsets between the distances as well as additional unaccounted for errors. We restrict ourselves again to clusters with $E(B-V) < 0.4$ mag for which the distances should be least influenced by reddening uncertainties.

We find a constant shift of the *Gaia* parallax distances of $\Delta\varpi = 0.007$ mas, confirming the results of VB21. There is no evidence for a significant shift of the CMD distances against the other methods. However, given that the error bar on Δ_{CMD} is about 0.04, the RR Lyrae distances would also be in statistical agreement with the distances that we determined from the *Gaia* EDR3 data. The MCMC sampling finds $\Delta D_{Gaia} = -0.016 \pm 0.020$, implying that the *Gaia* kinematic distances are in statistical agreement with the other methods. However the *HST* kinematic distances are smaller by about 3.0%. There is also some evidence for significant, additional unaccounted for errors in the *HST* kinematic distances. We therefore add an error equal to 0.017 times the distance in quadrature to the formal distance error of the *HST* distances for each cluster. We do not apply a shift to the *HST* kinematic distances since it is first not clear which method gives the correct distance, and also because we found the *HST* and *Gaia* kinematic distances to be in agreement with each other, meaning that the error might well be with the CMD distances. The MCMC analysis finally shows that the star count distances need to be increased by a factor $1/0.93 = 1.075$ and that their uncertainties have an additional systematic contribution of 4.4% of the cluster distances.

After increasing the star count distances and adding additional errors to the *HST* kinematic and star count distances, we determine the final distance for each cluster by minimizing the combined likelihood of all measurements according to:

$$\ln L = -\frac{1}{2} \frac{(\varpi_G - \frac{1}{\langle D \rangle})^2}{\epsilon_\varpi^2} - \frac{1}{2} \sum_i \frac{(D_i - \langle D \rangle)^2}{\sigma_i^2} - \frac{1}{2} \sum_j \frac{(\mu_j - 5 \log \langle D \rangle + 5)^2}{\sigma_j^2} \quad (3)$$

Here ϖ_G and ϵ_ϖ are the cluster parallaxes and their 1σ errors, D_i and σ_i are the cluster distances and associated 1σ errors of the kinematic, star count and moving group distances. μ_j and σ_j are the distance moduli and error bars that we obtain from the averaging of the literature data and our subdwarf fits. $\langle D \rangle$ is the mean cluster distance that we want to determine. We use the *Gaia* parallaxes here instead of the distances that can be calculated from them since errors on the parallax distance are Gaussian only in parallax space. For the same reason we use distance moduli for the literature and subdwarf distances. We calculate the mean distance from the point where $\ln L$ has a maximum and calculate the associated upper and lower distance errors from the condition that $\Delta \ln L = 1.0$. The resulting mean

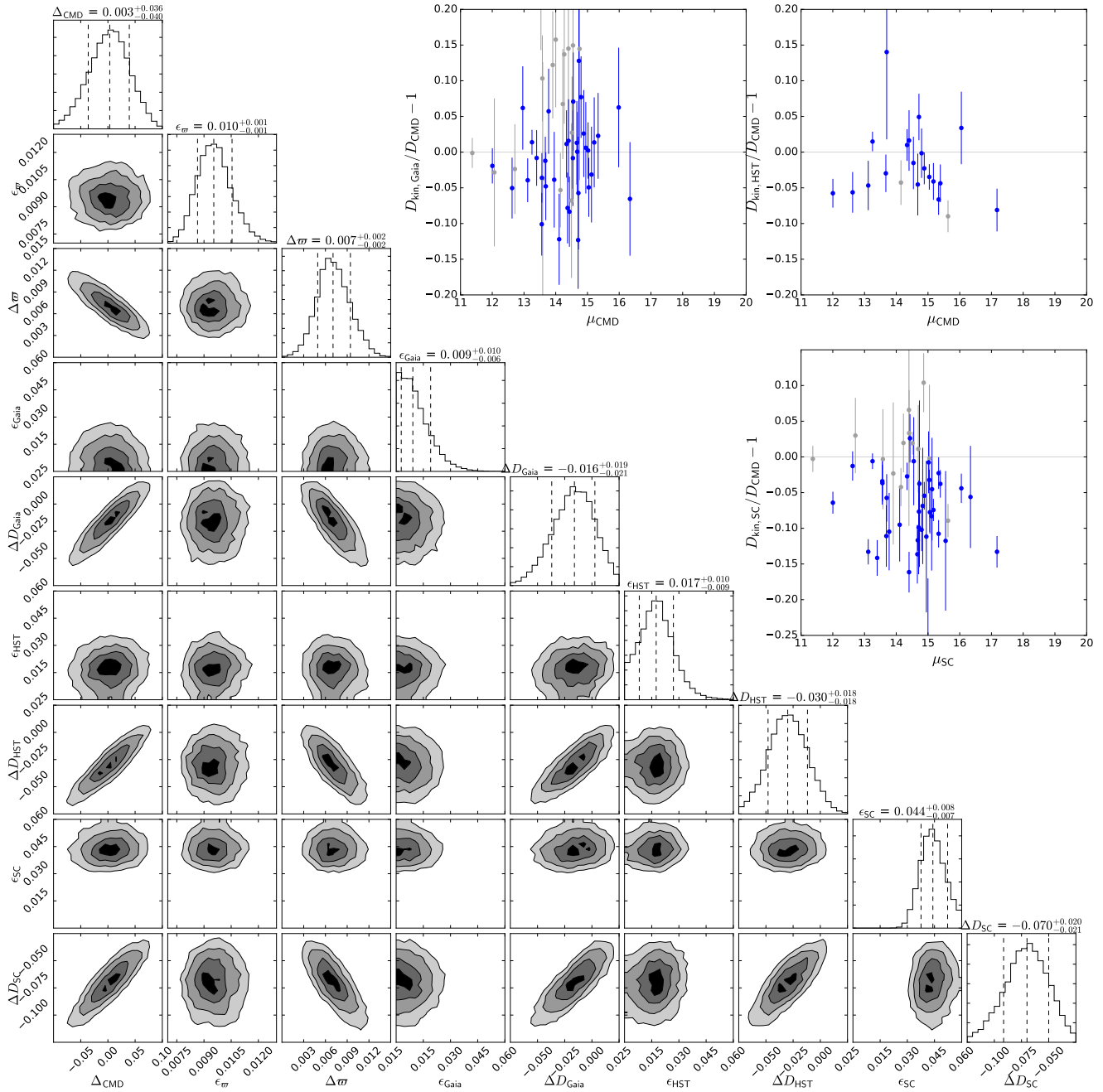


Figure 6. Comparison of the CMD fitting distances with the Gaia parallax and kinematic distances and the *HST* kinematic distances. We again use MCMC sampling and solve for constant scale factors ΔD in the distance scales of the various methods as well as additional systematic errors ϵ . ΔD_{Gaia} and ΔD_{HST} are relative shifts in the kinematic distances of the *Gaia* and *HST* kinematic distances and $\Delta\varpi$ is a shift in the Gaia parallaxes. We obtain a significant shift in the Gaia parallaxes of $\Delta\varpi \approx 0.007$ mas, in agreement with VB21. The *HST* kinematic distances are on average also smaller than the literature distances by about 3.0%, while the Gaia kinematic distance shift ΔD_{Gaia} is compatible with zero. The *HST* kinematic distances also show evidence of additional relative distance errors of about 1.7%. The inset compares the kinematic and star count distances with the distances from isochrone fitting of the cluster CMDs.

distances along with the individual values from the various methods are given in Table 2. All data has been transformed to linear distances to make the different measurements easier comparable with each other.

Fig.7 depicts the relative distance accuracy that we achieve by combining all data as a function of the cluster reddening. It can be seen that for clusters with low reddening

values $E(B - V) < 0.3$ we achieve relative accuracies of about 1%. For larger reddening values $E(B - V) > 0.3$ there is a continuous rise of the distance errors and we achieve only 20% accuracy for the most highly reddened clusters. This rise could partly be driven by the fact that heavily reddened clusters have often only few individual distance determinations.

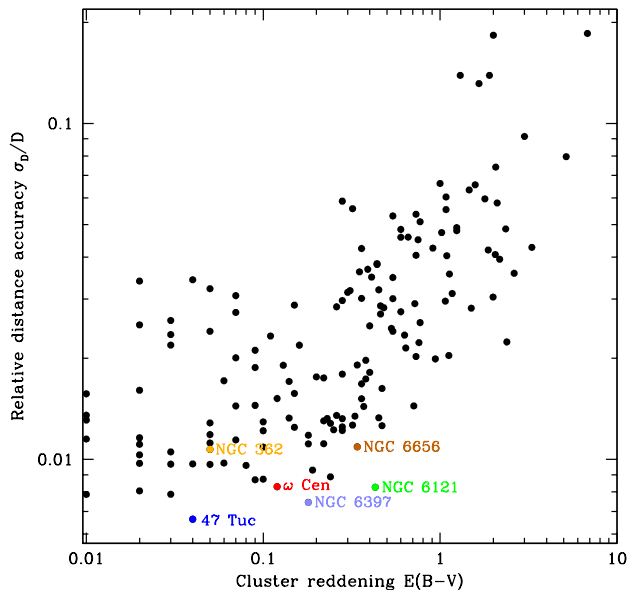


Figure 7. Final distance error σ_D/D as a function of the cluster reddening $E(B-V)$. Clusters with reddening values $E(B-V) < 0.20$ have an average distance error of about 1%. More reddened clusters show a continuous increase of the distance error with reddening. The location of three of the clusters discussed in the text is marked in the plot.

4.2 Individual clusters

4.2.1 47 Tuc

We derive a distance of $D = 4.52 \pm 0.03$ kpc to 47 Tuc (NGC 104). For 47 Tuc, both literature distances and kinematic distances have small formal errors and are fully consistent with each other (see Fig. 8). Our mean distance also agrees very well with the value of $D = 4.53 \pm 0.06$ kpc that Maíz Apellániz, Pantaleoni González & Barbá (2021) determined from the *Gaia* EDR3 parallaxes, correcting for the small scale angular covariances in the *Gaia* data by comparing the parallaxes of 47 Tuc stars with those of background SMC stars. It also agrees very well with the distance of $D = 4.45 \pm 0.12$ kpc that Chen et al. (2018) derived with the same method from *Gaia* DR2 data as well as the distance of $D = 4.53 \pm 0.05$ kpc that Thompson et al. (2020) found from the analysis of two detached eclipsing binaries in the cluster. The distance to 47 Tuc therefore seems to be established with an accuracy of better than 1%.

4.2.2 NGC 362

We correct the *Gaia* EDR3 parallaxes in the same way done by Maíz Apellániz, Pantaleoni González & Barbá (2021) for NGC 104 and Chen et al. (2018) for NGC 104 and NGC 362. We again use SMC field stars in the direction of NGC 362 as reference, assuming a distance of $D = 62.1 \pm 1.9$ kpc as distance to the SMC (Cioni et al. 2000; Graczyk et al. 2014). The resulting cluster parallax is $\varpi = 109.9 \pm 3.7 \mu\text{as}$, corresponding to a distance of $9.10^{+0.32}_{-0.30}$ kpc. This distance is in agreement with the earlier value of Chen et al. (2018) ($D = 8.54 \pm 0.48$ kpc) as well as the distance we derive from

an averaging of literature values (8.80 ± 0.11 kpc) and our own kinematic distance determinations (see Fig. 8).

4.2.3 ω Cen

There is also good agreement in our distance determinations for ω Cen. The literature distances lead to an average distance of $D = 5.47 \pm 0.06$ kpc (see Fig. 8). The *Gaia* kinematic distance is in good agreement with the literature distance, however the *HST* kinematic distance (5.26 ± 0.12 kpc) is about 200 pc shorter. One possible reason for the mismatch could be the intrinsic flattening of ω Cen. Mackey & Gilmore (2004) find an ellipticity of $\epsilon = 0.17$ for ω Cen based on its projected isophotes. The true flattening is likely even larger, with the exact value depending on the cluster inclination. van de Ven et al. (2006) found through axisymmetric Schwarzschild modeling that the resulting flattening of the velocity ellipsoid can decrease the kinematic cluster distance to ω Cen by several hundred pc if the flattening is not taken into account in the modeling. Since the N -body models that we use to derive the kinematic distances are spherically symmetric, there is a chance that our kinematic distances underestimate the true distance to ω Cen. This effect is much less likely for most other clusters which have much smaller relaxation times and should therefore be closer to being spherically symmetric. This is indeed also seen in observations (e.g. White & Shawl 1987). We therefore regard the literature distance as more reliable for ω Cen. The *Gaia* EDR3 parallaxes after application of the systematic parallax offset also favor a longer distance, however the error bar is too large to be decide between the two possibilities.

4.2.4 NGC 6121

We derive a distance of $D = 1.851 \pm 0.015$ kpc to M4 (NGC 6121). This distance is slightly larger than the distance of $D = 1.82 \pm 0.04$ kpc found by Kaluzny et al. (2013) based on three eclipsing binary stars as well as recent results from RR Lyrae stars (e.g. Braga et al. 2015; Neeley et al. 2019; Bhardwaj et al. 2020) (see Fig. 8). Nevertheless their distances are compatible with our distance within the error bars. The true distance to NGC 6121 is therefore likely somewhere in the range 1.83 to 1.85 kpc, making M4 another cluster whose distance is determined with an accuracy of about 1%.

4.2.5 NGC 6397 and NGC 6656

NGC 6397 and NGC 6656 (M 22) are among the closest globular clusters to the Sun. Their small distances together with their low reddening make them ideal targets for globular cluster studies, so a large amount of observational data exists for both clusters. For NGC 6397 we find a total of 27 individual distance determinations in the literature, from which we derive a mean cluster distance of 2.521 ± 0.025 kpc. Despite a relative distance error of only about 1% or the literature distance and similarly small errors for most of the other methods, most distances are in good statistical agreement with each other, with the exception of the *HST* kinematic distances that are too short by about 100 pc. Taking the average over all methods, we derive a distance

of 2.488 ± 0.019 kpc for NGC 6397, making this cluster the second closest cluster to the Sun. There is a similar good agreement in the individual distances values for NGC 6656, for which we derive a mean distance of $D = 3.307 \pm 0.037$ kpc.

4.3 Absolute luminosity of the TRGB and the value of H_0

Globular clusters can be used to determine the absolute luminosity of the tip of the red giant branch (TRGB), which in turn can be used to measure the distance to nearby galaxies. Using *Gaia* EDR3 parallaxes, Soltis, Casertano & Riess (2021) recently derived a distance of 5.24 ± 0.11 kpc to ω Cen. Using this distance, they derived an absolute I-band magnitude of the TRGB of $M_{I,TRGB} = -3.97 \pm 0.06$, from which they deduced a value of the local Hubble constant of $H_0 = 71.2 \pm 2.0$ km/sec. In contrast, Freedman et al. (2020) used stars in the LMC to derive an absolute TRGB magnitude of $M_{I,TRGB} = -4.05 \pm 0.06$, using eclipsing binaries in 47 Tuc and the SMC to calibrate the LMC distance.

The ω Cen distance of Soltis, Casertano & Riess (2021) was based on a direct averaging of the *Gaia* EDR3 parallaxes of individual member stars, applying only the Lindgren et al. (2020) parallax corrections. Their parallax value did not take systematic biases in the *Gaia* parallaxes or small scale correlated errors into account. Accounting for both, we derived a parallax of $\varpi = 182.3 \pm 9.5 \mu\text{as}$ for ω Cen (Vasiliev & Baumgardt 2021), corresponding to a distance $D = 5.48 \pm 0.24$ kpc, slightly larger than Soltis, Casertano & Riess (2021) and also with a larger formal error than found by them. Combining this data with the other distances, we then derive a distance of $D = 5.43 \pm 0.05$ to ω Cen. A similar analysis as the one done by Soltis, Casertano & Riess (2021) leads to an absolute TRGB magnitude of $M_{I,TRGB} = -4.06 \pm 0.06$, confirming the value found by Freedman et al. (2020). In addition, our results also confirm their adopted distance to NGC 104. The resulting value of the local Hubble constant of $H_0 = 69.4 \pm 2.0$ km/sec would be in better agreement with the expected value based on the Planck data of 67.4 ± 0.5 km/sec (Verde, Treu & Riess 2019).

5 CONCLUSIONS

We have derived mean distances to globular clusters using a combination of our own measurements based on *Gaia* EDR3 data and published literature distances. We derived our own distances using six different methods: *Gaia* ED3 parallaxes, kinematic distances using proper motion velocity dispersion profiles based on *Gaia* EDR3 proper motions, fitting nearby subdwarfs to the globular cluster main sequences where the distances and absolute luminosities of the subdwarfs are calculated from their *Gaia* parallaxes and moving group distances based on *Gaia* ED3 proper motions. In addition, we also derive kinematic distances from *HST* proper motion velocity dispersion profiles and distances using *HST* star counts in combination with the cluster kinematics.

Apart from a bias in the *Gaia* EDR3 parallaxes, we find good internal agreement among the distances calculated with the different methods and also with published distances

in the literature down to a level of about 2%. There is a possibility that our *HST* kinematic distances could slightly underestimate the distances to globular clusters, however the difference that we see could also signify a problem in the isochrone fitting distances. We also find some evidence that isochrone based distance moduli are larger than RR Lyrae based ones by about 0.02 mag.

Averaging over the various distance determinations, we are able to determine distances to a number of nearby globular clusters with an accuracy of 1%, making these clusters valuable objects for the establishment of a cosmic distance ladder. In particular, our results for the distances to 47 Tuc and ω Cen argue for an absolute TRGB magnitude of $M_{I,TRGB} = -4.05$ leading to a value of the local Hubble constant that is in agreement with the expected value based on Planck data. They however do not remove the tension between the Cepheid based value of H_0 and the Planck data, which is currently significant at about the 4σ level (Riess et al. 2019). Given that we find that the different literature distances to globular clusters are consistent down to a level of about 1-2%, it is also unlikely that our results would lead to a significant revision of the distance modulus to nearby galaxies like the LMC, and therefore a reduction of the tension in H_0 .

Future releases of the *Gaia* catalogue will further increase the sample of globular clusters with highly accurate distances by reducing the random and systematic errors in the parallaxes and proper motions of stars. There is currently also still a substantial uncertainty in the distances of highly reddened clusters, where individual distances can deviate from each other by up to a factor of two. At least for the more nearby clusters, *Gaia* parallaxes and proper motion velocity dispersion profiles based on future *Gaia* data releases should bring a significant improvement to the distances to these clusters.

ACKNOWLEDGMENTS

EV acknowledges support from STFC via the Consolidated grant to the Institute of Astronomy. We thank Domenico Nardiello for providing us with the HST photometry for NGC 6626. This work presents results from the European Space Agency (ESA) space mission *Gaia*. *Gaia* data are being processed by the Gaia Data Processing and Analysis Consortium (DPAC). Funding for the DPAC is provided by national institutions, in particular the institutions participating in the Gaia MultiLateral Agreement (MLA). This work is also based on observations made with the NASA/ESA Hubble Space Telescope, obtained from the data archive at the Space Telescope Science Institute. STScI is operated by the Association of Universities for Research in Astronomy, Inc. under NASA contract NAS 5-26555.

DATA AVAILABILITY

The distances and the fit results of our N -body models to Galactic globular clusters using these distances can be obtained from the following webpage: <https://people.smp.uq.edu.au/HolgerBaumgardt/globular/>

REFERENCES

- Alonso-García J., Dékány I., Catelan M., Contreras Ramos R., Gran F., Amigo P., Leyton P., Minniti D., 2015, *AJ*, 149, 99
- Baumgardt H., 2017, *MNRAS*, 464, 2174
- Baumgardt H. et al., 2019a, *MNRAS*, 488, 5340
- Baumgardt H., Hilker M., 2018, *MNRAS*, 478, 1520
- Baumgardt H., Hilker M., Sollima A., Bellini A., 2019b, *MNRAS*, 482, 5138
- Baumgardt H., Makino J., 2003, *MNRAS*, 340, 227
- Baumgardt H., Sollima A., Hilker M., 2020, *PASA*, 37, e046
- Bhardwaj A., 2020, *Journal of Astrophysics and Astronomy*, 41, 23
- Bhardwaj A. et al., 2020, arXiv e-prints, arXiv:2012.13495
- Bonatto C., Campos F., Kepler S. O., 2013, *MNRAS*, 435, 263
- Bono G. et al., 2016, *Mem. Soc. Astron. Italiana*, 87, 358
- Bono G., Caputo F., Di Criscienzo M., 2007, *A&A*, 476, 779
- Borissova J., Ivanov V. D., Stephens A. W., Catelan M., Minniti D., Prieto G., 2007, *A&A*, 474, 121
- Braga V. F. et al., 2015, *ApJ*, 799, 165
- Bressan A., Marigo P., Girardi L., Salasnich B., Dal Cero C., Rubele S., Nanni A., 2012, *MNRAS*, 427, 127
- Brown A., 1950, *ApJ*, 112, 225
- Cantat-Gaudin T. et al., 2018, *A&A*, 618, A93
- Carraro G., 2009, *AJ*, 137, 3809
- Carretta E., Bragaglia A., Gratton R., D’Orazi V., Lucatello S., 2009, *A&A*, 508, 695
- Casagrande L., Ramírez I., Meléndez J., Bessell M., Asplund M., 2010, *A&A*, 512, A54
- Catelan M., Pritzl B. J., Smith H. A., 2004, *ApJS*, 154, 633
- Cerny W., Freedman W. L., Madore B. F., Ashmead F., Hoyt T., Oakes E., Quang Hoang Tran N., Moss B., 2020, arXiv e-prints, arXiv:2012.09701
- Chen S., Richer H., Caiazzo I., Heyl J., 2018, *ApJ*, 867, 132
- Cioni M. R. L., van der Marel R. P., Loup C., Habing H. J., 2000, *A&A*, 359, 601
- Cohen R. E., Bellini A., Libralato M., Correnti M., Brown T. M., Kalirai J. S., 2021, *AJ*, 161, 41
- Cohen R. E., Sarajedini A., 2012, *MNRAS*, 419, 342
- Dambis A. K. et al., 2014, *MNRAS*, 439, 3765
- de Bruijne J. H. J., 1999, *MNRAS*, 306, 381
- Dixon R. I., Longmore A. J., 1993, *MNRAS*, 265, 395
- Dotter A., Sarajedini A., Anderson J., 2011, *ApJ*, 738, 74
- Dotter A. et al., 2010, *ApJ*, 708, 698
- Ebrahimi H., Sollima A., Haghi H., Baumgardt H., Hilker M., 2020, *MNRAS*, 494, 4226
- Feast M., Whitelock P., Menzies J., 2002, *MNRAS*, 329, L7
- Fernández-Trincado J. G. et al., 2021, arXiv e-prints, arXiv:2102.01088
- Fernley J., Barnes T. G., Skillen I., Hawley S. L., Hanley C. J., Evans D. W., Solano E., Garrido R., 1998, *A&A*, 330, 515
- Ferraro F. R., Messineo M., Fusi Pecci F., de Palo M. A., Straniero O., Chieffi A., Limongi M., 1999, *AJ*, 118, 1738
- Freedman W. L. et al., 2020, *ApJ*, 891, 57
- Gaia Collaboration, Brown A. G. A., Vallenari A., Prusti T., de Bruijne J. H. J., Babusiaux C., Biermann M., 2020, arXiv e-prints, arXiv:2012.01533
- Gaia Collaboration et al., 2016, *A&A*, 595, A1
- Giesers B. et al., 2019, *A&A*, 632, A3
- Gontcharov G. A., Mosenkov A. V., Khovritchev M. Y., 2019, *MNRAS*, 483, 4949
- Graczyk D. et al., 2014, *ApJ*, 780, 59
- Häberle M. et al., 2021, arXiv e-prints, arXiv:2102.07782
- Hamren K. M., Smith G. H., Guhathakurta P., Dolphin A. E., Weisz D. R., Rajan A., Grillmair C. J., 2013, *AJ*, 146, 116
- Harris W. E., 1996, *AJ*, 112, 1487
- Hénault-Brunet V., Gieles M., Sollima A., Watkins L. L., Zocchi A., Claydon I., Pancino E., Baumgardt H., 2019, *MNRAS*, 483, 1400
- Hendricks B., Stetson P. B., VandenBerg D. A., Dall’Ora M., 2012, *AJ*, 144, 25
- Hernitschek N. et al., 2019, *ApJ*, 871, 49
- Heyl J., Caiazzo I., Richer H., Anderson J., Kalirai J., Parada J., 2017, *ApJ*, 850, 186
- Heyl J. S. et al., 2012, *ApJ*, 761, 51
- Hilker M., 2006, *A&A*, 448, 171
- Ivanov V. D., Borissova J., 2002, *A&A*, 390, 937
- Kaluzny J., Rucinski S. M., Thompson I. B., Pych W., Krzeminski W., 2007, *AJ*, 133, 2457
- Kaluzny J. et al., 2013, *AJ*, 145, 43
- Kamann S. et al., 2018, *MNRAS*, 473, 5591
- Kerber L. O., Nardiello D., Ortolani S., Barbuy B., Bica E., Cassisi S., Libralato M., Vieira R. G., 2018, *ApJ*, 853, 15
- Laevens B. P. M. et al., 2015, *ApJ*, 813, 44
- Lagioia E. P. et al., 2014, *ApJ*, 782, 50
- Libralato M., Bellini A., Piotto G., Nardiello D., van der Marel R. P., Anderson J., Bedin L. R., Vesperini E., 2019, *ApJ*, 873, 109
- Lindgren L. et al., 2020, arXiv e-prints, arXiv:2012.01742
- Longeard N. et al., 2020, arXiv e-prints, arXiv:2005.05976
- Longeard N., Martin N., Ibata R. A., Collins M. L. M., Laevens B. P. M., Bell E., Mackey D., 2019, *MNRAS*, 490, 1498
- Lützgendorf N., Kissler-Patig M., Noyola E., Jalali B., de Zeeuw P. T., Gebhardt K., Baumgardt H., 2011, *A&A*, 533, A36
- Mackey A. D., Gilmore G. F., 2004, *MNRAS*, 355, 504
- Maíz Apellániz J., Pantaleoni González M., Barbá R. H., 2021, arXiv e-prints, arXiv:2101.10206
- Matsunaga N. et al., 2006, *MNRAS*, 370, 1979
- McNamara B. J., Harrison T. E., Baumgardt H., 2004, *ApJ*, 602, 264
- McNamara B. J., Harrison T. E., Baumgardt H., Khalaj P., 2012, *ApJ*, 745, 175
- Milone A. P., Piotto G., Bedin L. R., Cassisi S., Anderson J., Marino A. F., Pietrinferni A., Aparicio A., 2012, *A&A*, 537, A77
- Minniti D. et al., 2011, *A&A*, 527, A81
- Mutlu-Pakdil B. et al., 2018, *ApJ*, 863, 25
- Neeley J. R. et al., 2019, *MNRAS*, 490, 4254
- Pallanca C., Ferraro F. R., Lanzoni B., Saracino S., Raso S., Focardi P., 2019, *ApJ*, 882, 159
- Raso S. et al., 2020, *ApJ*, 895, 15
- Recio-Blanco A. et al., 2005, *A&A*, 432, 851
- Reid I. N., Gizis J. E., 1998, *AJ*, 116, 2929
- Riess A. G., Casertano S., Yuan W., Macri L. M., Scolnic D., 2019, *ApJ*, 876, 85

- Ripepi V., Molinaro R., Musella I., Marconi M., Leccia S., Eyer L., 2019, *A&A*, 625, A14
- Ryu J., Lee M. G., 2018, *ApJ*, 863, L38
- Sarajedini A. et al., 2007, *AJ*, 133, 1658
- Sirianni M. et al., 2005, *PASP*, 117, 1049
- Sollima A., Beccari G., Ferraro F. R., Fusi Pecci F., Sarajedini A., 2007, *MNRAS*, 380, 781
- Sollima A., Cacciari C., Valenti E., 2006, *MNRAS*, 372, 1675
- Soltis J., Casertano S., Riess A. G., 2021, *ApJ*, 908, L5
- Thompson I. B. et al., 2020, *MNRAS*, 492, 4254
- Tiongco M. A., Vesperini E., Varri A. L., 2016, *MNRAS*, 455, 3693
- Valcin D., Bernal J. L., Jimenez R., Verde L., Wandelt B. D., 2020, *Journal of Cosmology and Astroparticle Physics*, 2020, 002
- van de Ven G., van den Bosch R. C. E., Verolme E. K., de Zeeuw P. T., 2006, *A&A*, 445, 513
- van Leeuwen F., Le Poole R. S., Reijns R. A., Freeman K. C., de Zeeuw P. T., 2000, *A&A*, 360, 472
- VandenBerg D. A., Brogaard K., Leaman R., Casagrande L., 2013, *ApJ*, 775, 134
- Vasiliev E., Baumgardt H., 2021, *ArXiv e-prints*
- Verde L., Treu T., Riess A. G., 2019, *Nature Astronomy*, 3, 891
- Watkins L. L., van der Marel R. P., Bellini A., Anderson J., 2015a, *ApJ*, 803, 29
- Watkins L. L., van der Marel R. P., Bellini A., Anderson J., 2015b, *ApJ*, 812, 149
- White R. E., Shawl S. J., 1987, *ApJ*, 317, 246

APPENDIX A: COMPARISON OF DISTANCE DETERMINATIONS FOR GLOBULAR CLUSTERS

Figs. 8 to 29 depict the individual distances determinations to globular clusters used in this work. Only clusters with more than 5 measurements are shown.

APPENDIX B: LITERATURE DISTANCES USED IN THIS WORK

Table 2. Derived distances of the studied globular clusters. The final column lists the number of independent distance determinations used to calculate the mean distance. The *Gaia* EDR3 parallax distances give the mean and 1σ uncertainty of the distance. We have applied shifts to the star count distances and *Gaia* parallaxes to bring all distances to a common scale and also have added systematic errors as described in the text.

Name	GEDR3 parallax dist. [kpc]	GEDR3 kin. dist. [kpc]	HST kin. dist. [kpc]	Subdwarf dist. [kpc]	Star Count dist. [kpc]	Lit. dist. [kpc]	Mean distance [kpc]	N_{Tot}
2MASS-GC01	-	-	-	-	-	$3.373^{+0.682}_{-0.567}$	$3.373^{+0.682}_{-0.567}$	1
2MASS-GC02	-	-	-	-	-	$5.503^{+0.456}_{-0.421}$	$5.503^{+0.456}_{-0.421}$	2
AM 1	-	-	-	-	-	$118.905^{+3.444}_{-3.347}$	$118.905^{+3.444}_{-3.347}$	2
AM 4	-	-	-	-	-	$29.013^{+0.951}_{-0.920}$	$29.013^{+0.951}_{-0.920}$	2
Arp 2	-	-	-	$28.184^{+1.058}_{-1.019}$	-	$28.721^{+0.346}_{-0.342}$	$28.726^{+0.346}_{-0.342}$	11
BH 140	$4.808^{+0.258}_{-0.233}$	-	-	-	-	-	$4.808^{+0.258}_{-0.233}$	1
BH 261	-	-	-	-	-	$6.183^{+0.279}_{-0.267}$	$6.115^{+0.265}_{-0.253}$	4
Crater	-	-	-	-	-	$147.231^{+4.334}_{-4.210}$	$147.231^{+4.334}_{-4.210}$	3
Djor 1	-	-	-	-	-	$9.854^{+0.676}_{-0.632}$	$9.879^{+0.671}_{-0.628}$	4
Djor 2	-	-	-	-	-	$8.758^{+0.179}_{-0.176}$	$8.764^{+0.178}_{-0.174}$	5
E 3	$7.326^{+0.765}_{-0.633}$	-	-	-	-	$7.940^{+0.268}_{-0.259}$	$7.876^{+0.254}_{-0.245}$	3
ESO 280	-	-	-	-	-	$20.941^{+0.656}_{-0.636}$	$20.945^{+0.656}_{-0.636}$	3
ESO 452	-	-	-	-	-	$7.440^{+0.208}_{-0.203}$	$7.389^{+0.202}_{-0.196}$	4
Eridanus	-	-	-	-	-	$84.723^{+2.937}_{-2.839}$	$84.684^{+2.936}_{-2.838}$	1
FSR 1716	-	-	-	-	-	$7.321^{+0.275}_{-0.265}$	$7.431^{+0.270}_{-0.260}$	4
FSR 1735	-	-	-	-	-	$9.082^{+0.543}_{-0.512}$	$9.082^{+0.543}_{-0.512}$	4
FSR 1758	-	-	-	-	-	$11.482^{+0.832}_{-0.776}$	$11.085^{+0.764}_{-0.710}$	2
HP 1	-	-	-	-	-	$6.944^{+0.145}_{-0.142}$	$6.995^{+0.144}_{-0.141}$	10
IC 1257	-	-	-	-	-	$26.632^{+1.474}_{-1.397}$	$26.587^{+1.469}_{-1.392}$	2
IC 1276	$5.023^{+0.491}_{-0.411}$	-	-	-	-	$4.159^{+0.345}_{-0.318}$	$4.554^{+0.263}_{-0.243}$	3
IC 4499	-	-	-	$17.378^{+0.652}_{-0.629}$	-	$18.880^{+0.254}_{-0.250}$	$18.891^{+0.253}_{-0.250}$	11
Laevens 3	-	-	-	-	-	$61.773^{+1.672}_{-1.628}$	$61.767^{+1.672}_{-1.628}$	3
Liller 1	-	-	-	-	-	$8.061^{+0.353}_{-0.338}$	$8.061^{+0.353}_{-0.338}$	5
Lynge 7	-	-	-	$7.798^{+0.368}_{-0.351}$	-	$7.867^{+0.165}_{-0.161}$	$7.899^{+0.163}_{-0.159}$	8
Mercer 5	-	-	-	-	-	$5.495^{+0.533}_{-0.486}$	$5.466^{+0.523}_{-0.476}$	1
NGC 104	$4.367^{+0.189}_{-0.174}$	4.533 ± 0.067	4.522 ± 0.085	$4.406^{+0.165}_{-0.159}$	4.779 ± 0.197	$4.512^{+0.040}_{-0.039}$	$4.521^{+0.031}_{-0.031}$	33
NGC 288	$7.692^{+0.731}_{-0.615}$	9.814 ± 0.576	9.098 ± 0.348	$9.333^{+0.350}_{-0.338}$	8.798 ± 0.446	$8.983^{+0.096}_{-0.095}$	$8.988^{+0.089}_{-0.088}$	23
NGC 362	$9.099^{+0.317}_{-0.296}$	8.267 ± 0.646	9.202 ± 0.321	$8.790^{+0.330}_{-0.318}$	8.707 ± 0.374	$8.770^{+0.114}_{-0.112}$	$8.829^{+0.096}_{-0.096}$	21
NGC 1261	-	-	16.775 ± 0.872	$16.293^{+0.611}_{-0.589}$	16.680 ± 0.726	$16.353^{+0.205}_{-0.202}$	$16.400^{+0.192}_{-0.190}$	15
NGC 1851	-	-	11.440 ± 0.320	$12.303^{+0.462}_{-0.445}$	12.376 ± 0.528	$12.017^{+0.156}_{-0.154}$	$11.951^{+0.134}_{-0.133}$	18
NGC 1904	-	-	-	-	-	$13.080^{+0.182}_{-0.179}$	$13.078^{+0.181}_{-0.179}$	13
NGC 2298	-	-	-	$10.000^{+0.471}_{-0.450}$	7.471 ± 1.208	$9.890^{+0.175}_{-0.172}$	$9.828^{+0.170}_{-0.167}$	10
NGC 2419	-	-	-	-	-	$88.471^{+2.437}_{-2.371}$	$88.471^{+2.437}_{-2.371}$	6
NGC 2808	-	9.688 ± 0.428	9.837 ± 0.233	$10.280^{+0.435}_{-0.417}$	10.603 ± 0.494	$10.139^{+0.141}_{-0.139}$	$10.060^{+0.112}_{-0.111}$	20
NGC 3201	$4.819^{+0.239}_{-0.217}$	4.745 ± 0.176	-	$4.571^{+0.172}_{-0.165}$	4.416 ± 0.202	$4.749^{+0.046}_{-0.046}$	$4.737^{+0.043}_{-0.042}$	29
NGC 4147	-	-	-	$17.947^{+0.674}_{-0.649}$	-	$18.510^{+0.214}_{-0.212}$	$18.535^{+0.214}_{-0.212}$	16
NGC 4372	$5.688^{+0.425}_{-0.370}$	5.933 ± 0.423	-	-	4.593 ± 0.614	$5.959^{+0.385}_{-0.362}$	$5.713^{+0.214}_{-0.207}$	5
NGC 4590	-	-	-	$10.328^{+0.388}_{-0.374}$	10.396 ± 0.841	$10.409^{+0.101}_{-0.100}$	$10.404^{+0.100}_{-0.099}$	24
NGC 4833	$6.557^{+0.490}_{-0.426}$	5.822 ± 0.360	-	$6.546^{+0.246}_{-0.237}$	6.453 ± 0.395	$6.519^{+0.091}_{-0.089}$	$6.480^{+0.084}_{-0.083}$	12
NGC 5024	-	17.313 ± 1.353	-	$18.535^{+0.696}_{-0.670}$	18.803 ± 1.446	$18.518^{+0.189}_{-0.187}$	$18.498^{+0.185}_{-0.183}$	20
NGC 5053	-	-	-	$18.030^{+0.677}_{-0.652}$	-	$17.515^{+0.235}_{-0.232}$	$17.537^{+0.235}_{-0.232}$	20
NGC 5139	$5.485^{+0.302}_{-0.272}$	5.359 ± 0.141	5.264 ± 0.121	-	-	$5.468^{+0.056}_{-0.055}$	$5.426^{+0.047}_{-0.047}$	31
NGC 5272	-	10.116 ± 0.384	-	$9.638^{+0.362}_{-0.349}$	10.770 ± 0.610	$10.167^{+0.085}_{-0.084}$	$10.175^{+0.082}_{-0.081}$	38
NGC 5286	-	11.181 ± 0.689	-	$10.864^{+0.408}_{-0.393}$	-	$11.071^{+0.149}_{-0.147}$	$11.096^{+0.145}_{-0.143}$	13
NGC 5466	-	-	-	$15.776^{+0.592}_{-0.571}$	-	$16.106^{+0.164}_{-0.162}$	$16.120^{+0.164}_{-0.162}$	21
NGC 5634	-	-	-	-	-	$25.990^{+0.630}_{-0.615}$	$25.959^{+0.628}_{-0.613}$	4
NGC 5694	-	-	-	-	-	$34.834^{+0.746}_{-0.730}$	$34.840^{+0.745}_{-0.730}$	6

Table 2 – *continued*

Name	GEDR3 parallax dist. [kpc]	GEDR3 kin. dist. [kpc]	HST kin. dist. [kpc]	Subdwarf dist. [kpc]	Star Count dist. [kpc]	Lit. dist. [kpc]	Mean distance [kpc]	N_{Tot}
NGC 5824	-	-	-	-	-	$31.754^{+0.605}_{-0.594}$	$31.713^{+0.604}_{-0.593}$	5
NGC 5897	-	-	-	$12.359^{+0.464}_{-0.447}$	12.252 ± 1.141	$12.607^{+0.246}_{-0.241}$	$12.549^{+0.238}_{-0.233}$	8
NGC 5904	$7.651^{+0.677}_{-0.575}$	7.467 ± 0.357	7.456 ± 0.201	$7.551^{+0.283}_{-0.273}$	7.721 ± 0.350	$7.471^{+0.066}_{-0.065}$	$7.479^{+0.060}_{-0.060}$	38
NGC 5927	$8.606^{+0.900}_{-0.744}$	8.209 ± 0.647	-	$8.472^{+0.318}_{-0.306}$	8.757 ± 0.371	$8.215^{+0.118}_{-0.116}$	$8.270^{+0.111}_{-0.109}$	14
NGC 5946	-	-	-	-	-	$9.554^{+0.589}_{-0.555}$	$9.642^{+0.529}_{-0.496}$	4
NGC 5986	-	10.269 ± 0.668	-	$10.471^{+0.393}_{-0.379}$	10.885 ± 0.837	$10.549^{+0.137}_{-0.135}$	$10.540^{+0.132}_{-0.130}$	14
NGC 6093	-	-	-	$10.375^{+0.389}_{-0.375}$	10.193 ± 0.489	$10.342^{+0.120}_{-0.118}$	$10.339^{+0.116}_{-0.115}$	20
NGC 6101	-	-	-	$14.322^{+0.537}_{-0.518}$	-	$14.454^{+0.188}_{-0.185}$	$14.449^{+0.187}_{-0.184}$	13
NGC 6121	$1.830^{+0.035}_{-0.034}$	1.878 ± 0.033	-	$1.888^{+0.071}_{-0.068}$	2.016 ± 0.090	$1.839^{+0.020}_{-0.020}$	$1.851^{+0.015}_{-0.016}$	23
NGC 6139	-	-	-	-	-	$10.046^{+0.488}_{-0.465}$	$10.035^{+0.463}_{-0.441}$	6
NGC 6144	$8.292^{+0.866}_{-0.716}$	-	-	$8.511^{+0.319}_{-0.308}$	-	$8.147^{+0.129}_{-0.127}$	$8.151^{+0.127}_{-0.125}$	8
NGC 6171	$5.464^{+0.411}_{-0.357}$	6.017 ± 0.407	-	$5.998^{+0.254}_{-0.244}$	5.479 ± 0.407	$5.629^{+0.081}_{-0.080}$	$5.631^{+0.077}_{-0.076}$	18
NGC 6205	$8.621^{+0.822}_{-0.690}$	6.906 ± 0.336	-	$7.379^{+0.277}_{-0.267}$	-	$7.427^{+0.079}_{-0.078}$	$7.419^{+0.076}_{-0.075}$	25
NGC 6218	$5.068^{+0.282}_{-0.254}$	4.632 ± 0.194	-	$5.321^{+0.200}_{-0.192}$	5.352 ± 0.265	$5.136^{+0.052}_{-0.052}$	$5.109^{+0.049}_{-0.048}$	24
NGC 6229	-	-	-	-	-	$30.102^{+0.475}_{-0.468}$	$30.106^{+0.475}_{-0.467}$	7
NGC 6235	-	-	-	-	-	$11.896^{+0.395}_{-0.383}$	$11.937^{+0.387}_{-0.374}$	5
NGC 6254	$5.394^{+0.412}_{-0.358}$	4.976 ± 0.199	-	$4.989^{+0.235}_{-0.225}$	5.346 ± 0.310	$5.051^{+0.070}_{-0.069}$	$5.067^{+0.064}_{-0.063}$	19
NGC 6256	-	-	-	$7.516^{+0.650}_{-0.598}$	7.680 ± 0.804	$7.204^{+0.326}_{-0.312}$	$7.242^{+0.299}_{-0.288}$	9
NGC 6266	$5.764^{+0.426}_{-0.371}$	6.395 ± 0.327	6.502 ± 0.163	-	6.956 ± 0.325	$6.249^{+0.172}_{-0.167}$	$6.412^{+0.105}_{-0.104}$	13
NGC 6273	$7.657^{+0.683}_{-0.580}$	7.658 ± 0.424	-	-	8.463 ± 0.536	$8.527^{+0.203}_{-0.198}$	$8.343^{+0.165}_{-0.163}$	10
NGC 6284	-	-	-	-	-	$14.309^{+0.435}_{-0.422}$	$14.208^{+0.427}_{-0.415}$	6
NGC 6287	$7.184^{+0.721}_{-0.601}$	-	-	-	-	$8.143^{+0.427}_{-0.406}$	$7.929^{+0.376}_{-0.356}$	6
NGC 6293	-	-	-	-	9.273 ± 1.131	$9.209^{+0.297}_{-0.288}$	$9.192^{+0.282}_{-0.274}$	7
NGC 6304	$6.373^{+0.504}_{-0.435}$	7.304 ± 0.684	-	$5.702^{+0.214}_{-0.206}$	-	$6.059^{+0.161}_{-0.157}$	$6.152^{+0.150}_{-0.146}$	13
NGC 6316	-	9.631 ± 0.901	-	-	9.131 ± 1.785	$11.792^{+0.499}_{-0.479}$	$11.152^{+0.393}_{-0.382}$	7
NGC 6325	$6.627^{+0.646}_{-0.540}$	-	-	$8.241^{+0.795}_{-0.725}$	-	$7.755^{+0.369}_{-0.352}$	$7.533^{+0.330}_{-0.314}$	7
NGC 6333	$8.052^{+0.775}_{-0.650}$	-	-	-	-	$8.310^{+0.147}_{-0.144}$	$8.300^{+0.144}_{-0.142}$	8
NGC 6341	-	8.627 ± 0.473	8.231 ± 0.374	$8.872^{+0.333}_{-0.321}$	8.188 ± 0.345	$8.511^{+0.075}_{-0.074}$	$8.501^{+0.071}_{-0.070}$	35
NGC 6342	$7.716^{+0.787}_{-0.654}$	-	-	$8.054^{+0.302}_{-0.291}$	-	$8.043^{+0.244}_{-0.237}$	$8.013^{+0.233}_{-0.226}$	6
NGC 6352	$5.583^{+0.378}_{-0.333}$	-	6.260 ± 0.816	$5.702^{+0.214}_{-0.206}$	5.564 ± 0.295	$5.534^{+0.077}_{-0.076}$	$5.543^{+0.073}_{-0.072}$	16
NGC 6355	$7.236^{+0.707}_{-0.591}$	-	-	$8.472^{+0.318}_{-0.306}$	9.444 ± 0.449	$8.527^{+0.259}_{-0.251}$	$8.655^{+0.224}_{-0.220}$	8
NGC 6356	-	-	-	-	-	$15.900^{+0.973}_{-0.917}$	$15.656^{+0.946}_{-0.890}$	4
NGC 6362	$8.026^{+0.731}_{-0.618}$	7.717 ± 0.440	7.720 ± 0.341	$7.656^{+0.287}_{-0.277}$	6.849 ± 0.326	$7.677^{+0.071}_{-0.070}$	$7.649^{+0.067}_{-0.066}$	28
NGC 6366	$3.643^{+0.181}_{-0.165}$	3.404 ± 0.256	-	$3.548^{+0.167}_{-0.160}$	3.861 ± 0.297	$3.407^{+0.055}_{-0.054}$	$3.444^{+0.051}_{-0.050}$	14
NGC 6380	-	-	-	$9.550^{+0.358}_{-0.345}$	-	$9.532^{+0.312}_{-0.302}$	$9.607^{+0.306}_{-0.296}$	4
NGC 6388	-	-	10.894 ± 0.230	$10.765^{+0.404}_{-0.389}$	11.196 ± 0.466	$11.545^{+0.280}_{-0.273}$	$11.171^{+0.162}_{-0.161}$	15
NGC 6397	$2.458^{+0.061}_{-0.058}$	2.467 ± 0.056	2.371 ± 0.051	$2.410^{+0.090}_{-0.087}$	2.531 ± 0.107	$2.512^{+0.024}_{-0.024}$	$2.482^{+0.019}_{-0.019}$	29
NGC 6401	$7.283^{+0.781}_{-0.643}$	-	-	$8.204^{+0.308}_{-0.297}$	8.448 ± 0.376	$7.910^{+0.316}_{-0.304}$	$8.064^{+0.238}_{-0.234}$	7
NGC 6402	$8.482^{+0.847}_{-0.706}$	-	-	-	-	$9.204^{+0.267}_{-0.259}$	$9.144^{+0.255}_{-0.248}$	6
NGC 6426	-	-	-	$21.677^{+1.022}_{-0.976}$	-	$20.701^{+0.356}_{-0.350}$	$20.710^{+0.355}_{-0.349}$	8
NGC 6440	$7.283^{+0.742}_{-0.617}$	7.394 ± 0.776	-	-	-	$8.461^{+0.281}_{-0.272}$	$8.248^{+0.248}_{-0.241}$	7
NGC 6441	-	-	12.190 ± 0.244	-	13.095 ± 0.674	$13.176^{+0.245}_{-0.240}$	$12.728^{+0.163}_{-0.162}$	16
NGC 6453	-	-	-	-	11.149 ± 0.523	$9.804^{+0.238}_{-0.232}$	$10.070^{+0.220}_{-0.216}$	8
NGC 6496	-	9.823 ± 0.612	-	$9.204^{+0.345}_{-0.333}$	9.326 ± 0.988	$9.647^{+0.161}_{-0.159}$	$9.641^{+0.153}_{-0.151}$	11
NGC 6517	-	10.202 ± 1.704	-	-	-	$8.913^{+0.717}_{-0.664}$	$9.227^{+0.578}_{-0.538}$	4
NGC 6522	-	8.120 ± 0.929	-	-	-	$7.158^{+0.221}_{-0.214}$	$7.295^{+0.211}_{-0.205}$	8
NGC 6528	-	-	-	-	-	$7.791^{+0.244}_{-0.237}$	$7.829^{+0.239}_{-0.232}$	8

Table 2 – continued

Name	GEDR3 parallax dist. [kpc]	GEDR3 kin. dist. [kpc]	HST kin. dist. [kpc]	Subdwarf dist. [kpc]	Star Count dist. [kpc]	Lit. dist. [kpc]	Mean distance [kpc]	N_{Tot}
NGC 6535	$6.570^{+0.669}_{-0.556}$	-	-	$6.486^{+0.274}_{-0.263}$	-	$6.353^{+0.127}_{-0.125}$	$6.363^{+0.124}_{-0.122}$	8
NGC 6539	$8.292^{+0.866}_{-0.716}$	8.686 ± 0.746	-	-	8.694 ± 1.140	$7.565^{+0.609}_{-0.563}$	$8.165^{+0.395}_{-0.379}$	5
NGC 6540	-	-	-	-	-	$5.897^{+0.301}_{-0.286}$	$5.909^{+0.279}_{-0.265}$	4
NGC 6541	$7.429^{+0.648}_{-0.552}$	7.056 ± 0.324	-	$7.311^{+0.274}_{-0.264}$	8.493 ± 0.416	$7.617^{+0.113}_{-0.111}$	$7.609^{+0.102}_{-0.101}$	11
NGC 6544	$2.585^{+0.074}_{-0.070}$	2.516 ± 0.239	-	-	-	$2.589^{+0.113}_{-0.109}$	$2.582^{+0.059}_{-0.057}$	6
NGC 6553	$5.488^{+0.370}_{-0.326}$	6.211 ± 0.457	-	-	-	$5.219^{+0.141}_{-0.138}$	$5.332^{+0.128}_{-0.125}$	12
NGC 6558	-	-	-	$7.943^{+0.298}_{-0.287}$	-	$7.495^{+0.306}_{-0.294}$	$7.474^{+0.294}_{-0.282}$	6
NGC 6569	-	-	-	-	10.961 ± 1.031	$10.529^{+0.275}_{-0.268}$	$10.534^{+0.261}_{-0.255}$	9
NGC 6584	-	-	-	$12.647^{+0.475}_{-0.457}$	-	$13.602^{+0.177}_{-0.174}$	$13.611^{+0.176}_{-0.174}$	13
NGC 6624	-	8.027 ± 0.530	7.972 ± 0.308	$7.621^{+0.286}_{-0.276}$	-	$8.017^{+0.119}_{-0.117}$	$8.019^{+0.108}_{-0.107}$	15
NGC 6626	$5.297^{+0.325}_{-0.289}$	5.734 ± 0.306	-	-	5.571 ± 0.403	$5.311^{+0.114}_{-0.111}$	$5.368^{+0.099}_{-0.098}$	10
NGC 6637	-	9.960 ± 1.149	-	$9.204^{+0.345}_{-0.333}$	9.139 ± 1.054	$8.880^{+0.107}_{-0.106}$	$8.900^{+0.106}_{-0.104}$	17
NGC 6638	-	-	-	-	-	$9.786^{+0.363}_{-0.350}$	$9.775^{+0.347}_{-0.334}$	5
NGC 6642	-	-	-	$8.054^{+0.302}_{-0.291}$	-	$8.009^{+0.209}_{-0.204}$	$8.049^{+0.204}_{-0.198}$	7
NGC 6652	-	-	-	$9.506^{+0.357}_{-0.344}$	-	$9.467^{+0.141}_{-0.138}$	$9.464^{+0.139}_{-0.137}$	13
NGC 6656	$3.368^{+0.119}_{-0.111}$	3.181 ± 0.123	3.161 ± 0.088	$3.373^{+0.127}_{-0.122}$	3.556 ± 0.149	$3.327^{+0.049}_{-0.049}$	$3.303^{+0.037}_{-0.037}$	14
NGC 6681	-	9.722 ± 0.578	9.260 ± 0.228	$9.120^{+0.342}_{-0.330}$	9.634 ± 0.414	$9.354^{+0.130}_{-0.128}$	$9.362^{+0.107}_{-0.106}$	15
NGC 6712	$7.402^{+0.676}_{-0.571}$	7.463 ± 0.546	-	-	-	$7.355^{+0.294}_{-0.282}$	$7.382^{+0.240}_{-0.233}$	9
NGC 6715	-	-	25.019 ± 0.829	-	25.386 ± 1.185	$26.644^{+0.383}_{-0.378}$	$26.283^{+0.328}_{-0.325}$	17
NGC 6717	-	-	-	-	-	$7.464^{+0.135}_{-0.133}$	$7.524^{+0.133}_{-0.131}$	10
NGC 6723	$8.237^{+0.829}_{-0.690}$	8.708 ± 0.586	-	$8.472^{+0.318}_{-0.306}$	8.691 ± 0.601	$8.241^{+0.103}_{-0.102}$	$8.267^{+0.100}_{-0.099}$	18
NGC 6749	$7.849^{+0.779}_{-0.650}$	-	-	-	-	$7.561^{+0.230}_{-0.223}$	$7.591^{+0.218}_{-0.212}$	5
NGC 6752	$4.092^{+0.171}_{-0.158}$	4.036 ± 0.114	4.005 ± 0.147	$3.981^{+0.149}_{-0.144}$	3.917 ± 0.167	$4.176^{+0.050}_{-0.050}$	$4.125^{+0.041}_{-0.041}$	18
NGC 6760	$8.244^{+0.839}_{-0.697}$	9.322 ± 0.900	-	-	-	$8.110^{+0.600}_{-0.559}$	$8.411^{+0.441}_{-0.418}$	4
NGC 6779	-	-	-	$10.139^{+0.381}_{-0.367}$	-	$10.404^{+0.145}_{-0.143}$	$10.430^{+0.144}_{-0.142}$	12
NGC 6809	$5.020^{+0.285}_{-0.256}$	5.201 ± 0.246	-	$5.200^{+0.195}_{-0.188}$	5.223 ± 0.303	$5.370^{+0.055}_{-0.054}$	$5.348^{+0.052}_{-0.051}$	27
NGC 6838	$4.160^{+0.190}_{-0.174}$	4.154 ± 0.237	-	$4.036^{+0.151}_{-0.146}$	-	$3.977^{+0.053}_{-0.053}$	$4.001^{+0.050}_{-0.050}$	15
NGC 6864	-	-	-	-	-	$20.549^{+0.459}_{-0.449}$	$20.517^{+0.457}_{-0.448}$	5
NGC 6934	-	16.718 ± 1.382	-	$14.791^{+0.555}_{-0.535}$	-	$15.704^{+0.175}_{-0.173}$	$15.716^{+0.173}_{-0.171}$	19
NGC 6981	-	-	-	$16.069^{+0.603}_{-0.581}$	-	$16.672^{+0.185}_{-0.183}$	$16.661^{+0.185}_{-0.183}$	15
NGC 7006	-	-	-	$39.264^{+1.474}_{-1.420}$	-	$39.319^{+0.565}_{-0.557}$	$39.318^{+0.565}_{-0.557}$	9
NGC 7078	-	-	10.375 ± 0.295	$10.617^{+0.398}_{-0.384}$	10.769 ± 0.452	$10.740^{+0.104}_{-0.103}$	$10.709^{+0.096}_{-0.095}$	28
NGC 7089	-	11.940 ± 0.703	-	$11.169^{+0.419}_{-0.404}$	12.267 ± 0.543	$11.647^{+0.119}_{-0.117}$	$11.693^{+0.115}_{-0.114}$	21
NGC 7099	$7.981^{+0.753}_{-0.633}$	8.682 ± 0.496	-	$8.630^{+0.324}_{-0.312}$	7.959 ± 0.435	$8.480^{+0.094}_{-0.093}$	$8.458^{+0.090}_{-0.089}$	19
NGC 7492	-	-	-	-	-	$24.434^{+0.581}_{-0.567}$	$24.390^{+0.579}_{-0.566}$	4
Pal 1	-	-	-	$10.520^{+0.547}_{-0.520}$	-	$11.189^{+0.329}_{-0.320}$	$11.176^{+0.328}_{-0.319}$	4
Pal 2	-	-	-	-	-	$26.158^{+1.321}_{-1.258}$	$26.174^{+1.317}_{-1.253}$	2
Pal 3	-	-	-	-	-	$94.842^{+3.288}_{-3.178}$	$94.842^{+3.288}_{-3.178}$	2
Pal 4	-	-	-	-	-	$101.391^{+2.601}_{-2.536}$	$101.391^{+2.601}_{-2.536}$	2
Pal 5	-	-	-	-	-	$21.928^{+0.521}_{-0.509}$	$21.941^{+0.520}_{-0.508}$	6
Pal 6	-	-	-	-	-	$6.887^{+0.472}_{-0.442}$	$7.047^{+0.463}_{-0.433}$	6
Pal 8	-	-	-	-	-	$11.695^{+0.722}_{-0.680}$	$11.316^{+0.652}_{-0.611}$	4
Pal 10	-	-	-	-	-	$8.402^{+1.621}_{-1.359}$	$8.944^{+1.292}_{-1.072}$	3
Pal 11	-	-	-	-	-	$14.125^{+0.523}_{-0.505}$	$14.024^{+0.517}_{-0.498}$	3
Pal 12	-	-	-	$18.281^{+0.686}_{-0.661}$	-	$18.484^{+0.300}_{-0.296}$	$18.494^{+0.300}_{-0.295}$	8
Pal 13	-	-	-	-	-	$23.475^{+0.403}_{-0.397}$	$23.475^{+0.403}_{-0.397}$	6
Pal 14	-	-	-	-	-	$73.587^{+1.645}_{-1.609}$	$73.579^{+1.645}_{-1.609}$	4

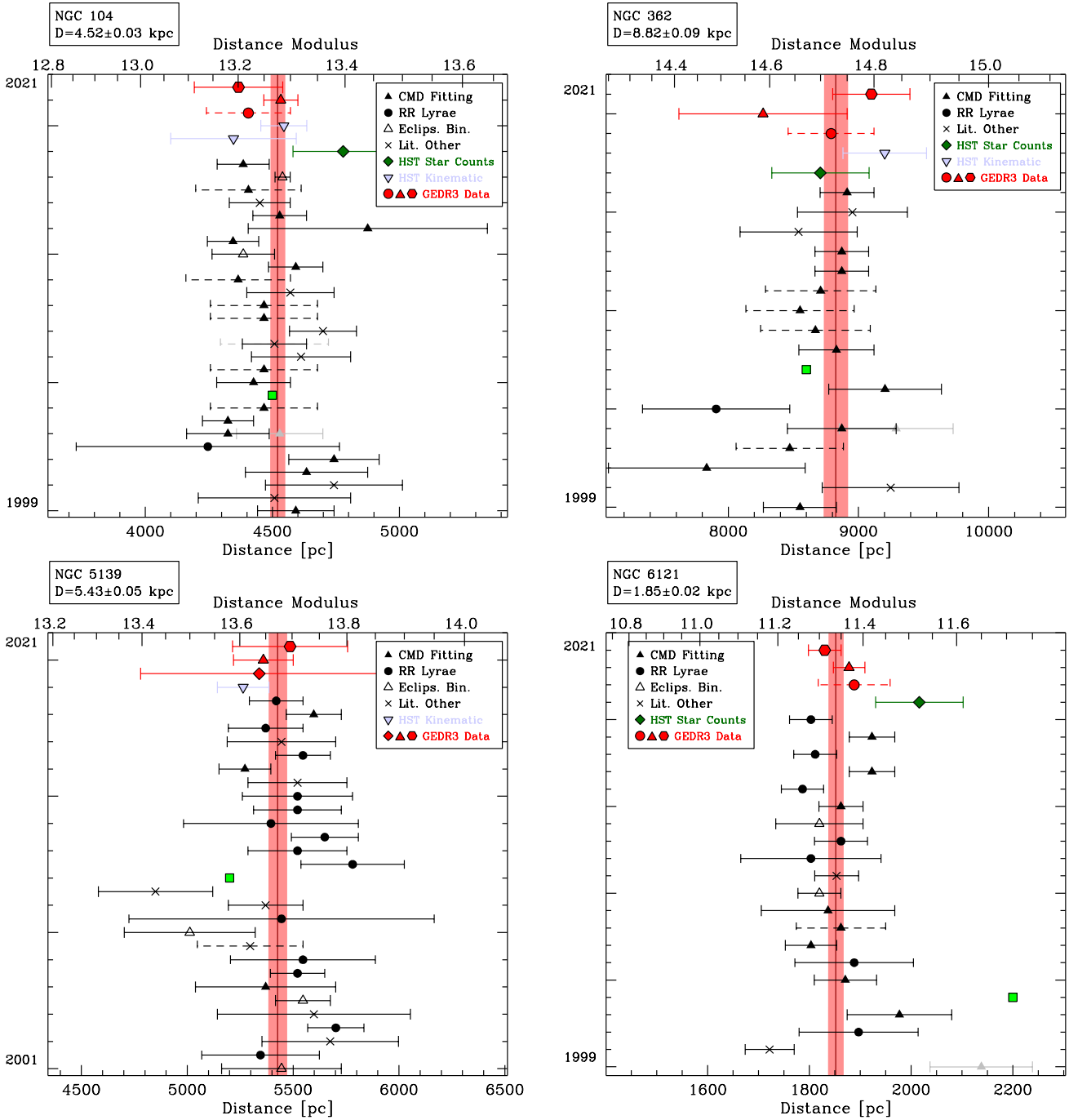
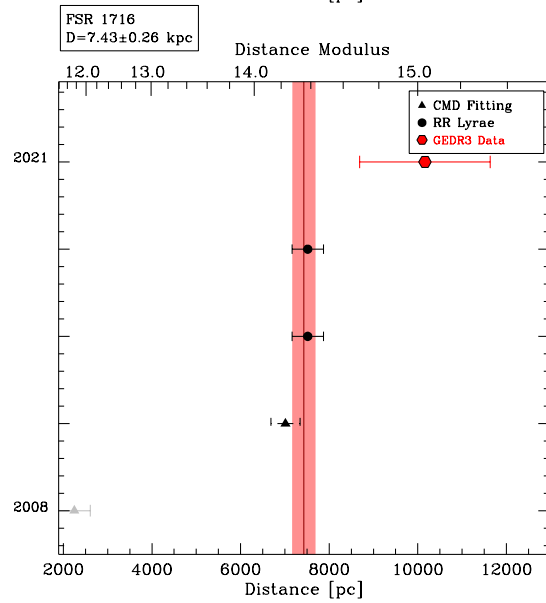
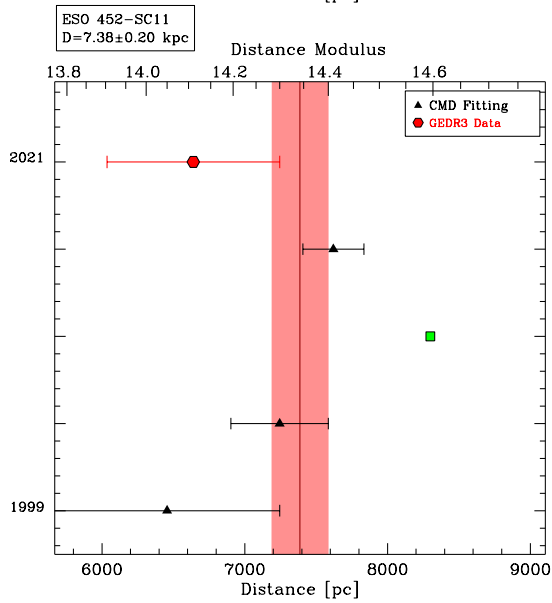
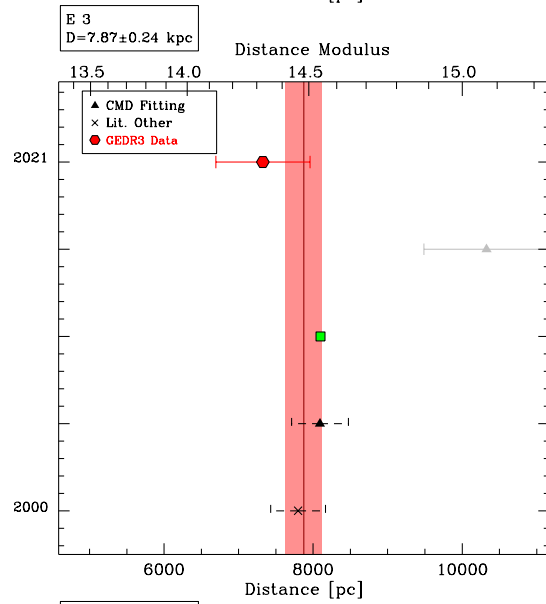
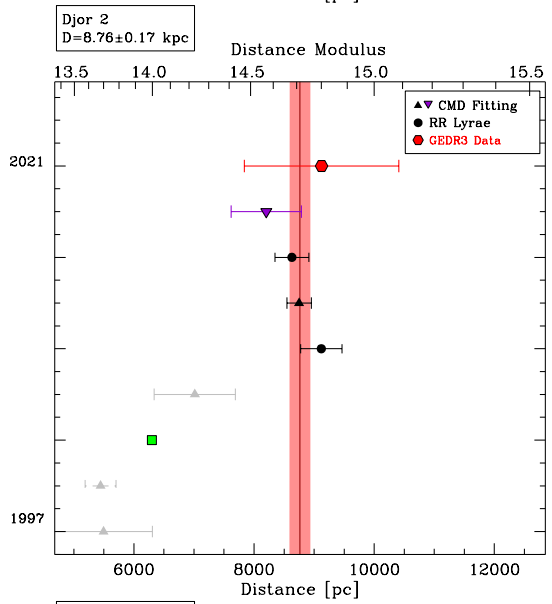
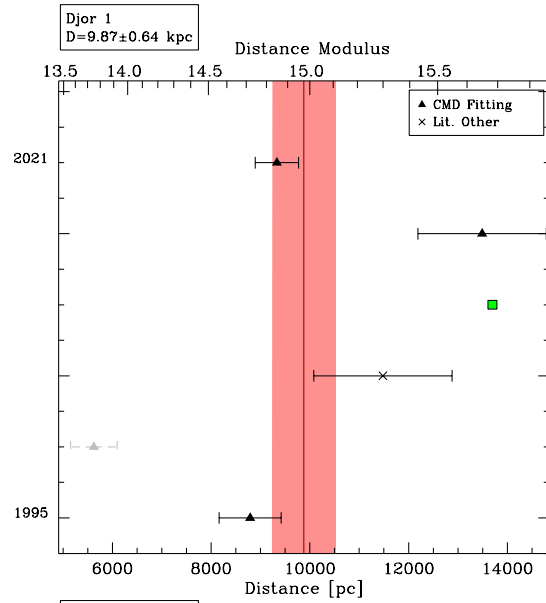
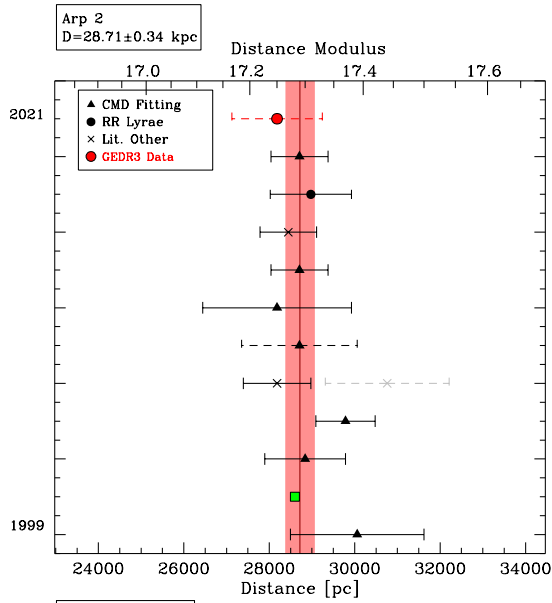


Figure 8. Comparison of recent literature distance determinations for the globular clusters NGC 104, NGC 362, NGC 5139 and NGC 6121 with our data. Black symbols depict distance determinations taken from the literature, while red symbols show our own measurements based on *Gaia* EDR3 data. Red triangles show *Gaia* EDR3 kinematic distances, red circles subdwarf distances, red squares moving group distances and red hexagons show *Gaia* EDR3 parallax distances. Blue triangles show HST kinematic distances and dark green squares with error bars star count distances. The bright green square is the distance given by Harris (2010) based on an averaging of literature values up to 2010. The distances are sorted according to publication year, with newest measurements at the top of each panel and the first and last year indicated. Distance determinations shown in grey have been neglected when calculating the mean cluster distance. For literature distances without an error, the dashed error bars show our adopted error. Solid error bars are literature measurements with error bars. The red vertical line and shaded region marks the average distance and its 1σ error bar. The average distances are also given at the top of each panel.



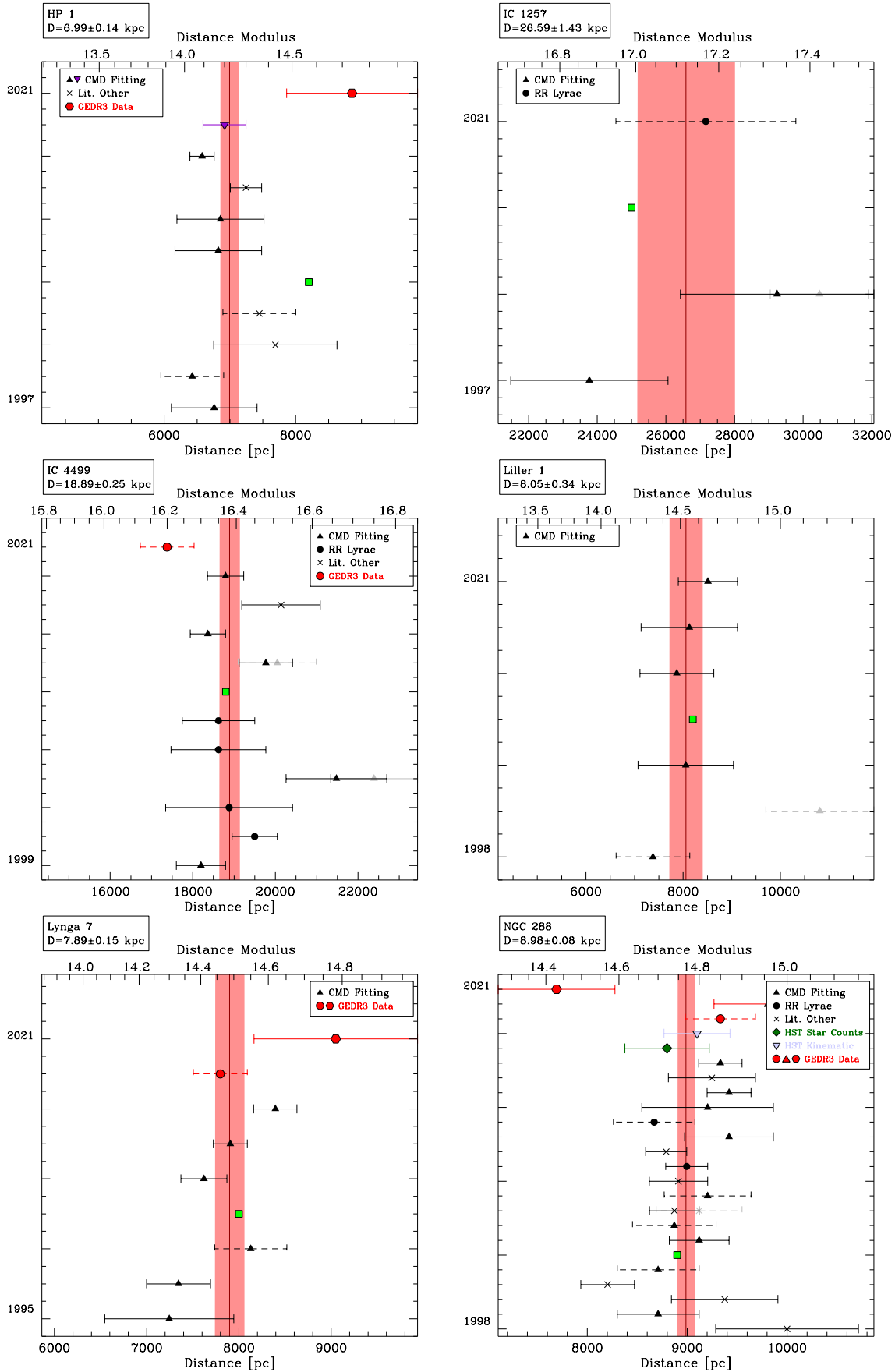


Figure 10. Same as Fig. 8 for HP 1, IC 1257, IC 4499 and Liller 1, Lynga 7 and NGC 288.

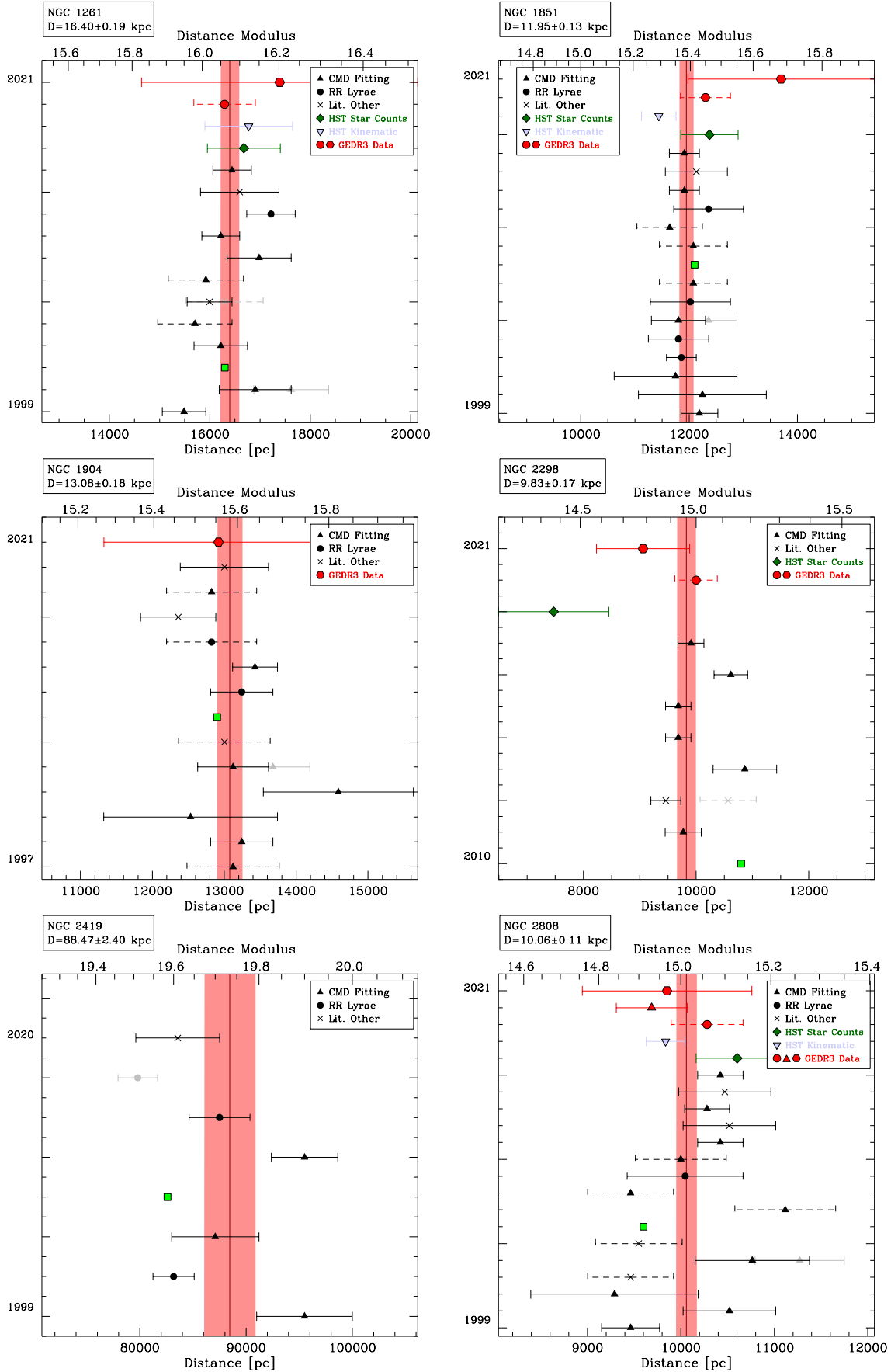


Figure 11. Same as Fig. 8 for NGC 1261, NGC 1851, NGC 1904, NGC 2298, NGC 2419 and NGC 2808.

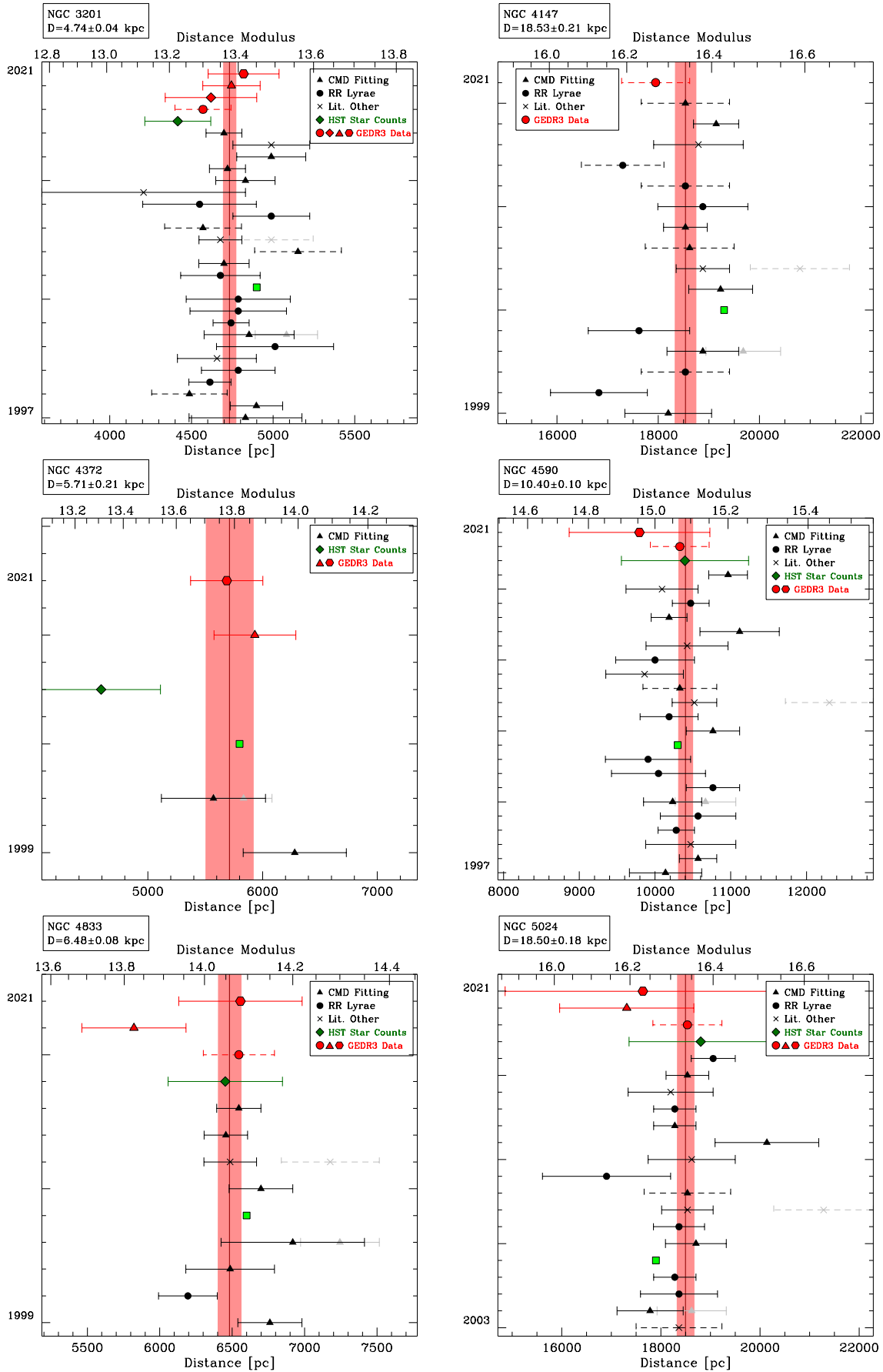
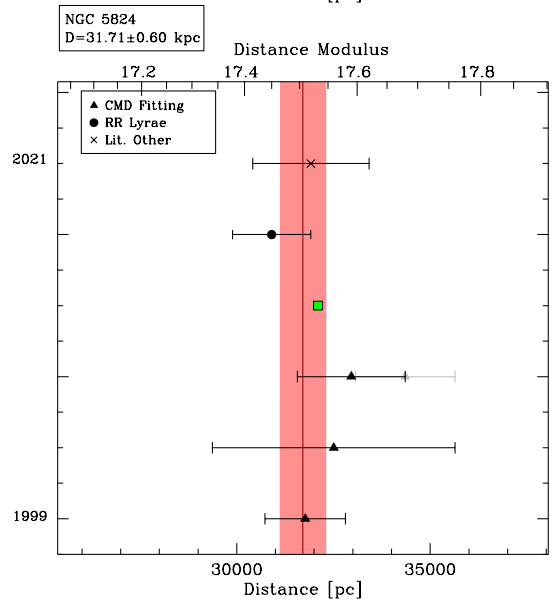
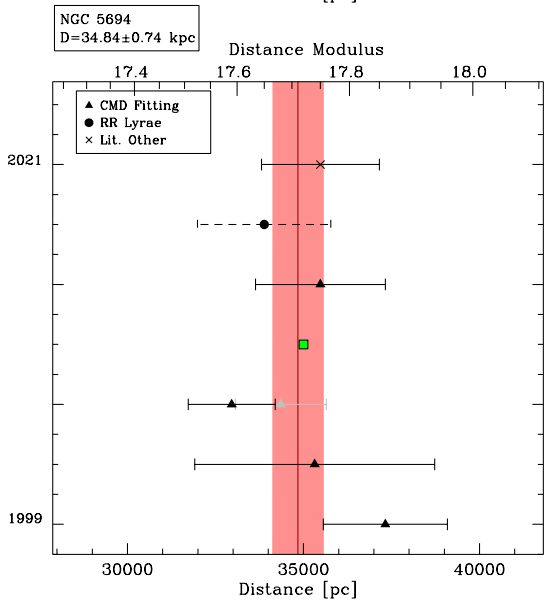
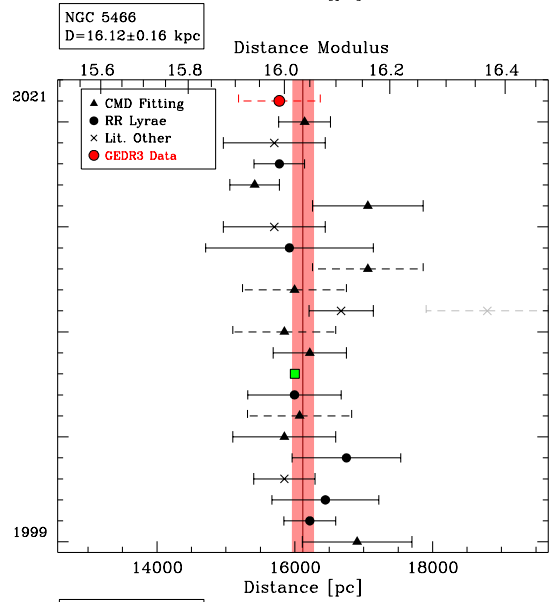
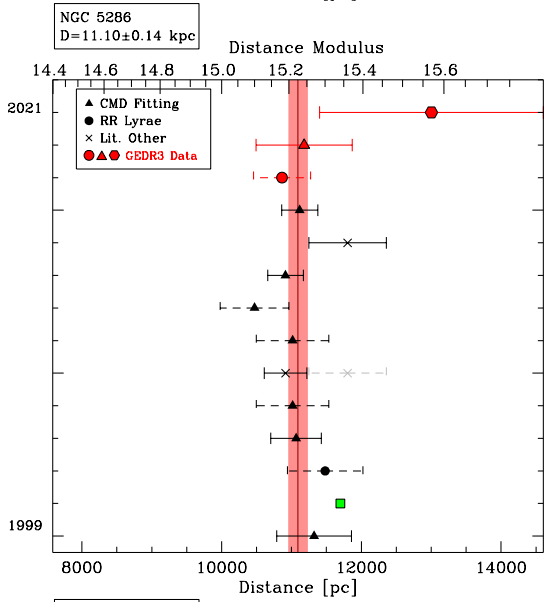
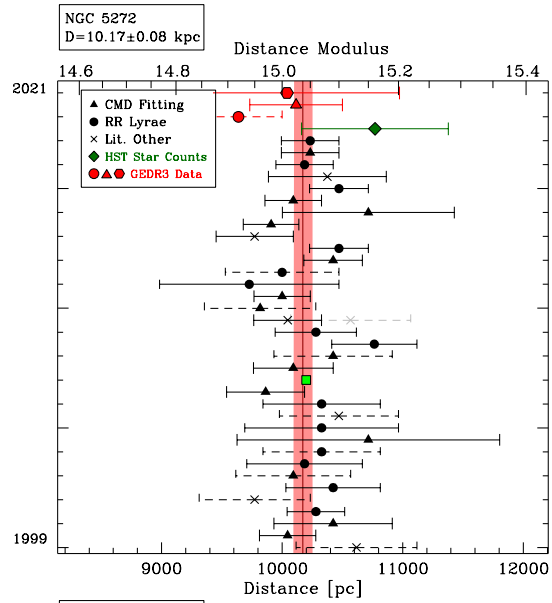
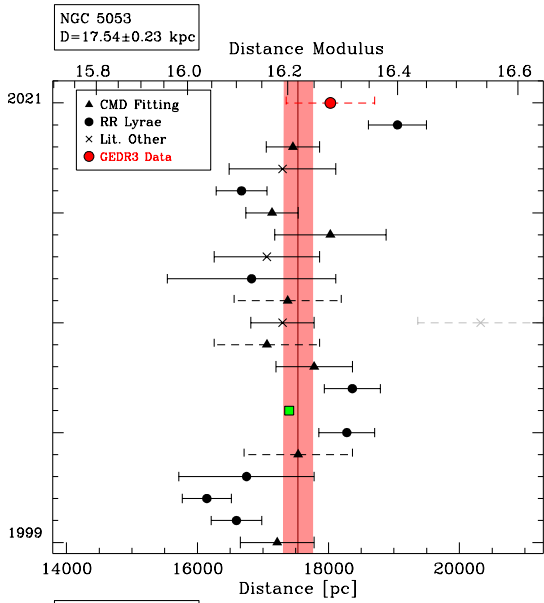


Figure 12. Same as Fig. 8 for NGC 3201, NGC 4147, NGC 4372, NGC 4590, NGC 4833 and NGC 5024.



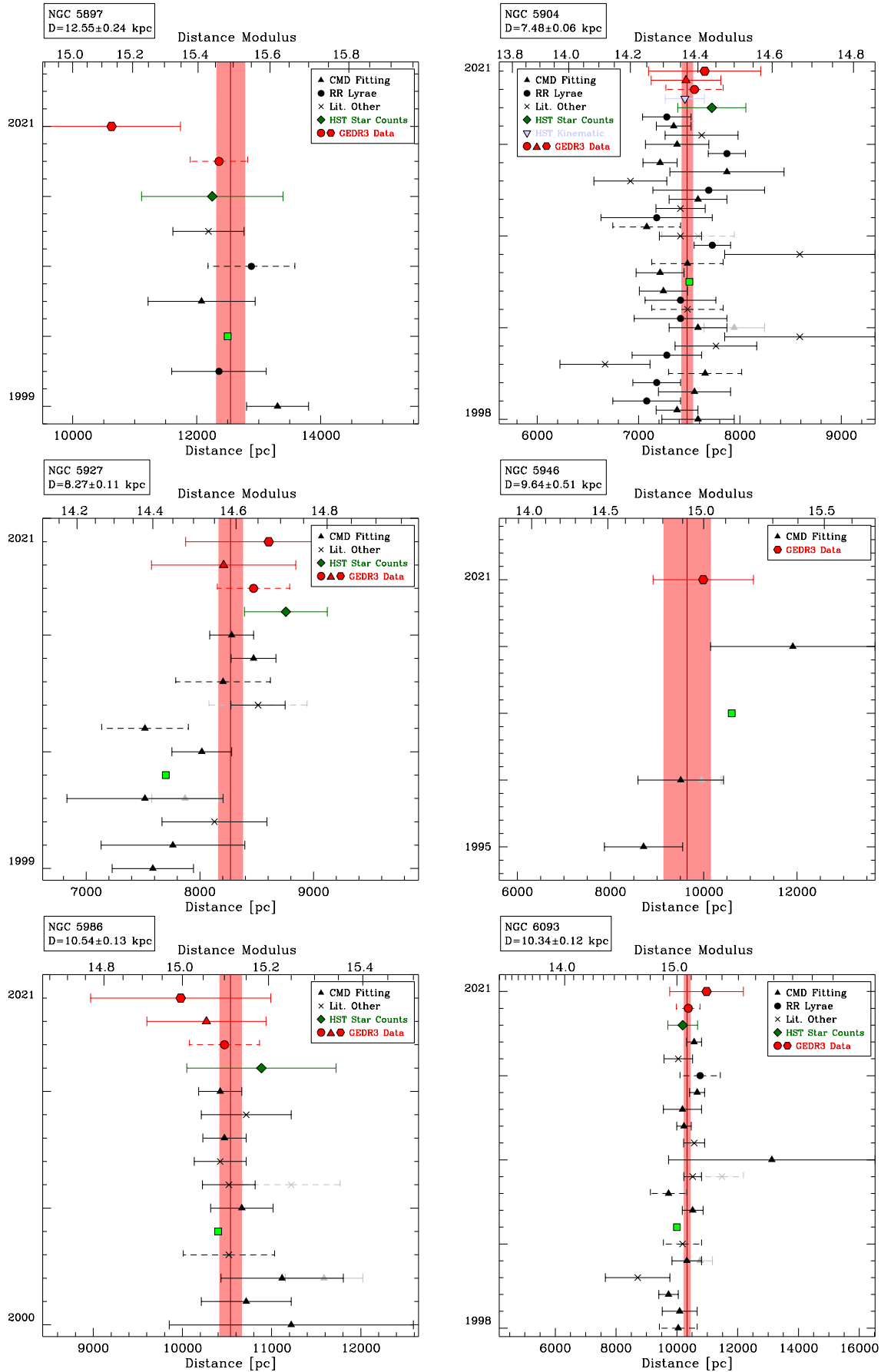
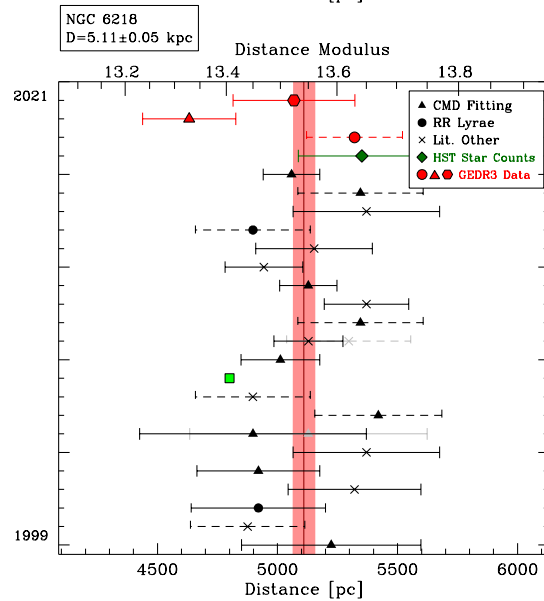
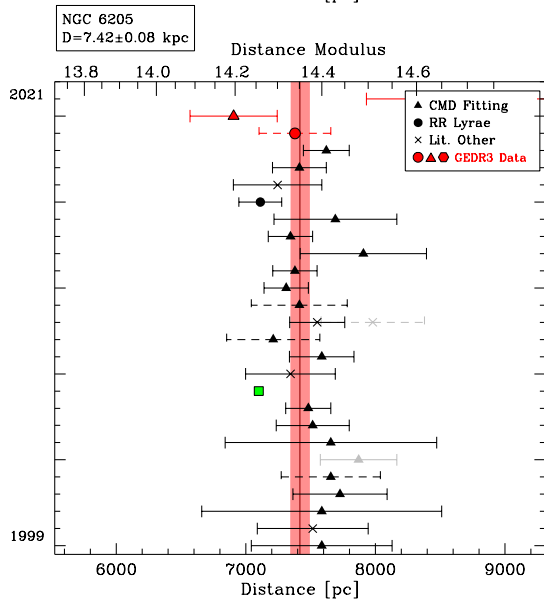
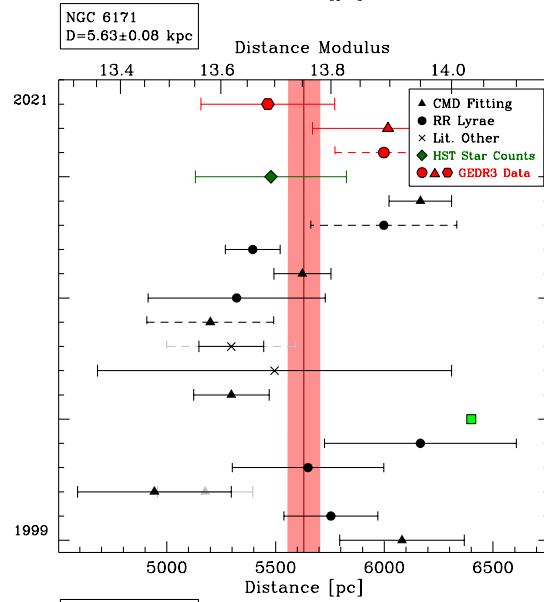
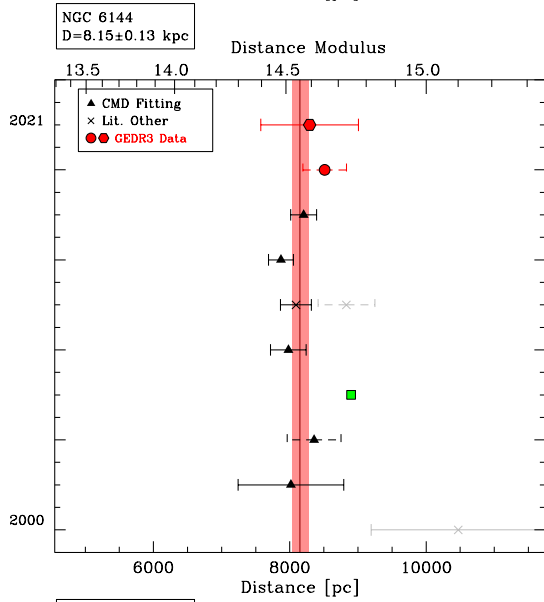
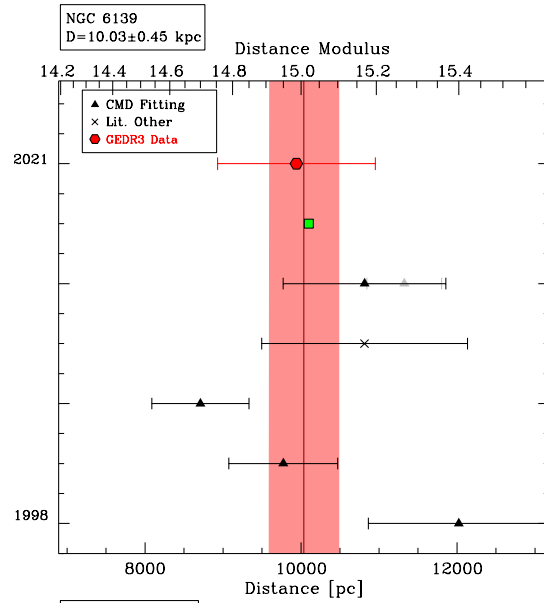
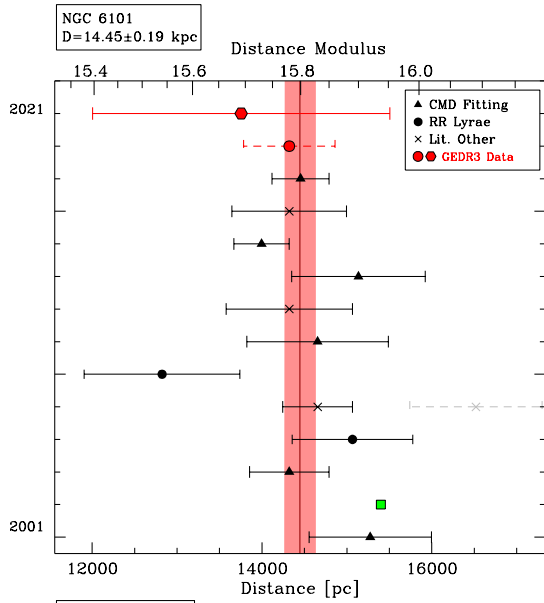
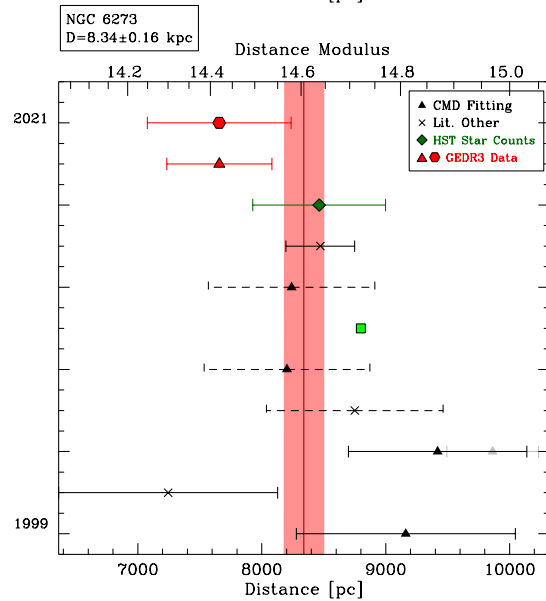
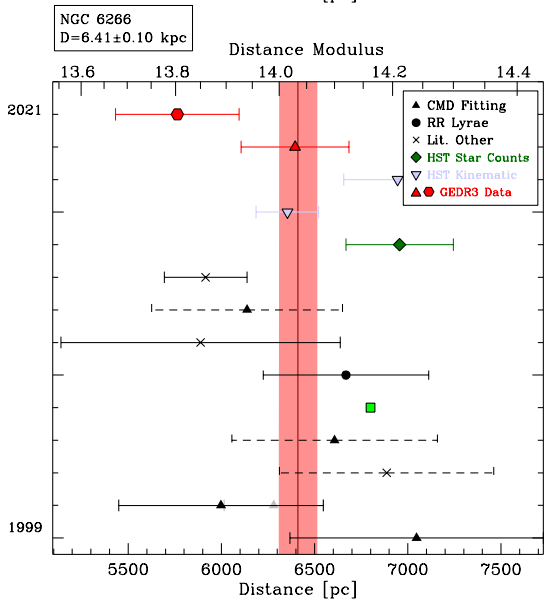
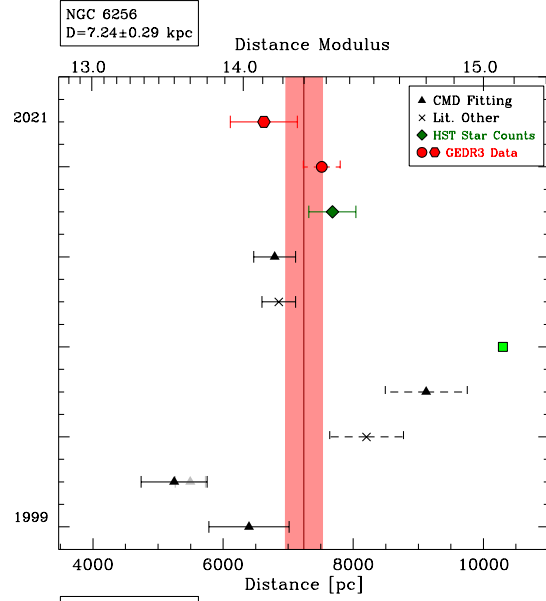
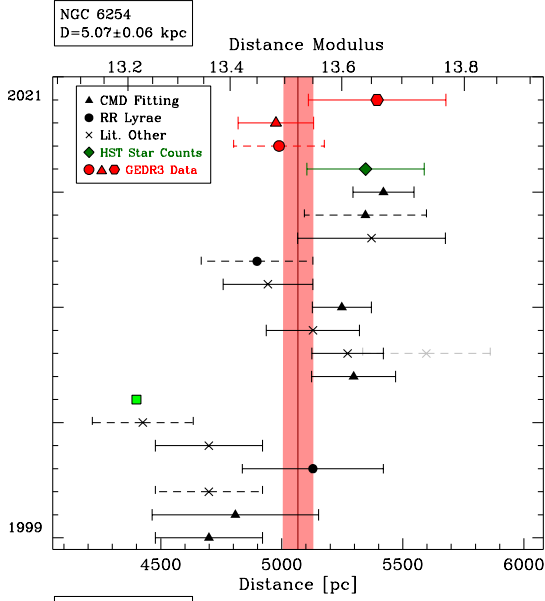
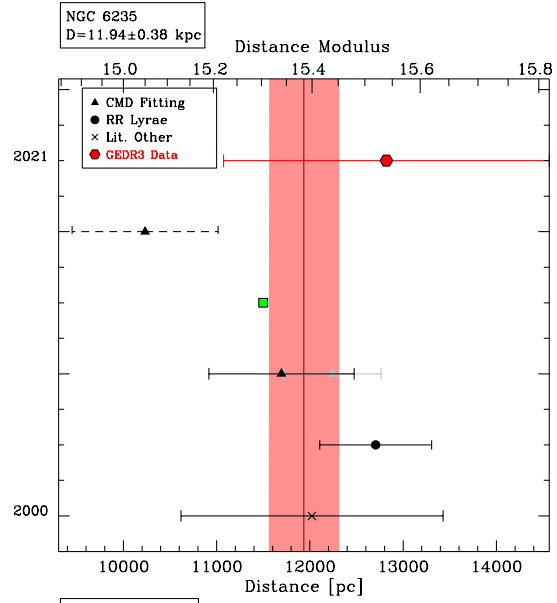
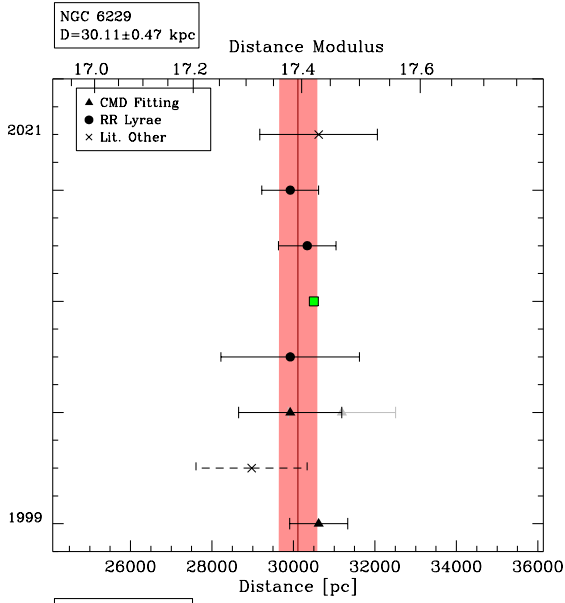
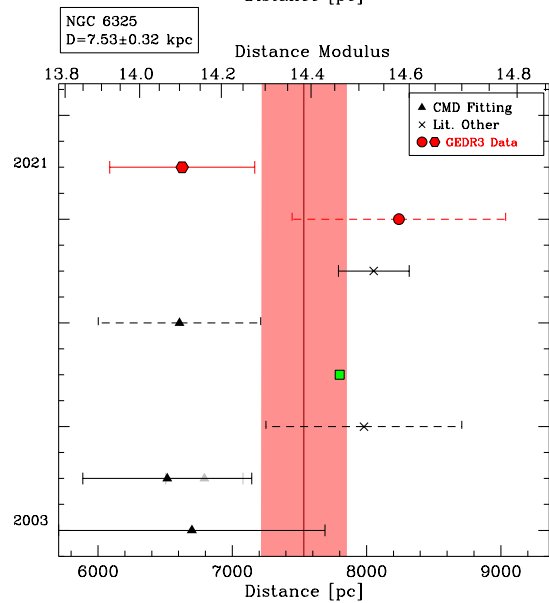
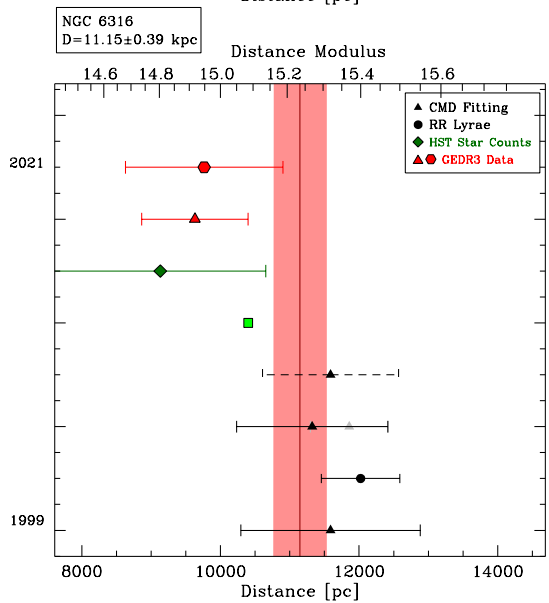
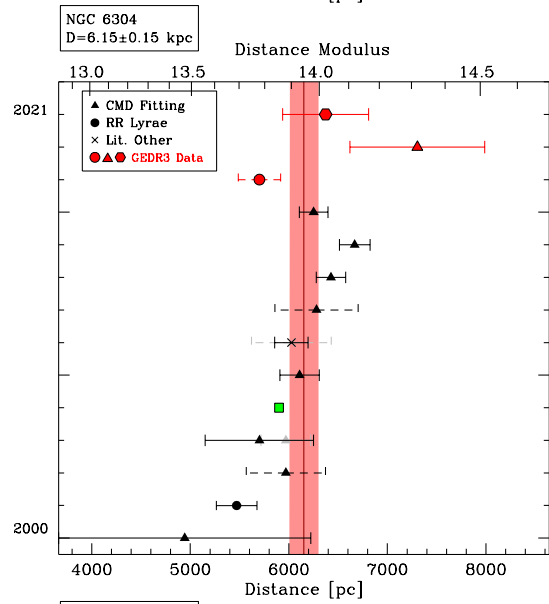
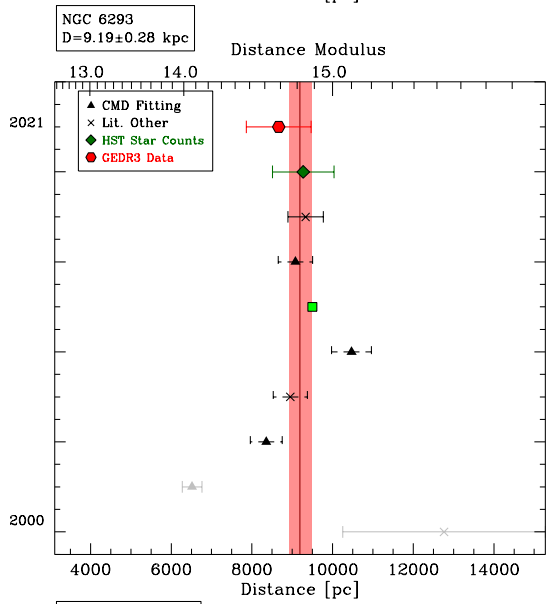
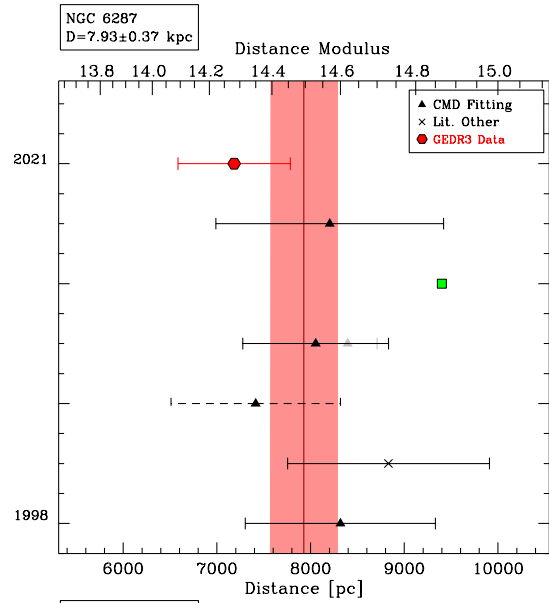
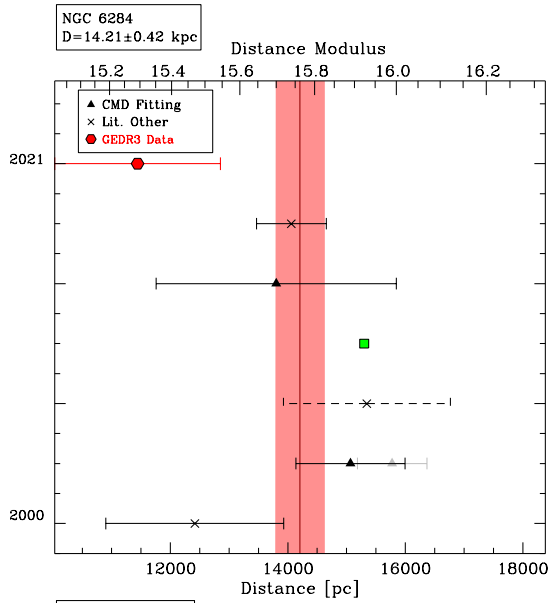


FIG. 14. Distance modulus plots for NGC 5897, NGC 5904, NGC 5927, NGC 5946, NGC 5986, and NGC 6093.







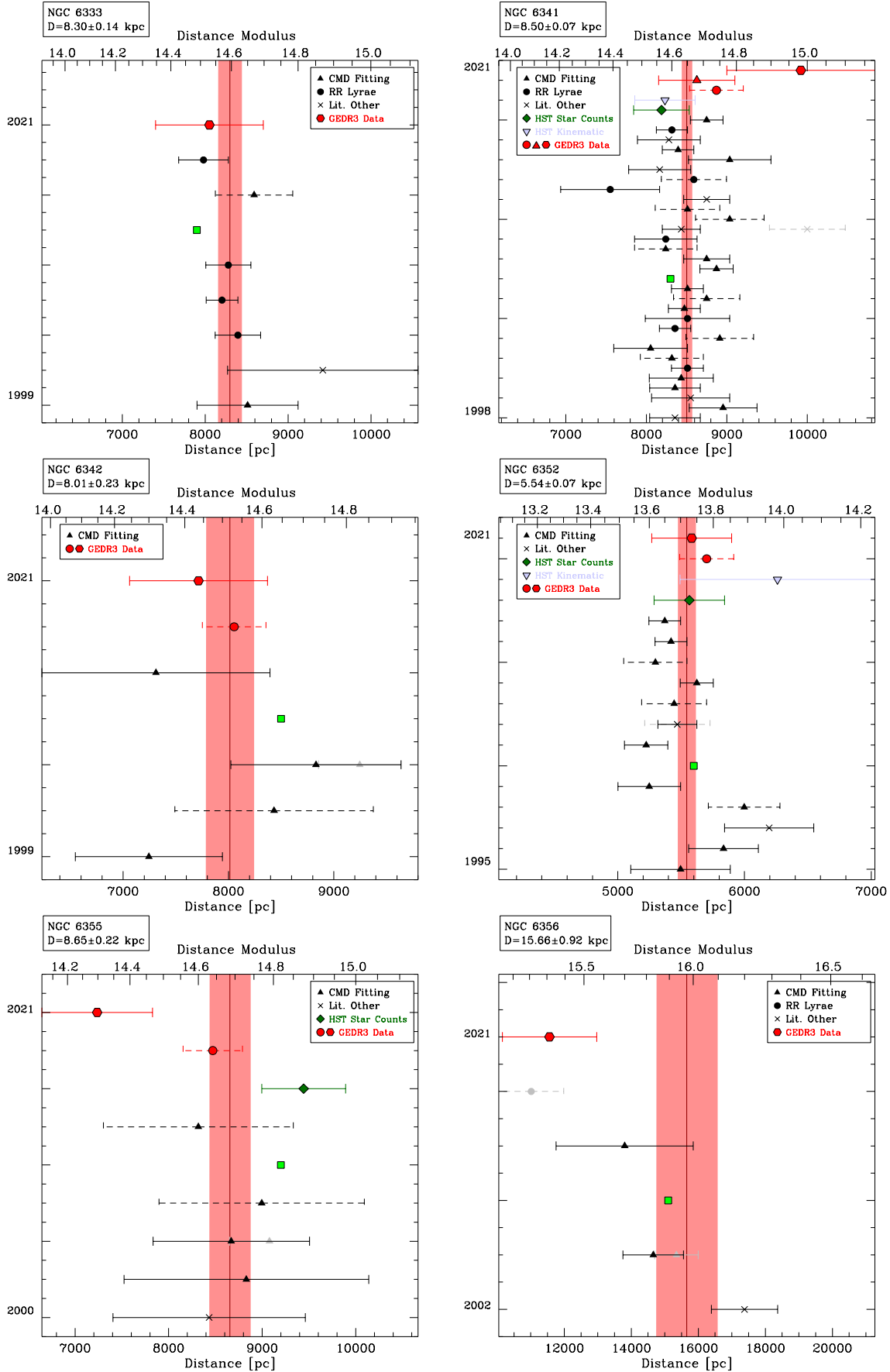
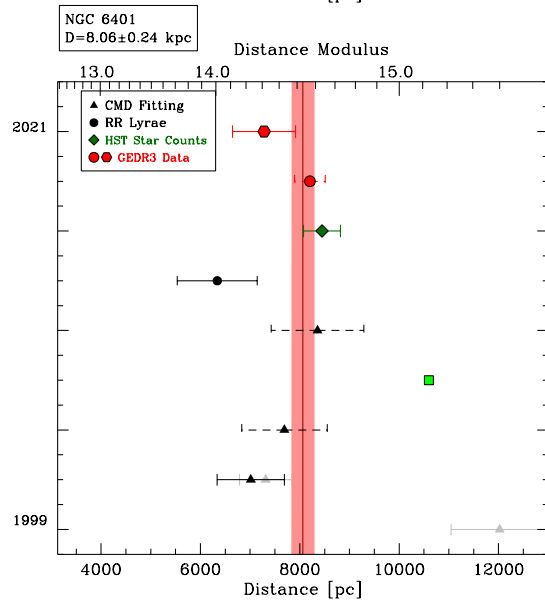
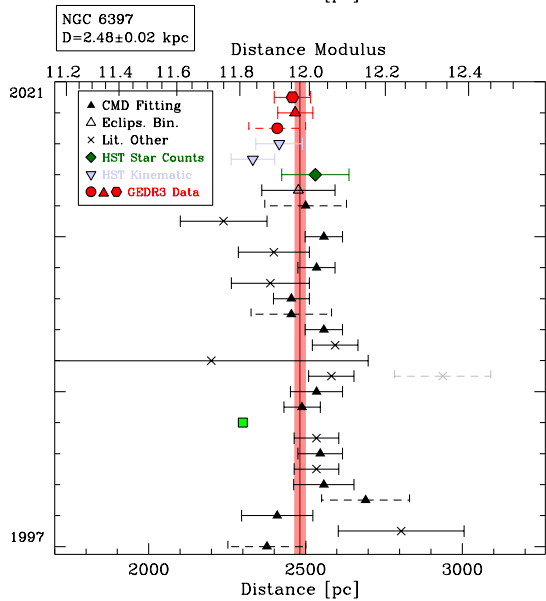
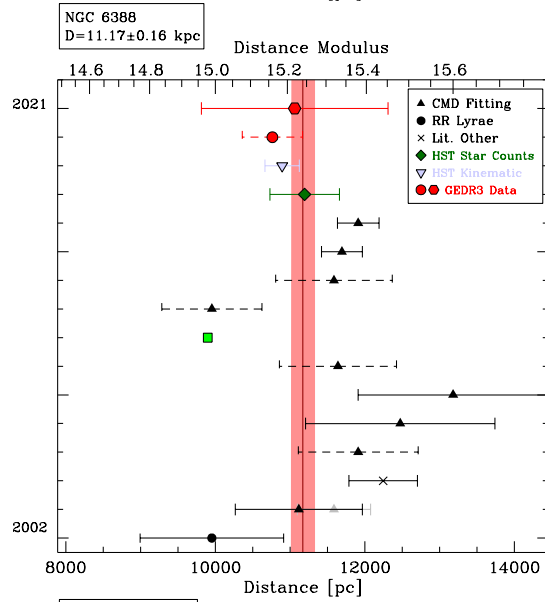
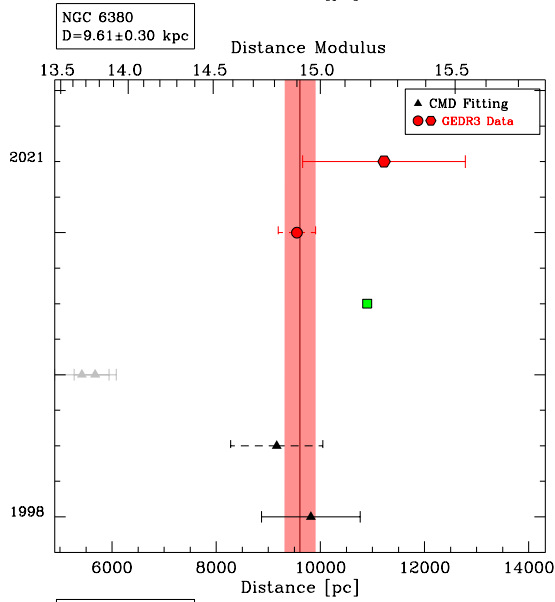
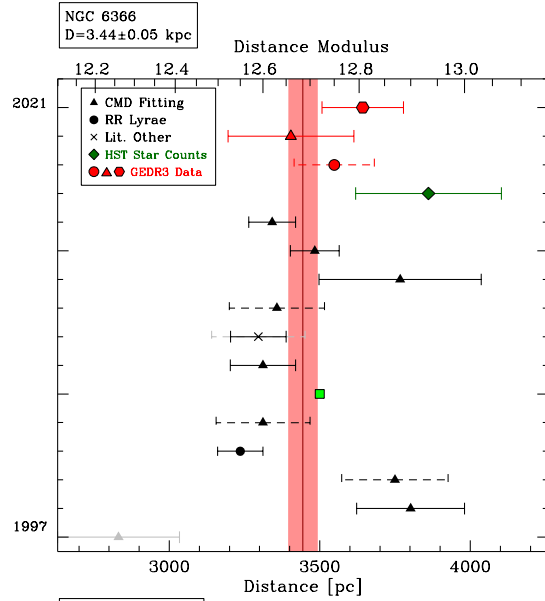
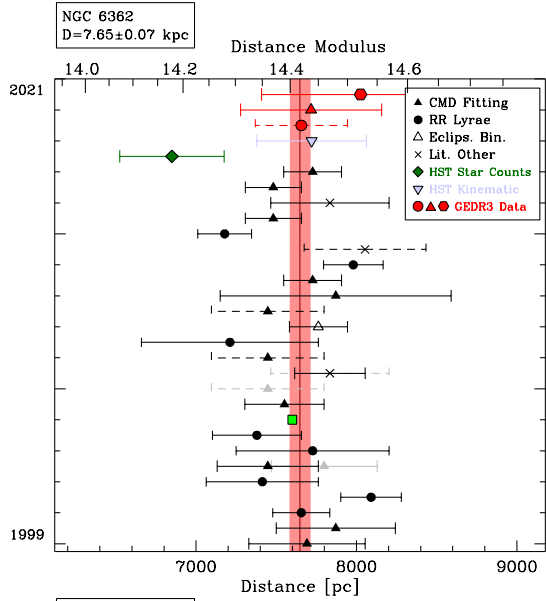


Figure 18. Same as Fig. 8 for NGC 6333, NGC 6341, NGC 6342 and NGC 6352, NGC 6355 and NGC 6356.



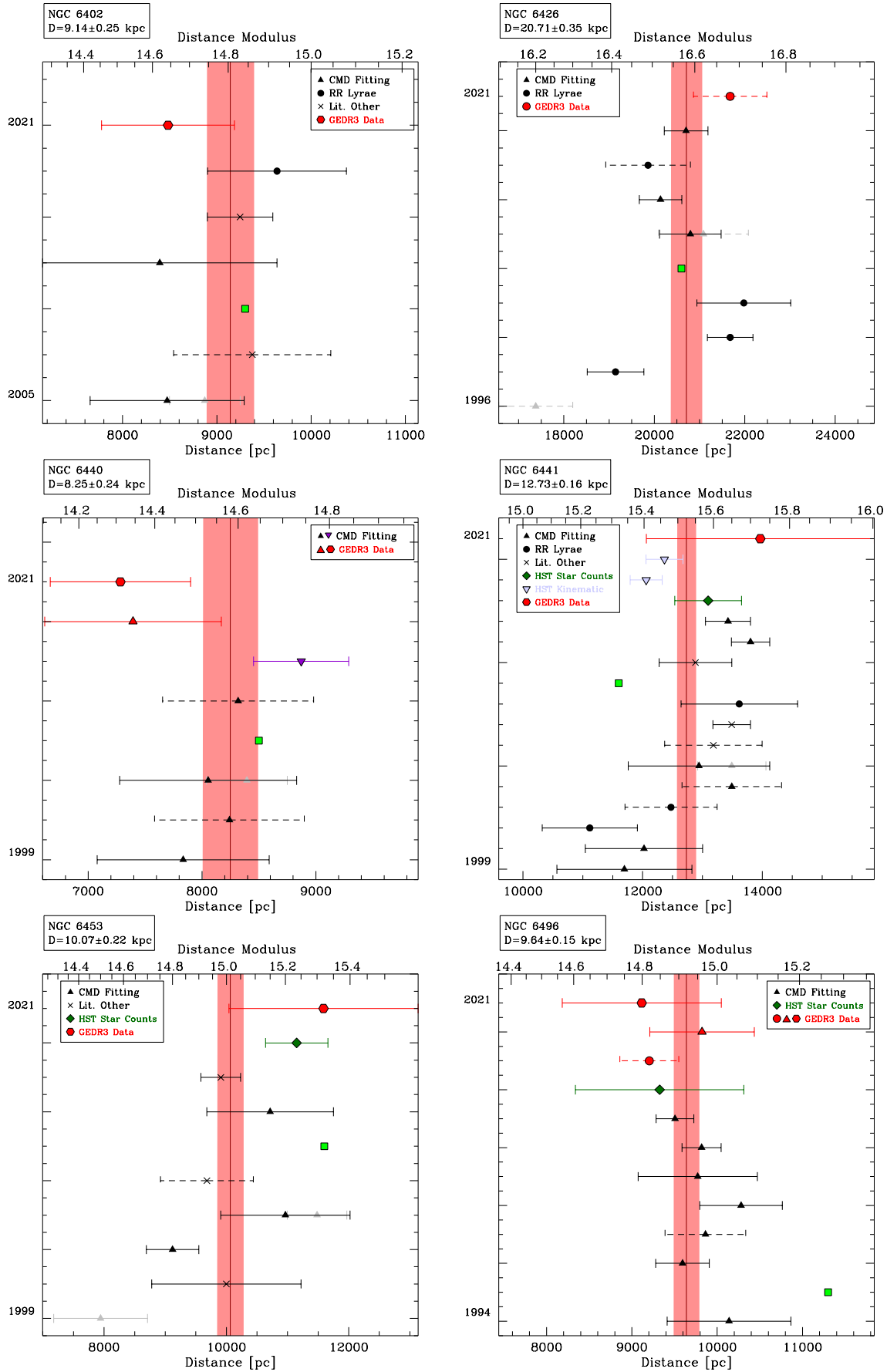
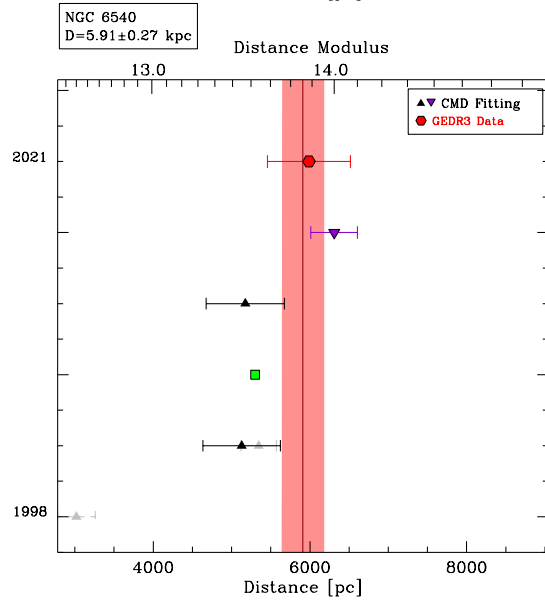
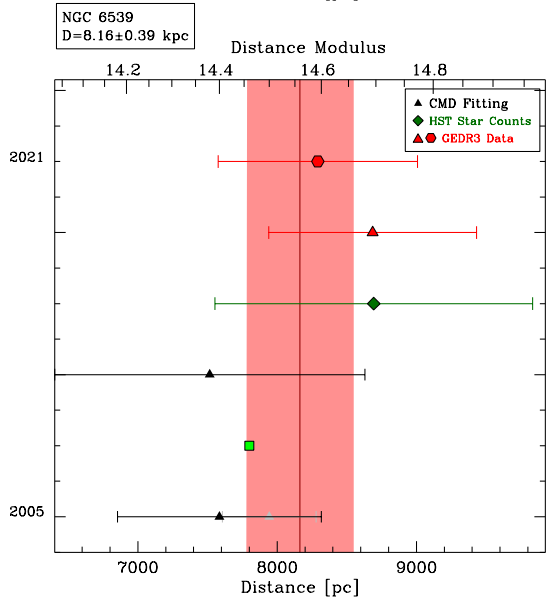
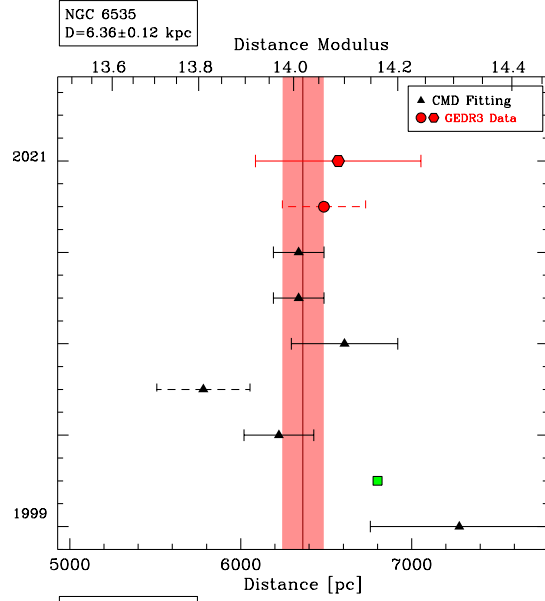
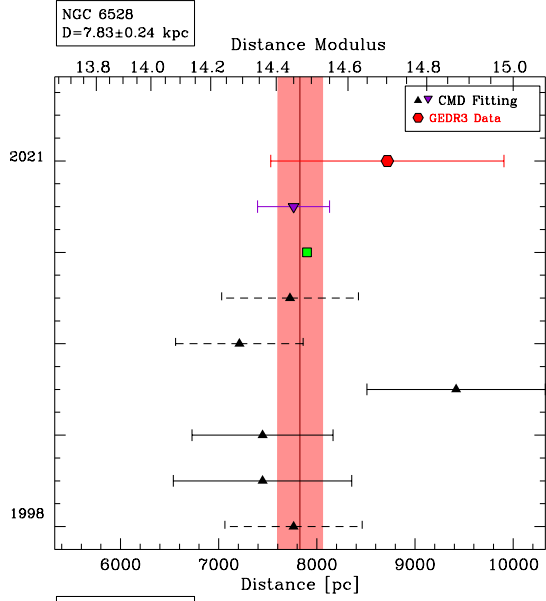
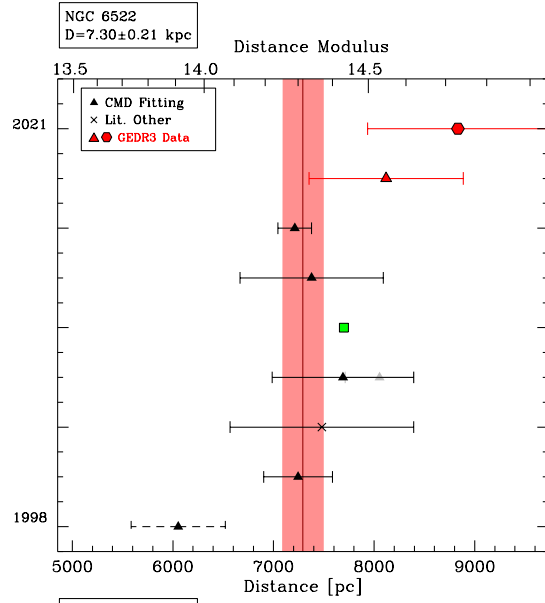
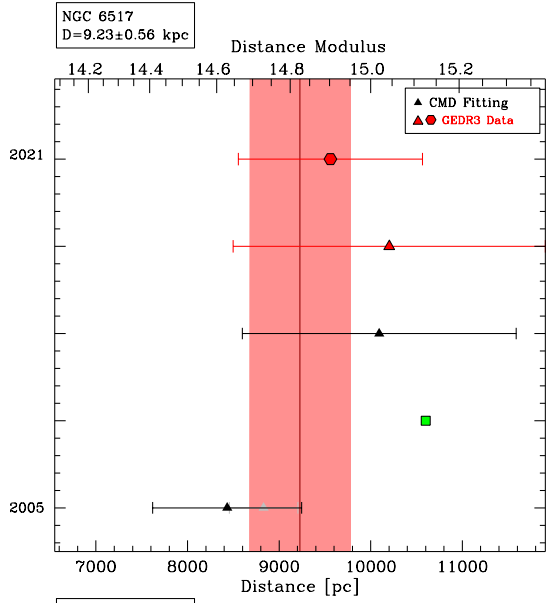
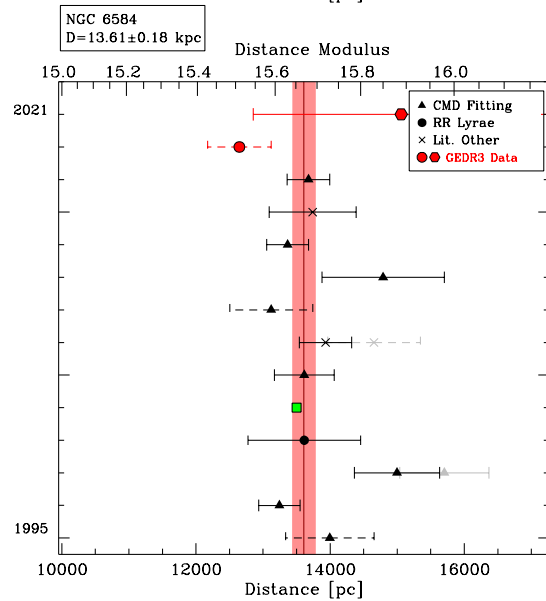
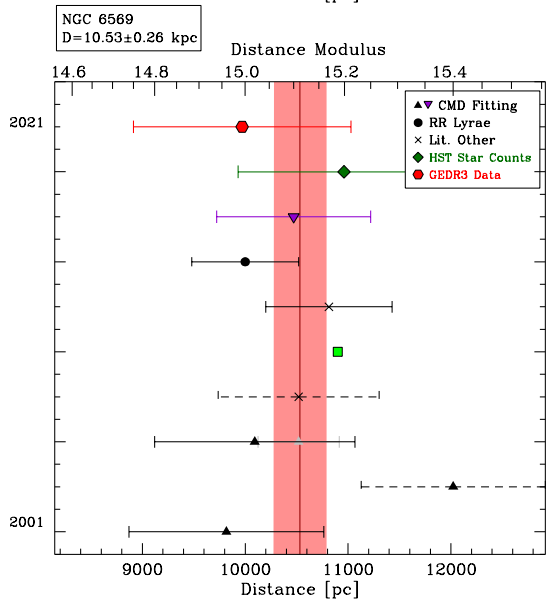
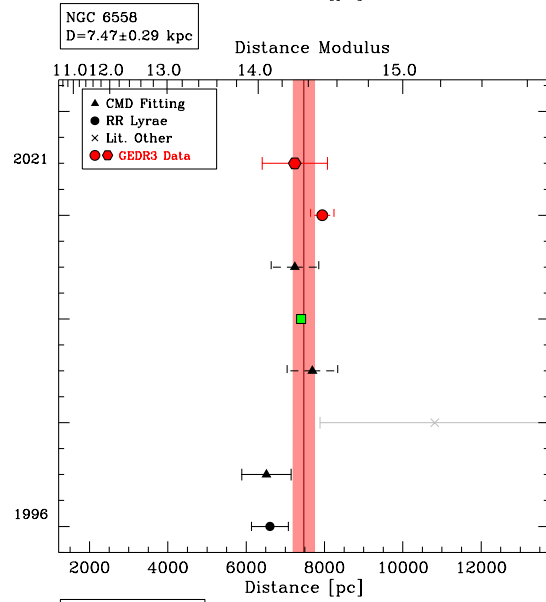
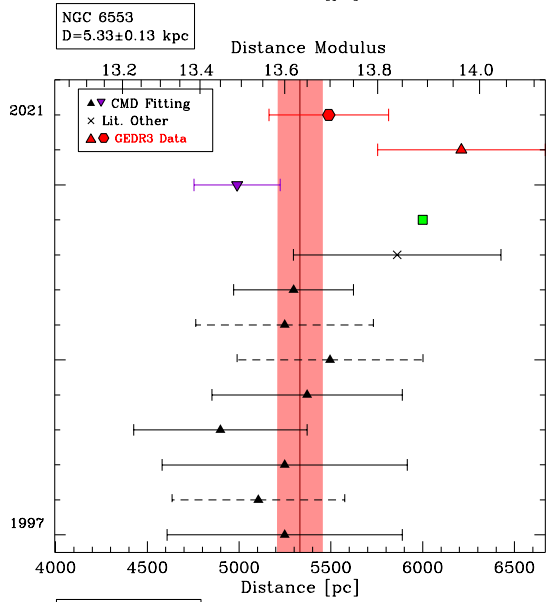
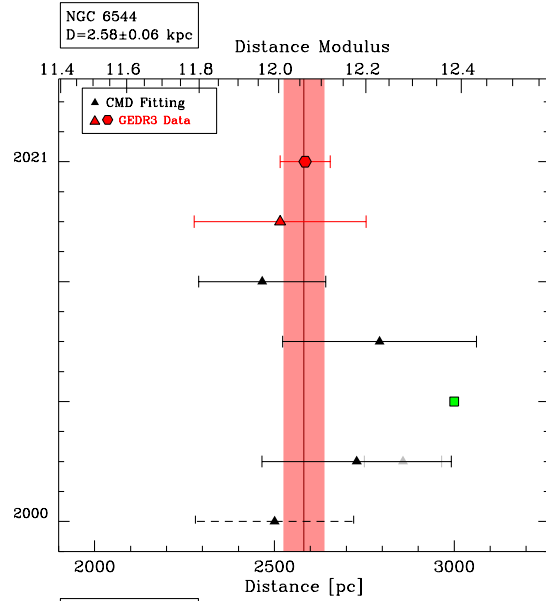
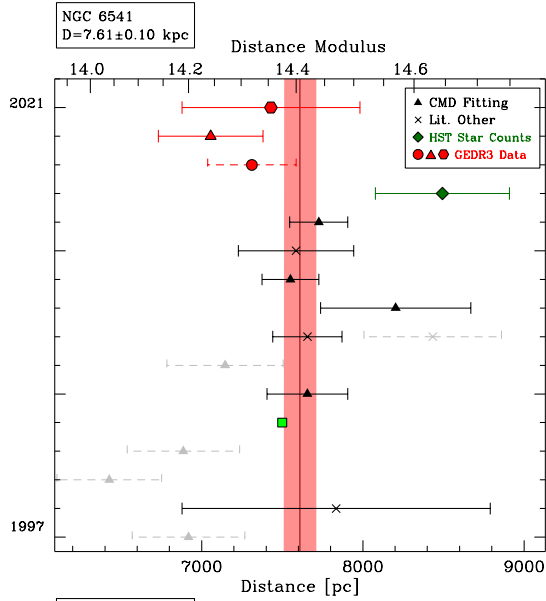
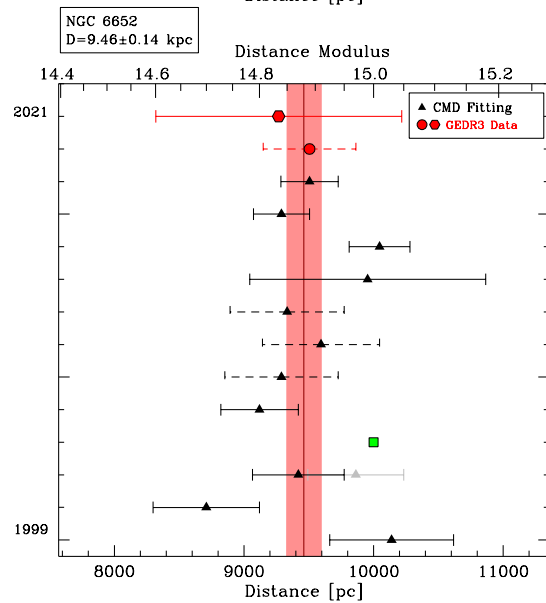
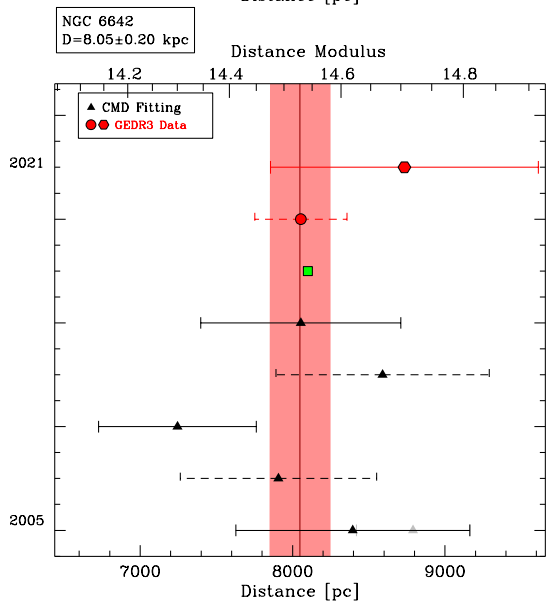
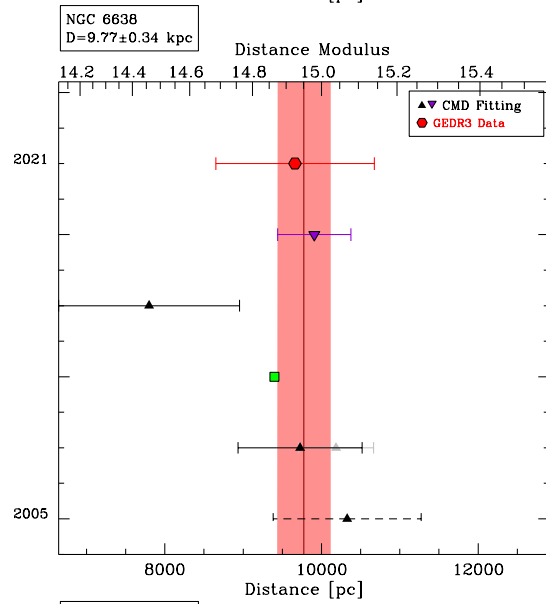
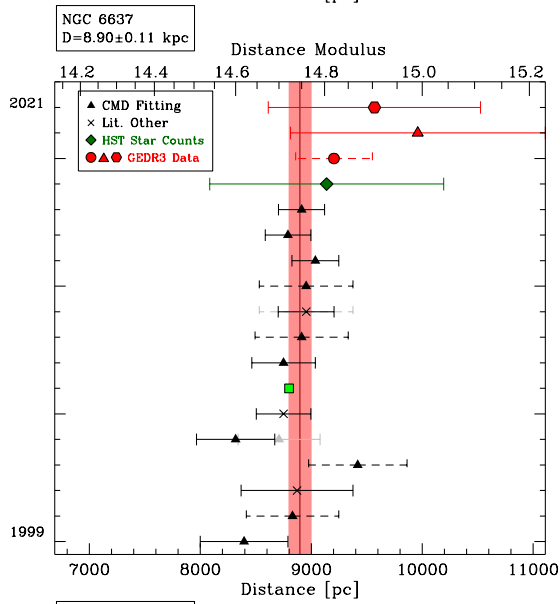
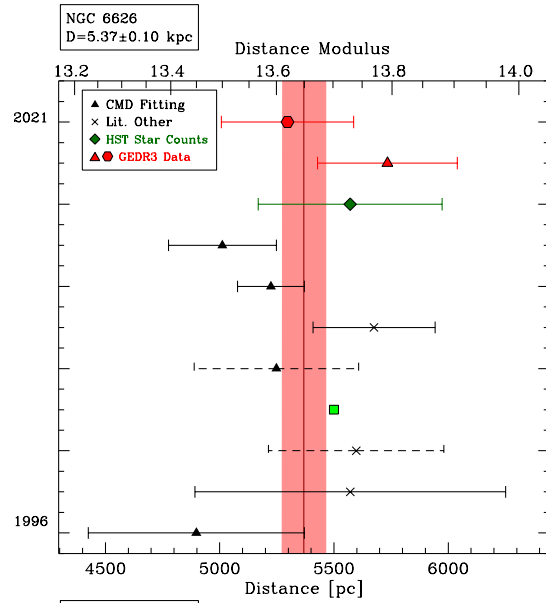
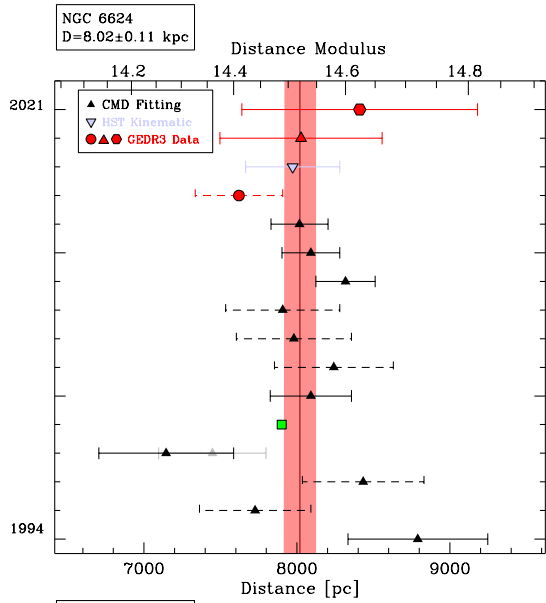
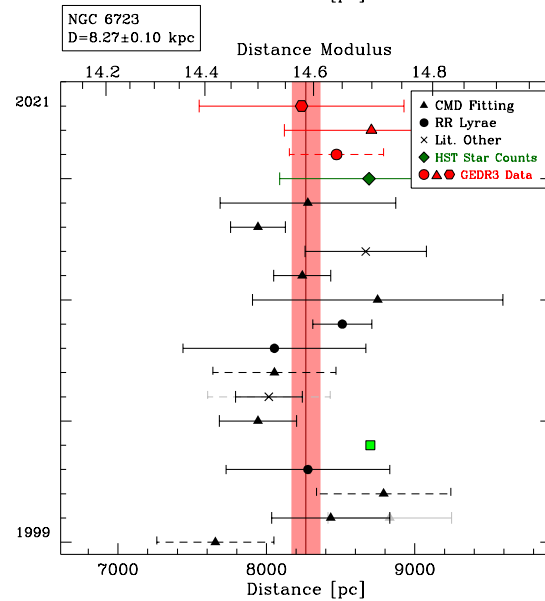
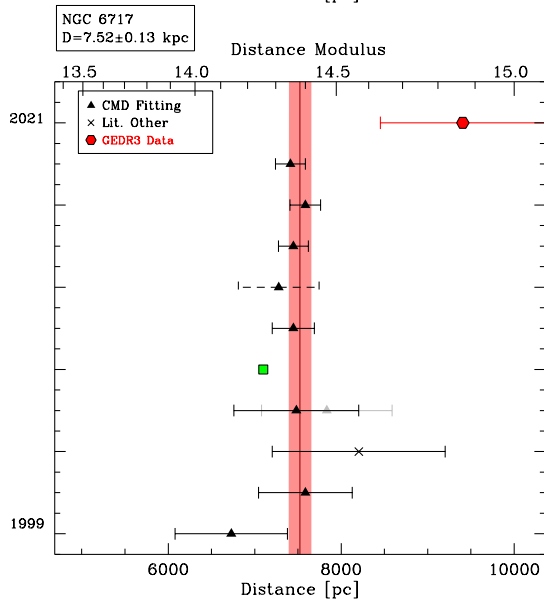
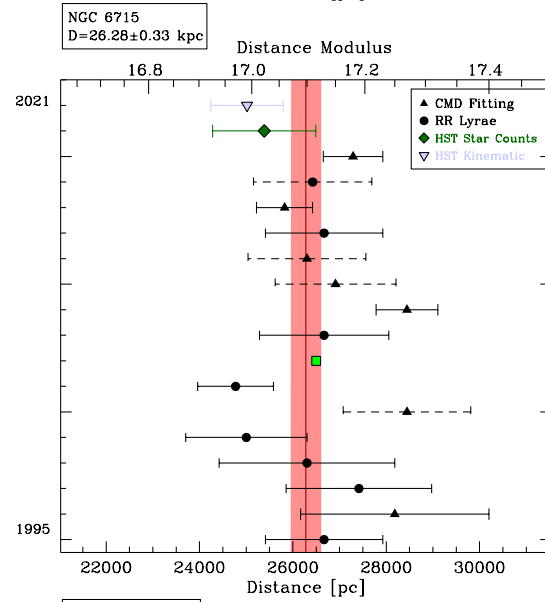
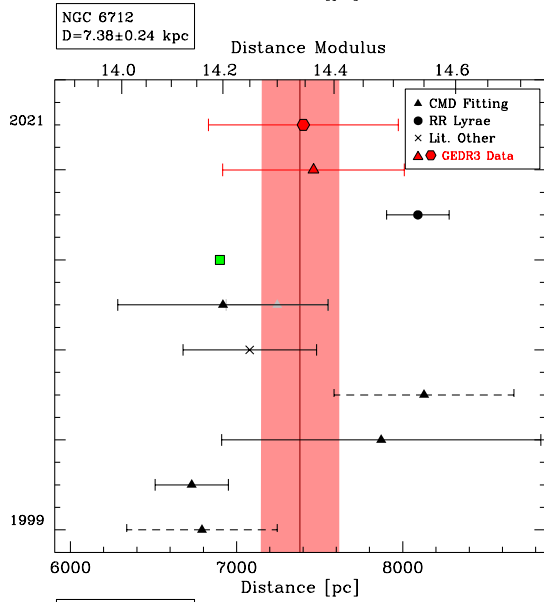
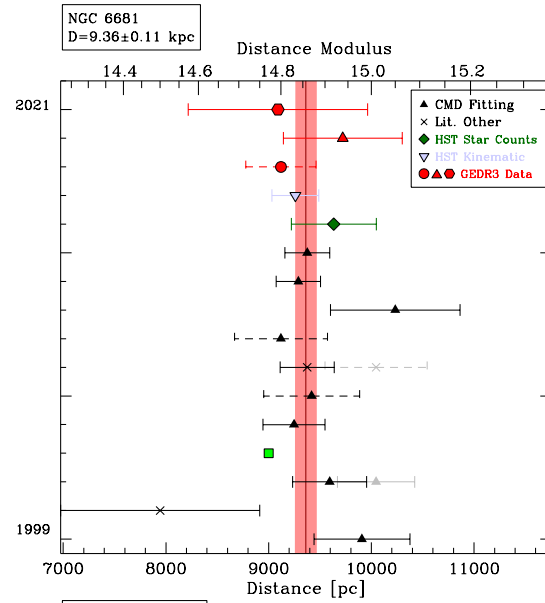
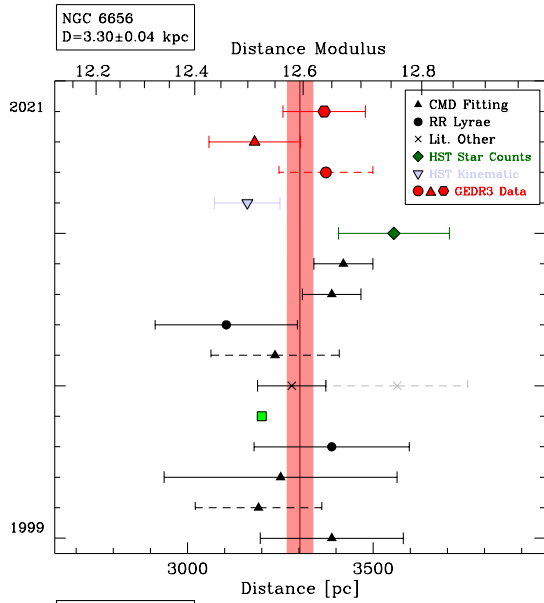


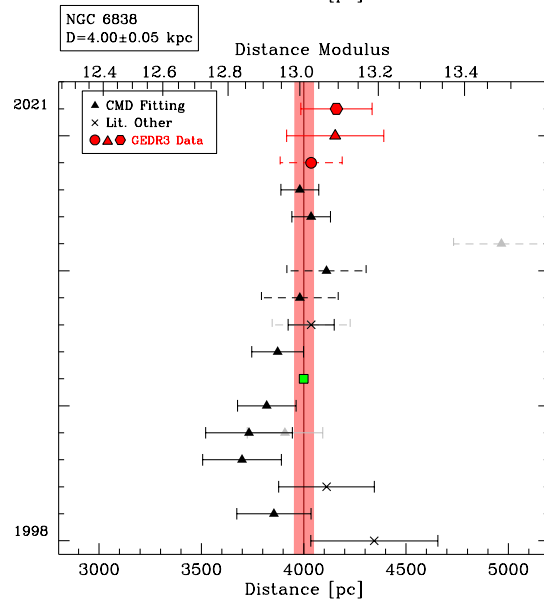
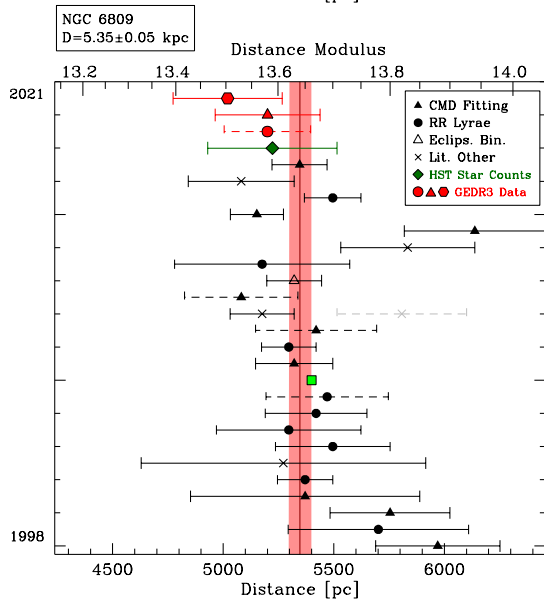
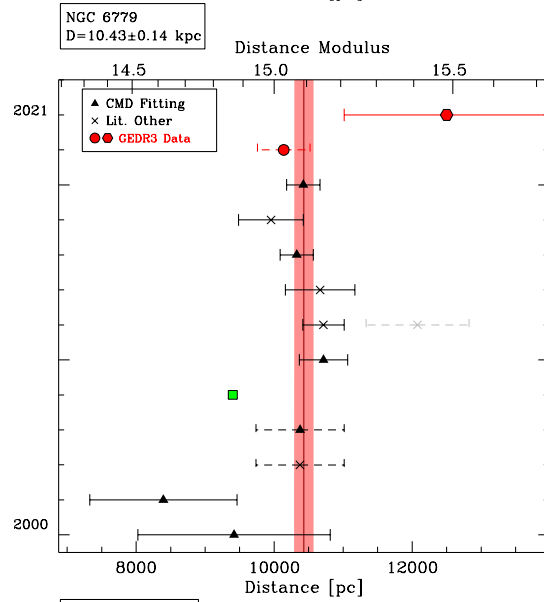
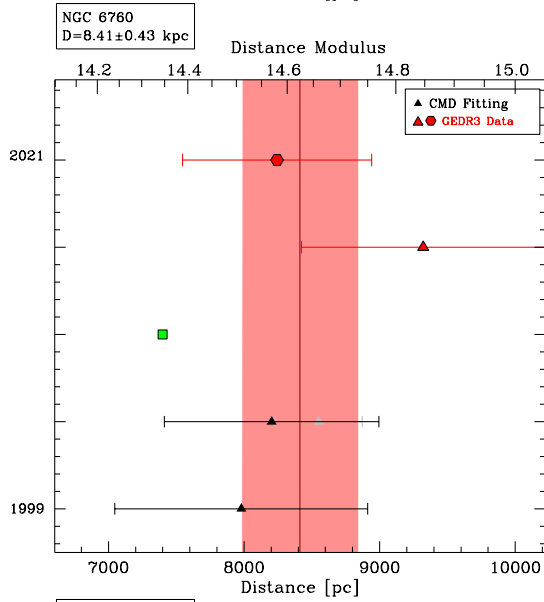
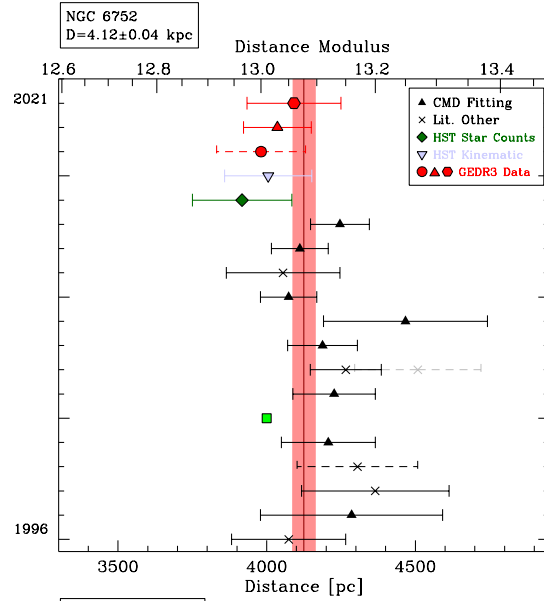
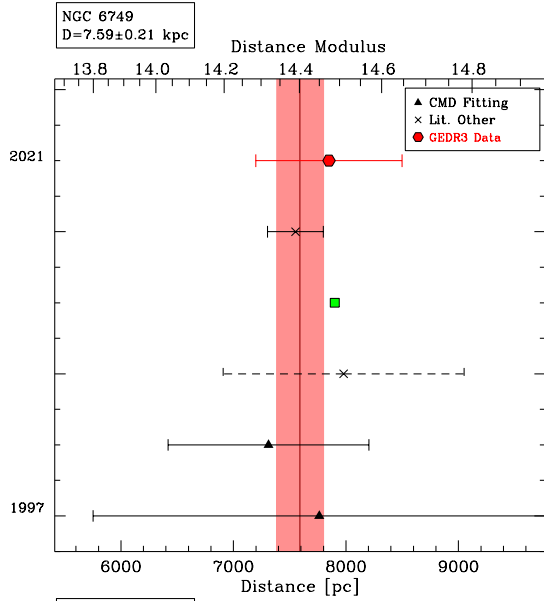
Figure 20. Same as Fig. 8 for NGC 6402, NGC 6426, NGC 6440 and NGC 6441, NGC 6453 and NGC 6496.

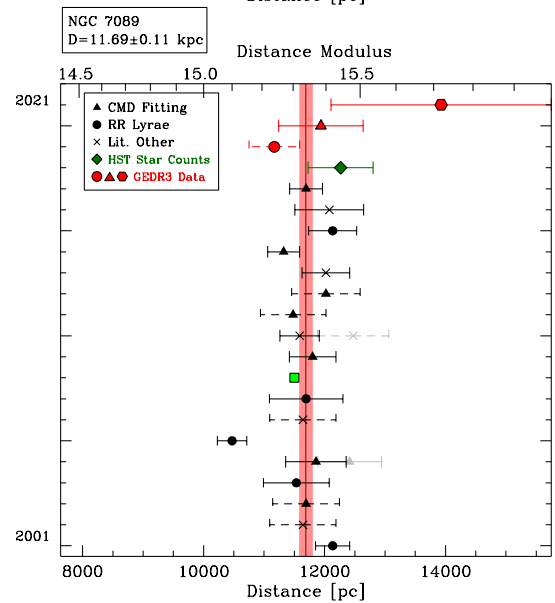
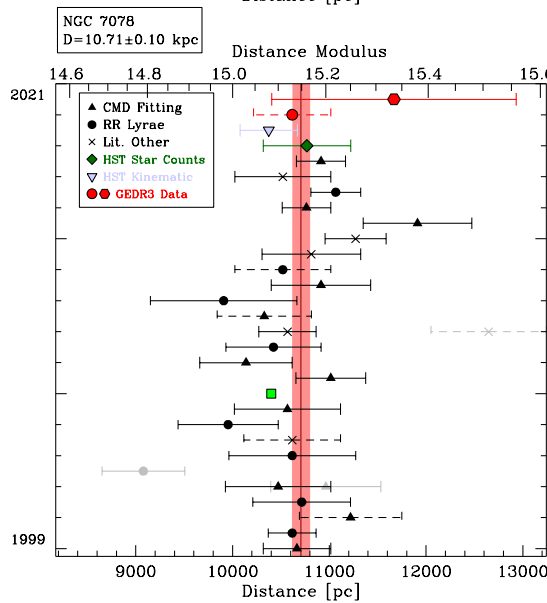
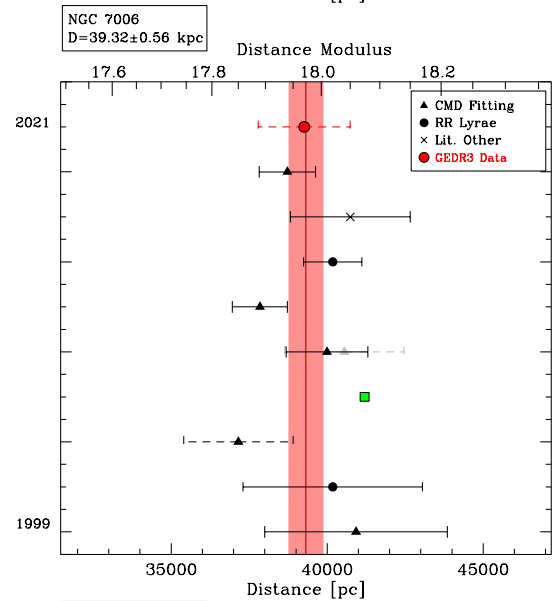
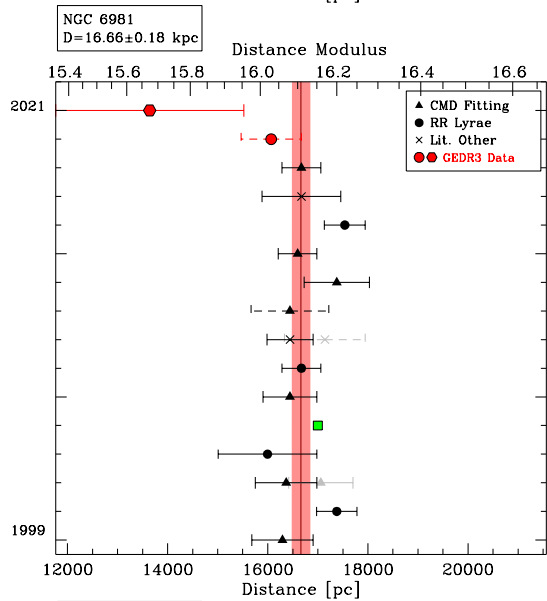
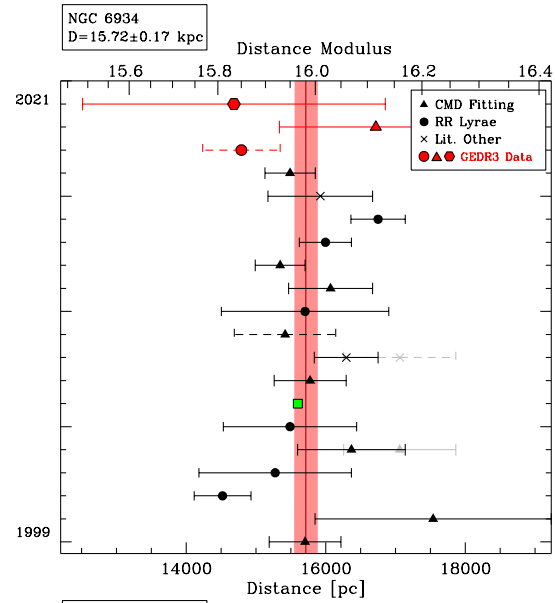
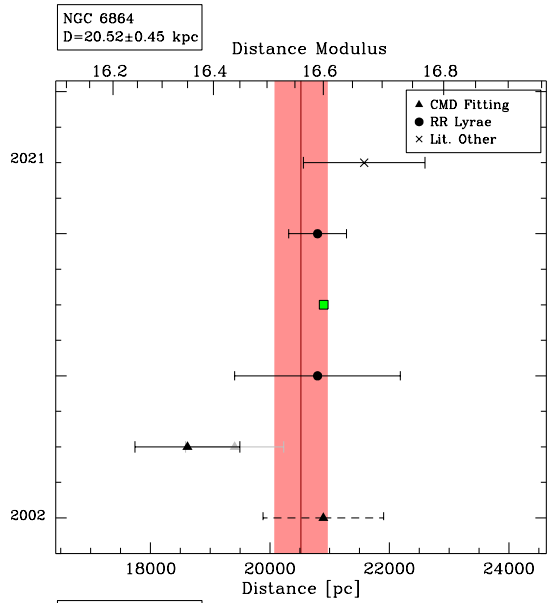












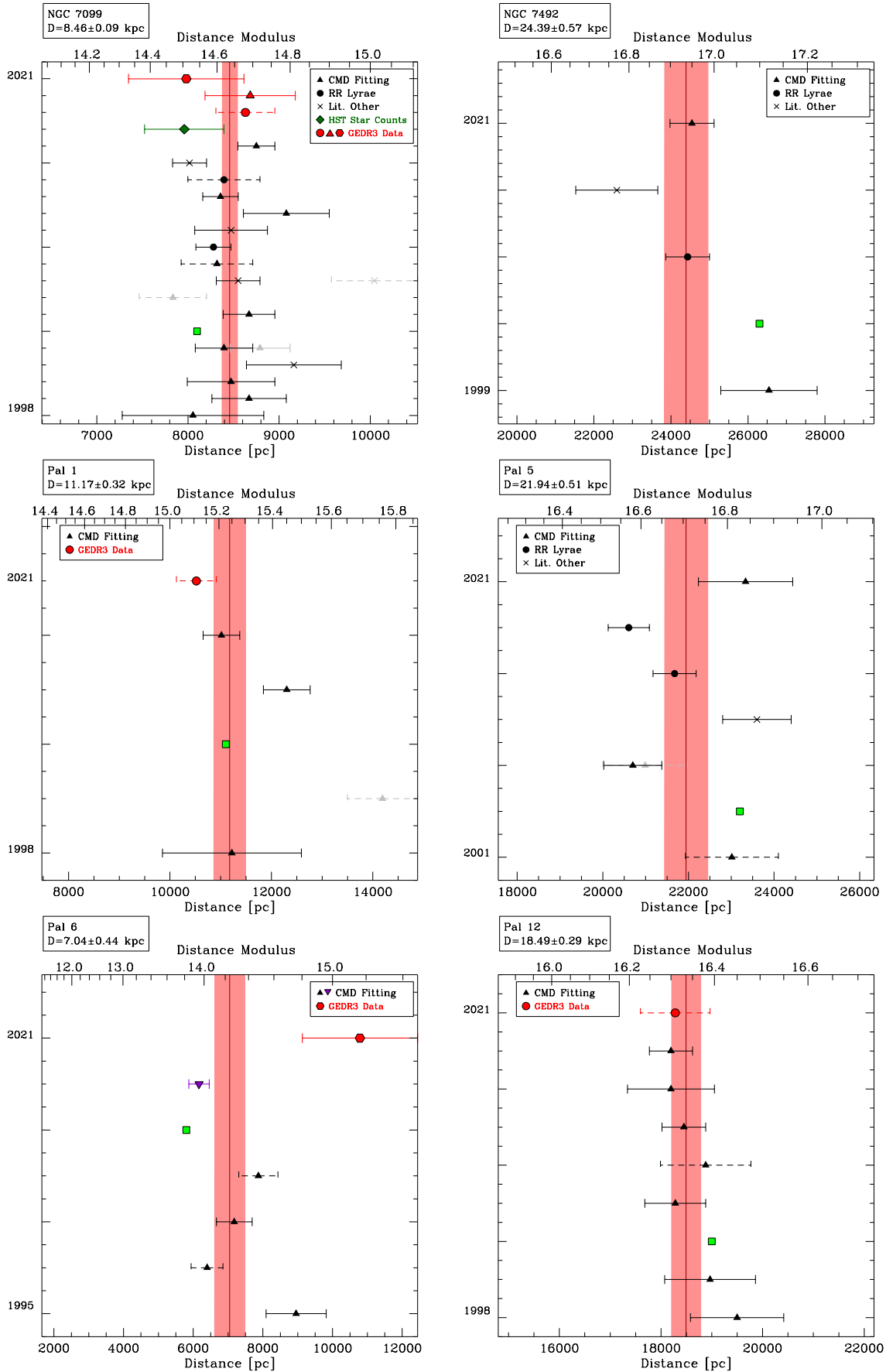


Figure 27. Same as Fig. 8 for NGC 7099, NGC 7492, Pal 1, Pal 5, Pal 6 and Pal 12

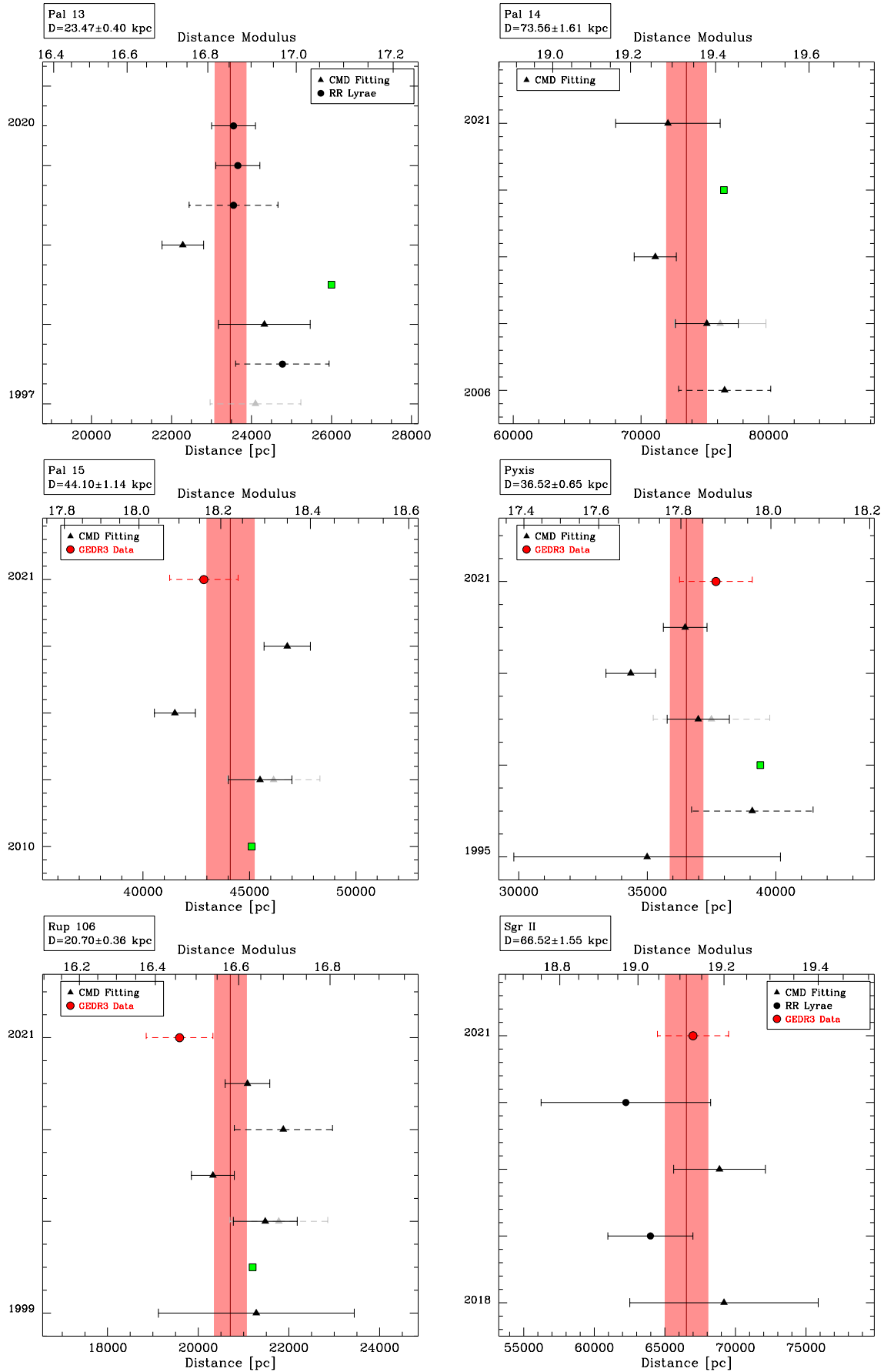


Figure 28. Same as Fig. 8 for Pal 13, Pal 14, Pal 15, Pyxis, Rup 106 and Ter 1

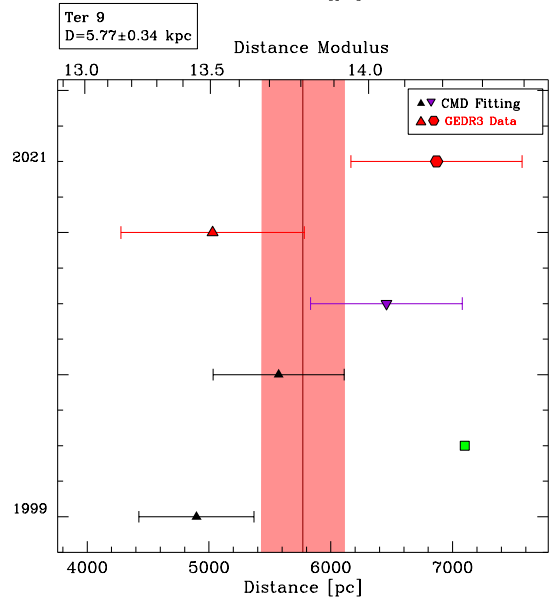
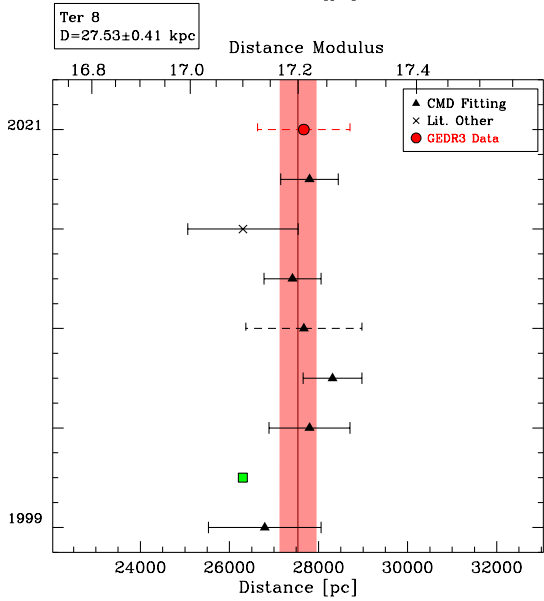
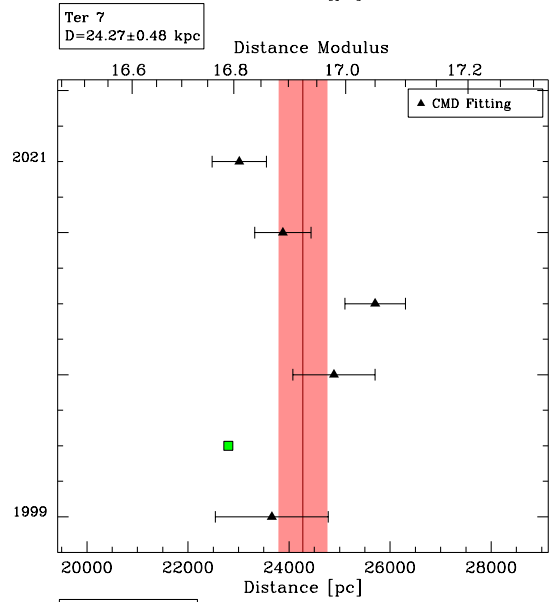
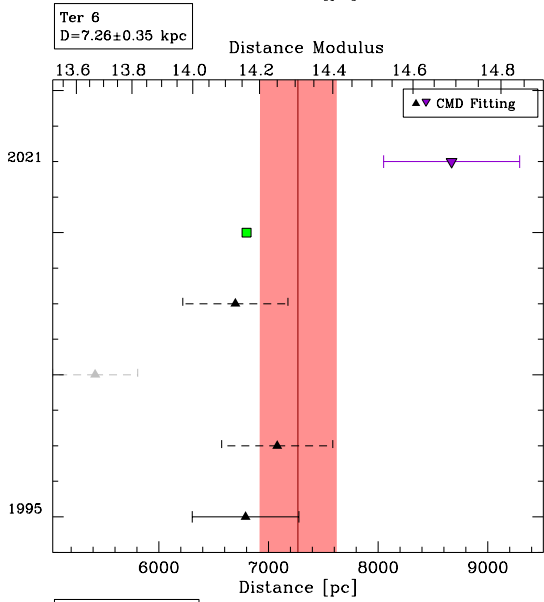
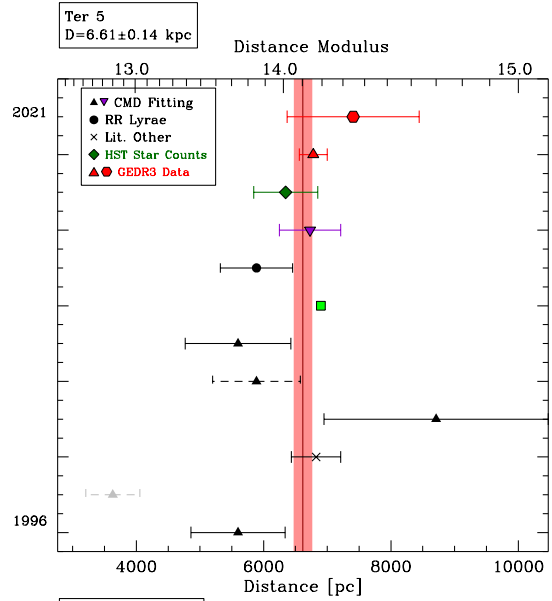
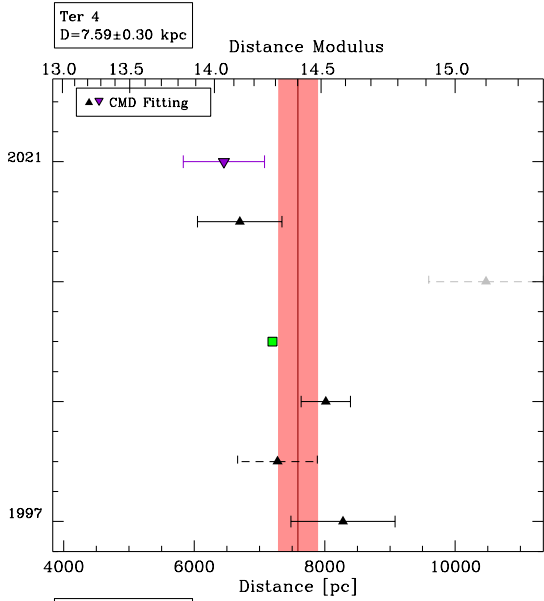


Table 2 – *continued*

Name	GEDR3 parallax dist. [kpc]	GEDR3 kin. dist. [kpc]	HST kin. dist. [kpc]	Subdwarf dist. [kpc]	Star Count dist. [kpc]	Lit. dist. [kpc]	Mean distance [kpc]	N_{Tot}
Pal 15	-	-	-	$42.855^{+2.227}_{-2.117}$	-	$44.096^{+1.152}_{-1.123}$	$44.096^{+1.152}_{-1.123}$	4
Pyxis	-	-	-	$37.670^{+1.414}_{-1.363}$	-	$36.526^{+0.662}_{-0.650}$	$36.526^{+0.662}_{-0.650}$	6
RLGC 1	-	-	-	-	-	$28.840^{+4.288}_{-3.733}$	$28.840^{+4.288}_{-3.733}$	1
RLGC 2	-	-	-	-	-	$15.849^{+2.356}_{-2.051}$	$15.849^{+2.356}_{-2.051}$	1
Rup 106	-	-	-	$19.588^{+0.735}_{-0.709}$	-	$20.730^{+0.366}_{-0.360}$	$20.711^{+0.365}_{-0.359}$	6
Sgr II	-	-	-	$66.988^{+2.514}_{-2.423}$	-	$66.527^{+1.581}_{-1.544}$	$66.527^{+1.581}_{-1.544}$	5
Ter 1	-	-	-	-	-	$5.673^{+0.175}_{-0.170}$	$5.673^{+0.175}_{-0.170}$	6
Ter 2	-	-	-	-	-	$7.681^{+0.336}_{-0.322}$	$7.753^{+0.332}_{-0.318}$	4
Ter 3	-	-	-	-	-	$7.568^{+0.338}_{-0.324}$	$7.644^{+0.318}_{-0.304}$	3
Ter 4	-	-	-	-	-	$7.558^{+0.316}_{-0.304}$	$7.591^{+0.315}_{-0.302}$	5
Ter 5	-	6.780 ± 0.220	-	-	6.346 ± 0.503	$6.462^{+0.224}_{-0.217}$	$6.617^{+0.150}_{-0.148}$	10
Ter 6	-	-	-	-	-	$7.271^{+0.360}_{-0.343}$	$7.271^{+0.360}_{-0.343}$	4
Ter 7	-	-	-	-	-	$24.277^{+0.497}_{-0.487}$	$24.278^{+0.496}_{-0.487}$	5
Ter 8	-	-	-	$27.669^{+1.038}_{-1.001}$	-	$27.542^{+0.422}_{-0.415}$	$27.535^{+0.421}_{-0.415}$	8
Ter 9	-	5.030 ± 1.037	-	-	-	$5.605^{+0.434}_{-0.403}$	$5.770^{+0.356}_{-0.333}$	5
Ter 10	-	-	-	-	-	$10.247^{+0.414}_{-0.398}$	$10.212^{+0.412}_{-0.396}$	3
Ter 12	-	5.002 ± 1.851	-	-	-	$5.107^{+0.444}_{-0.408}$	$5.166^{+0.400}_{-0.369}$	4
Ton 2	-	-	-	-	-	$6.934^{+0.360}_{-0.343}$	$6.987^{+0.344}_{-0.326}$	3
UKS 1	-	-	-	-	-	$15.581^{+0.570}_{-0.550}$	$15.581^{+0.570}_{-0.550}$	2
VVV-CL001	-	-	-	-	-	$8.204^{+1.664}_{-1.383}$	$8.082^{+1.622}_{-1.343}$	1
Whiting 1	-	-	-	-	-	$30.591^{+1.192}_{-1.147}$	$30.591^{+1.192}_{-1.147}$	2
Pal 6	-	-	-	-	-	$6.887^{+0.472}_{-0.442}$	$7.047^{+0.463}_{-0.433}$	6

Table 3. Globular cluster distances from the literature used in this paper. For each distance we give either the de-reddened distance modulus or the distance in kpc depending on what has been given in the original paper.

Cluster	Source Paper	Method	DM/Distance
2MS-GC01	Ivanov & Borissova (2002)	TRGB	12.64 ± 0.40
2MS-GC02	Borissova et al. (2007)	CMD Fitting	13.55 ± 0.18
2MS-GC02	Alonso-Garcfa et al. (2015)	RR Lyrae	14.28 ± 0.35
AM 1	Hilker (2006)	CMD Fitting	20.45
AM 1	Dotter et al. (2010)	CMD Fitting	20.37
AM 4	Carraro (2009)	CMD Fitting	17.58 ± 0.20
AM 4	Hamren et al. (2013)	CMD Fitting	17.28 ± 0.03
Arp 2	Ferraro et al. (1999)	ZAHB	17.39 ± 0.11
Arp 2	Dotter et al. (2010)	CMD Fitting	17.33
.	.	.	.
.	.	.	.